The Dissertation Committee for Khai Hong Pham Certifies that this is the approved version of the following dissertation:

Characterization and Modeling of Mixed-mode I+III Fracture in Brittle Materials

Committee:

Krishnaswamy Ravi-Chandar, Supervisor

Chad M. Landis

Kenneth M. Liechti

Mark E. Mear

Michael P. Marder

Characterization and Modeling of Mixed-mode I+III Fracture in Brittle Materials

by

Khai Hong Pham, B.S.

Dissertation

Presented to the Faculty of the Graduate School of

The University of Texas at Austin

in Partial Fulfillment

of the Requirements

for the Degree of

DOCTOR OF PHILOSOPHY

The University of Texas at Austin

December 2015

Acknowledgements

First of all, I would like to thank my supervisor, Professor Ravi-Chandar, for his endless guidance, support, and encouragement. I am also thankful to Professor Mear for allowing me to use his BEM code in our research. I would like to thank Professor Landis for the discussions about the phase-field model.

I would like to thank Pablo Cortez, Joseph Pokluda, Travis Crooks, Andrew Gross and Qunli Liu for their assistance in preparing specimens and building experimental apparatus. I would like to thank the Vietnam Education Foundation for granting me the two-year Fellowship. The computations performed as part of this work were supported by a generous allocation of computing resources by the Texas Advanced Computing Center. This support is gratefully acknowledged.

I would like to express my appreciation to my parents, parents-in-law, and my wife for their love and endless support. I dedicate this work to our newborn child.

Characterization and Modeling of Mixed-mode I+III Fracture in Brittle Materials

Khai Hong Pham, Ph.D.

The University of Texas at Austin, 2015

Supervisor: Krishnaswamy Ravi-Chandar

Mixed-mode I+III fracture in brittle materials presents spectacular, scale-independent pattern formation in nature and engineering applications; and it is one of the last remaining puzzles in *linear elastic fracture mechanics*. This problem has received much attention in the literature over the past few decades both from experiments and analysis, but there are still open challenges that remain. Specifically, the existence of a threshold ratio of mode III to mode I loading below which fragmentation of the crack front (formation of daughter cracks) does not occur and the length scale associated with the spacing of the fragments when they do occur are still under debate. The continued growth of cracks under remote mode I + III loading is also of interest; it is observed that in some cases the fragmented cracks coalesce, while in others they maintain their independent development.

We approach this problem through carefully designed experiments to examine the physical aspects of crack initiation and growth. This is then explored further through numerical simulations of the stress state that explore the influence of perturbations on the formation of daughter cracks. We show that a parent crack subjected to combined modes I+III loading exhibits fragmentation of the crack front into daughter cracks *without any threshold*. The distance between the daughter cracks is dictated by the length scale

corresponding to the decay of the elastic field; this decay depends on the characteristic dimension of the parent crack from which the daughter cracks are nucleated. As the daughter cracks continue growing, they coarsen in spacing also through elastic shielding. As the daughter cracks grow farther, the parent crack, pinned at the original position, experiences increased stress intensity factor and the bridging regions begin to crack and the parent crack front advances towards the daughter cracks. This establishes a steady state condition for the system of parent crack with equally spaced daughter cracks to continue growing together.

Finally, direct numerical simulation of crack initiation and growth is explored using a phase-field model. The model is first validated for in-plane modes I + II through comparison to experiments, and then used to explore combined modes I + III in order to study the above mechanism of mixed-mode I + III crack growth.

Table of Contents

List of Tables

List of Figures

Chapter 1: Introduction

1.1 Review of 3D Fracture

The question of an appropriate criterion for fracture, although originally raised by Griffith nearly one century ago, is still being discussed, even within the restricted setting of linearly elastic materials, exhibiting a small-scale (nonlinear) fracture process zone. Griffith's criterion, as originally stated, is itself quite remarkable in its generality; subsequent attempts have only provided simplified implementations of this idea such as to permit applications to specific conditions of loading symmetries. For completeness, we quote the theory of rupture postulated by Griffith:

> …the problem of the rupture of elastic solids has been attacked from a new standpoint. According to the well-known 'theorem of minimum energy', the equilibrium state of an elastic solid body, deformed by specified surface forces, is such that the potential energy of the whole system is a minimum. The new criterion of rupture is obtained by adding to this theorem the statement that, the equilibrium position, if equilibrium is possible, must be one in which rupture of the solid has occurred, if the system can pass from the unbroken to the broken condition by a process involving a continuous decrease in potential energy. In order, however, to apply this extended theorem to the problem of finding the breaking loads of real solids, it is necessary to take account of the increase in potential energy which occurs in the formation of new surfaces in the interior of such solids. … A.A. Griffith, (1920).

In principle, this criterion should be able to predict arbitrary evolution of the crack(s), if such evolution is possible quasi-statically[1]. The total energy of the system is

[1] If dynamic fracture is to be considered, inclusion of kinetic energy is essential.

written as: $E = \Pi + U_s$ where U_s is the surface energy and $\Pi = -W_{\partial R} + U_R$ is the potential energy of the mechanical system. Griffith's postulated fracture criterion is then: $E'(a) = 0$ where a represents the equilibrium crack length. Griffith's example was a crack loaded with an opening mode symmetry with the consequence of a straight extension of the crack and he equated the fracture energy to the surface energy (surface tension), but the theory itself corresponds to the standard idea of energy minimization, and has no such restrictions. In principle, when considering $E'(a) = 0$, all possible crack configurations must be considered, and all possible source of dissipation that occur prior to generation of failure could be introduced into U_s, not just the surface energy. Therefore, the criterion for selection of the crack path (or nucleation of a crack) is embedded in Griffith's postulate; the main hurdle is that it is extremely difficult to extract the path corresponding to this minimization unless special methods are introduced to permit crack surface evolution! The change in the mechanical potential energy (outside of the crack surface energy) $-d\Pi / da = G$ is labeled the elastic energy release rate.

Practical fracture *criteria* (note plural) have been introduced since the time of Irwin (1957), that, while still based on the Griffith theory, are of limited validity. Nevertheless, such criteria are of enormous practical significance since they permit the design of fracture critical structures, determination of residual strength of structural components in the presence of cracks, and assessment of structural integrity in a large number of applications. The separation of the global loading into the three symmetries – opening mode (mode I), in-plane shearing mode (mode II) and anti-plane shear mode (mode III) – is an extremely useful exercise that decouples the problem of crack path selection from the energy balance equation, at least for mode I. Since mode I loading is perhaps the most prevalent in structural applications, such decoupling has permitted successful development of a practical fracture theory. Consider a local region of a curved crack front (CF), with the position along the crack indicated by the arc length s as shown in Figure 1.1a. The unit vector $\mathbf{t}(s)$ is tangent to the CF, the unit vector $\mathbf{n}(s)$ is normal to the original crack plane (CP) and the unit vector $\mathbf{b}(s)$ indicates the normal to the CF and completes the triad of mutually orthogonal unit vectors at the point s. For simplicity consider that the cracked solid is subjected to loading such that the crack tip experiences a constant combined mode I+II+III loading indicated by the stress intensity factors (SIF) $\left(K_I^\infty, K_{II}^\infty, K_{III}^\infty\right)$ along the $\left(\mathbf{n}, \mathbf{b}, \mathbf{t}\right)$ directions, respectively.

For mode I, based on the Williams (1952) and Irwin (1957) estimate of the singular crack tip stress field, $\sigma_{\alpha\beta} = K_I^\infty \left(2\pi r\right)^{-1/2} f_{\alpha\beta}\left(\theta\right)$, where $f_{\alpha\beta}^I\left(\theta\right)$ is a known angular distribution, the connection to the Griffith criterion can be written as $G = \left(1-\nu^2\right)\left(K_I^\infty\right)^2 / E$, where $\left(E, \nu\right)$ are the modulus of elasticity and Poisson's ratio, respectively. The Griffith fracture criterion can be written as $K_I^\infty = K_{IC}$ at onset of crack growth, where K_{IC} is the *fracture toughness* and is related to the *fracture energy per unit area* G_c by $\sqrt{EG_c / (1-\nu^2)} \equiv K_{IC}$. This should be considered to be a solved problem, apart from the search for numerical methods that can implement this in a robust calculation.

For problems involving coupled in-plane modes I+II, the stress field in the vicinity of the crack tip is written as: $\sigma_{\alpha\beta} = K_I^\infty \left(2\pi r\right)^{-1/2} f_{\alpha\beta}^I\left(\theta\right) + K_{II}^\infty \left(2\pi r\right)^{-1/2} f_{\alpha\beta}^{II}\left(\theta\right)$, where $f_{\alpha\beta}^{II}\left(\theta\right)$ is another known angular distribution, and the connection to the Griffith criterion can be written *formally* as: $G = \left(1-\nu^2\right)\left[\left(K_I^\infty\right)^2 + \left(K_{II}^\infty\right)^2\right] / E$. However, it must be noted that this estimate of the energy release rate is valid only for a straight line extension of the crack; however, it is expected that due to the asymmetry in the loading under combined modes I+II, that the crack will in general experience a curved or kinked crack evolution, depending on the magnitude of the asymmetry that is dictated by the ratio: $K_{II}^\infty / K_I^\infty$. At least three different formulations of the failure criterion have been used in the literature: (i)

Griffith – crack grows in the direction of the maximum energy release, when this attains the fracture energy, G_c. Calculation and implementation of this criterion has been difficult and awaits the development of numerical or other methods – such as the phase field method – for determining this path. (ii) Maximum hoop stress criterion (Erdogan and Sih, 1963) – crack grows in the direction perpendicular to which the hoop stress reaches a maximum; of course, the energy released in this direction will be a function of the stress intensity factors; therefore, this criterion can be written as: $F\left(K_I^\infty, K_{II}^\infty\right) = 0$. (iii) Principle of local symmetry (PLS, Goldstein and Salganik,1974): consider an infinitesimal extension of the main crack along some direction γ in the ***n***-***b*** plane (see Figure 1.1b), and denote the stress intensity factors at the tip of such extension as $\left(k_I(\gamma), k_{II}(\gamma)\right)$; according to PLS the crack will grow in the direction γ_c in which the local mode II stress intensity factor vanishes: $k_{II}(\gamma_c) = 0$, when $k_I(\gamma_c) = K_{IC}$. The scatter in the available experimental data prevents a positive discrimination between the predictions of the maximum hoop stress criterion and the principle of local symmetry; within these limits, both the PLS and the maximum hoop-stress criterion appear to provide acceptable predictions of crack path and growth. Combined modes I+II also represents a nearly solved problem; additional investigations could be fruitful if directed towards design of suitable experiments that could discriminate between the different failure criteria and towards development of robust numerical methods for implementation of these failure criteria.

For problems involving mixed modes I+III, the situation is much less developed for many different reasons. First, there have been limited attempts, some experimental and others analytical, to extract/elucidate the appropriate failure criterion. Second, the available experimental investigations have been clouded somewhat by uncertainties associated with the actual loading/boundary conditions that bring to question the mode mix really responsible for crack initiation/growth. Lastly, while the anti-plane shear problem for deformation is governed by Laplace's equation in two-dimensions, the corresponding fracture problem must include additional specification of the nature of the failure process before the need for three-dimensional analysis can be determined; thus, on the one hand, if failure is taken to be caused by slip along planes of maximum shear (as in the work of Barenblatt and Cherepanov, 1961), the mode III problem remains two-dimensional, and such "shear cracks" can propagate with the normal to the crack surface remaining in the plane and maintaining the anti-plane symmetry. On the other hand, if one considers that failure is caused by opening stresses, one must abandon the assumption that the solutions retain anti-plane symmetry; the fracture problem is then inherently three dimensional, and indicates possibly discontinuous evolution of the crack that make analysis difficult. This distinction has not always been maintained clearly in the literature, with most analyses of the problem implicitly assuming failure by opening stresses.

Early experimental results of Sommer (1969) and Knauss (1970) revealed unambiguously that a continuous crack front under mixed mode I + III loading fragments or breaks up into multiple crack front segments with discontinuities. Hence, the question of what fracture criterion should be used under such mixed-mode conditions is of paramount importance; the criterion used should, of course, take into account the failure mechanisms that govern the fracture process. The generalization of the PLS (discussed earlier for mixed-mode I+II) proposed by Goldstein and Salganik (1974), is the following criterion:

$$\begin{aligned} & k_{II}(\gamma_c) = 0 \\ & f\left(k_I, k_{III}\right) = 0 \end{aligned} \tag{1.1}$$

where the Eq.(1.1a) indicates vanishing of mode II, while the Eq.(1.1b) implies energy balance – note that this is still a local criterion imposed at every point s, and dictates the crack growth angle γ_c in the ***n*-*b*** plane. Different versions of this criterion have been used by a number of investigators to examine mixed-mode fracture. For example, in the case of pure anti-plane shear loading, $\left(K_I^\infty = 0, K_{II}^\infty = 0, K_{III}^\infty\right)$, if fracture is generated by mechanisms dictated by the shear stresses, a failure criterion based solely on the perturbed mode III stress intensity factor, k_{III}, is adequate and the crack grows continuously from the plane of the initial crack following the direction of maximum k_{III}. This implies that there is no twist of the crack front about the ***b***-axis, but possible rotation about the ***t***-axis; anti-plane symmetry is maintained during crack growth. Barenblatt and Cherepanov (1961) appear to have been the first to use such a criterion to examine the dynamics of shear fracture.

Another criterion that has been widely used (see for example, Gao and Rice, 1986; Xu et al. 1994; Leblond et al. 2011), one that is more suitable for materials that fail through the tensile fractures is the suitably extended Griffith energy criterion:

$$G = \frac{\left(1-\nu^2\right)}{E}\left[k_I^2 + \frac{1}{(1-\nu)}k_{III}^2\right] = G_c \tag{1.2}$$

However, this criterion is a local criterion and obtained by considering a smooth (continuous) evolution of the crack surface from the initial (parent) crack; in other words, the new crack front remains in the ***t***-direction and rotates about the ***b***-axis smoothly as it emerges from the parent crack front. On the other hand, experiments indicate abrupt nucleation of discontinuous crack front fragments directly from the parent crack front. This issue has been addressed by a number of authors (see for example, Xu et al. 1994; Pons and Karma, 2010; and Leblond et al. 2011) through a linear stability analysis. Xu et al (1994) considered sinusoidal perturbations of the crack front/surface analytically[2] and numerically, while Pons and Karma (2010) considered helicoidal perturbations of the crack front through a phase field model of fracture, and more recently, Leblond et al. (2011) examined the same problem analytically. In the perturbation analysis of Leblond et al. (2011), a straight crack front was perturbed by helicoidal perturbation; and the variations of SIFs and energy release rate for the perturbed crack front were calculated analytically. The PLS (Eqs.(1.1) and (1.2)) and Griffith's criteria were used as the fracture criteria to calculate the rate of growth of the linear instability mode. This provides a number of predictions. First, it indicates that helicoidal perturbations became unstable when the ratio of $\beta \equiv K_{III}^{\infty} / K_{I}^{\infty}$ exceeded a critical value $\beta_c(\nu)$ that is a function of the Poisson's ratio (see Figure 1.2). This instability can be taken as an indication that random perturbations of the crack front can grow and result in fragmentation. Second, the results indicate that above this critical $\beta_c(\nu)$, all wavelengths become unstable and further that the growth rate of the perturbations diverges at short wavelengths. As a result, there is no selection of a particular wavelength that corresponds to the fragment spacing. This also suggests the need for some regularization mechanism that prevents the instability at short wavelengths, perhaps something that depends on the process zone effects (Pons and Karma 2010, Leblond et al. 2011). Third, Pons and Karma (2010) took the numerical simulations further, and observed coarsening of the wavelengths; based on these results, the picture that is presented is one of an instability triggered helicoidal undulation of the crack front above a critical value of $\beta_c(\nu)$, followed by coarsening that results in the formation of crack fragments.

---

[2] Leblond et al (2011) indicate that the formulas of Xu et al. (1994) contain some errors and hence their critical values for $\beta_c(\nu)$ are not reliable.

However, experimental measurements provide only limited support for the coarsening mechanism of fragmentation, and not at all for the instability triggered fragmentation of crack fronts. First, Sommer (1969) examined the role of superposed mode III loading on a crack growing under a dominant mode I loading. The lateral surface of a cylindrical glass rod was subjected to fluid pressure; the fluid penetrated to the inside through surface flaws and then generated an opening mode interior crack perpendicular to the axis of the rod. By superposing a small torque on the rod, the fluid pressure driven crack was then subjected to a small additional mode III loading. In this case, Sommer observed a transition from a smooth to faceted fracture surface; such a transition had been observed earlier by Smekal (1953), who called the fragments “fracture lances” and associated this transition with the competition of mode III and mode I. In Sommer's experiments, mode III is negligibly small when the crack is in the central portion of the rod but increases as it grows towards the outer surface. The experiments were performed at three levels of torsion and the radius and crack tilt angle at the location of the initiation of faceted cracks were measured. Based on the experimental data, Sommer postulated that for lance initiation (fragmentation), a minimum angle of twist of the principal axis was necessary. This minimum angle is presumably dictated by intrinsic material properties and was measured to be 3.3° with respect to the nominal crack plane for the glass tested. The existence of the minimum twist angle of the crack is equivalent to a threshold ratio $K_{III}^{\infty}/K_{I}^{\infty}$ above which the crack front will fragment into facets and below which the crack surface will exhibit smooth undulations. The experimental measurements of Sommer (1969) on the onset of crack front fragmentation indicates a threshold that is significantly lower than the predictions from the linear stability analysis (see Figure 1.2). More recent experiments of Ronsin et al. (2014) emphasize the role of nonlinear material behavior – in particular, the influence of the toughness – on the onset of crack front fragmentation. These experiments were performed on gel specimens made of 5 wt% gelatin in a water-glycerol mixture. Rectangular strip specimens with slanted cracks were used to generate combined mode I + III. Their experiments indicated a number of interesting results. First, they showed that the existence of a threshold for the onset of crack front fragmentation was dependent on the energy release rate; below a critical value crack fronts were found to fragment even in the absence of any mode III, but above this critical value, a finite threshold, dependent on the energy release rate was found. Second, through a step jump experiment in which the energy release rate was altered abruptly from the smooth regime to the fragmented regime, fragmentation was shown to be homogeneously nucleated from the straight crack front. Based on these results, Ronsin et al (2014) suggest that formation of fragments through a linear-instability triggered at a finite threshold of $\beta_c(\nu)$, followed by coarsening as suggested by Pons and Karma (2010) was not the mechanism, but that fragmentation of the crack front occurs through the homogeneous nucleation and growth of localized crack front distortions. This raises the first fundamental question: *whether there exists a threshold ratio* $K_{III}^{\infty}/K_I^{\infty}$ *below which continuous extension of the crack may occur is still open.*

Since we know that mode III loading is important in crack front evolution, we seek a different generalization of the PLS: if in-plane cracks evolve so as to eliminate shear, the natural generalization would be to insist that 3D cracks also evolve so as to eliminate shear. Based on the experiments of Sommer (1969), Knauss (1970), Cooke and Pollard (1996), and Lin et al, (2010), we revisit the criterion that eliminates all shear induced SIF and postulate that the crack will propagate along the direction (γ_c,ϕ_c) when

$$\begin{aligned} k_I(\gamma_c,\phi_c) &= K_{IC} \\ k_{II}(\gamma_c,\phi_c) &= 0 \\ k_{III}(\gamma_c,\phi_c) &= 0 \end{aligned} \tag{1.3}$$

A simple interpretation of this criterion is that the first provides the condition of criticality, while the second and third dictate the rotation angle γ_c of the crack normal about the $\mathbf{t}(s)$ and angle ϕ_c about the $\mathbf{b}(s)$ axes – the tilt and twist, respectively. Pollard et al. (1982) estimated the angle ϕ_c by considering the orientation of the principal tensile stress in the ***t-n*** plane for arbitrary combination of $\left(K_I^\infty, 0, K_{III}^\infty\right)$; this yields

$$\left(\frac{1}{2}-\nu\right)\tan 2\phi_c = \frac{K_{III}^\infty}{K_I^\infty} \tag{1.4}$$

Experimental observations support the above postulate for crack initiation (see Knauss, 1970; Yates et al, 1989; Cooke and Pollard, 1996; Lazarus et al., 2008; and Lin et al, 2010); in particular, the pure mode III experiment of Knauss (1970) indicates an angle of the cracks to be $\pi/4$ in agreement with the prediction of Eq.(1.4). Cooke and Pollard (1996) showed that this criterion is equivalent to $k_{III}=0$ and maximum k_I criterion; both these criteria indicate that $\phi_c \to \pi/4$ as $K_{III}^\infty / K_I^\infty \to \infty$.

However, crack twisting cannot be achieved by a continuous evolution of the original crack front (parent crack front); this requires the crack front to fragment – through the generation of crack nuclei (daughter cracks) – immediately upon application of a nonzero K_{III}. This raises the second fundamental question: *what, if anything, sets the intrinsic scale for the spacing between the nucleated crack front fragments*. Since linear elastic fracture theory does not provide an intrinsic length scale, this length must arise from other geometrical features of the problem – either an intrinsic process zone or a macroscopic length scale.

With the formation of fragmented crack front and growth of daughter cracks from the parent crack under mixed-mode I+III a specific pattern is formed as the crack grows. The cross-section perpendicular to the original crack surface exhibits a typical "factory roof" profile[3] (see Figure 1.3). There are two types of daughter cracks corresponding to the two twist angles in this factory-roof pattern: cracks of type A (sometimes also called *echelon cracks*) are formed by opening mode I, and cracks of type B which are not favorably oriented with respect to local opening mode I. Leblond et al (2001) demonstrated that type B are not energetically favorable in comparison to type A cracks. Based on experimental observation of the dynamic crack growth, Lin et al (2010) determined that type B cracks do not form concurrently with the type A cracks and proposed that type A cracks form first, but the region between them (called the *bridging region*) is either uncracked or breaks later through different methods. The energy penalty associated with the bridging region (indicated as the region R in Figure 1.3b) must be paid as the type A cracks develop. Lin et al (2010) made an estimate of this using dimensional arguments; more recently, Leblond et al. (2015) have formulated a multi-scale model of a cohesive zone that is composed only of type A cracks and determined the energy release rate from such crack configurations.

Goldstein and Osipenko (2012) examined crack front fragmentation evolution through some very innovative experiments. They designed a specimen with two inclined cracks anti-symmetrically disposed with respect to the center line, and loaded in such a manner as to generate a compressive mode I and a mode III loading (see Figure 1.4). Experiments in this configuration were performed in gypsum and cheese; slices of the specimen normal to the ***b*-*t*** plane were taken every few millimeters along the ***b*** direction to reveal the crack geometry. Inclined, unconnected type A cracks were clearly observed with regular spacing; furthermore the spacing and the size of the type A cracks were seen to increase with increasing distance from the parent crack. Based on these sections, they

[3] This terminology was apparently introduced first by Andre Pineau (see Hourlier et al., 1978).

constructed an image of the shape of the type A cracks as they propagated away from the parent crack. The absence of type B cracks that was indicated earlier by Lin et al (2010) was clearly demonstrated in these experiments. Goldstein and Osipenko (2012) also performed an approximate calculation of the stress intensity factor at the type A daughter cracks by removing the tractions on a periodic array of daughter cracks surface that would have been generated by the parent crack. Based on this, they suggested a shielding mechanism that led to the arresting of every other nucleated crack, resulting in a period-doubling or coarsening of the spacing between the daughter cracks. We will examine this configuration in greater detail in this work. We will reproduce these results in a brittle polymer and explore this period-doubling through a full analysis of the stress state in the vicinity of the daughter cracks.

1.2 ORGANIZATION OF THE DISSERTATION

In this work, we address the problem of the initiation and growth of cracks under arbitrary mixed-mode I + III loading conditions. Specifically, our aim is to answer the following questions: (i) Whether there exists a threshold ratio $K_{III}^{\infty}/K_{I}^{\infty}$ below which continuous extension of the crack may occur? (ii) What, if anything, sets the intrinsic scale for the spacing between the nucleated crack front fragments? (iii) Does fragmentation occur through an instability of planar growth along the lines discussed above or through nucleation? (iv) Does coarsening of the fragmented crack fronts occur in brittle materials, and if so, how? and (v) How do the type A cracks interact/merge to form the final crack pattern?

The dissertation is organized as follows: recent works on mixed-mode I+III fracture are reviewed in Chapter 1. The design of specimens and experimental results on glass and Homalite H-100 materials are discussed in Section 1 of Chapter 2, with particular attention to the question of the existence of a threshold for the occurrence of fragmentation along the crack front and the question of pattern formation from the resulting crack initiation. In Section 2 of Chapter 2, we discuss different experimental configurations designed to vary the crack tip stress state, along with the calculations of the initial stress intensity factor along the crack front. Results of experiments performed on Homalite-100 with the goal of demonstrating crack front fragmentation, as well as coarsening of the spacing with distance of propagation are also discussed in this section. These results provide a clear picture of the nucleation of crack front fragmentation, and coalescence/coarsening behavior. In Section 3 of Chapter 2 we describe the edge-cracked tension specimen configuration used for the study of the mixed-mode I+III fracture in gels to reveal the model for the echelon cracks formation. Finally, the direct numerical simulation of crack initiation and growth is explored using a phase-field model in Chapter 3. The model is first validated for in-plane modes I + II through comparison to experiments, and then used to explore combined modes I + III. The main outcomes of this work and their implication on fracture modeling are summarized in Chapter 4.

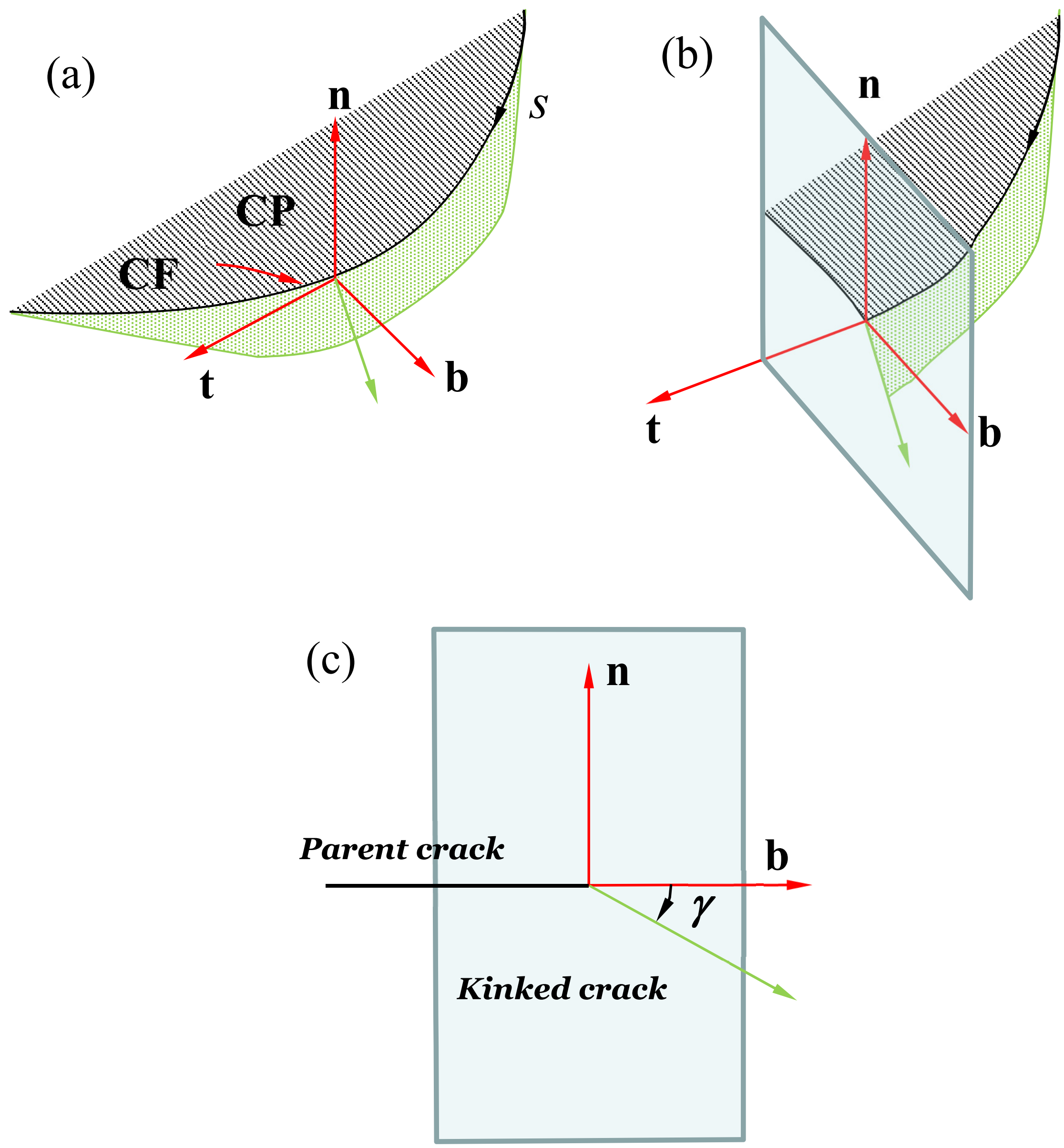

Figure 1.1. (a) Schematic diagram of a three dimensional crack front. CF and CP represent the crack front and crack plane, respectively. $(\mathbf{b}, \mathbf{n}, \mathbf{t})$ represent the directions normal to CF, normal to CP, and tangent to the CF respectively. (b) Slice indicating the geometry in the (**b**-**n**) plane. (c) Geometry of the kinked crack in the (**b**-**n**) plane.

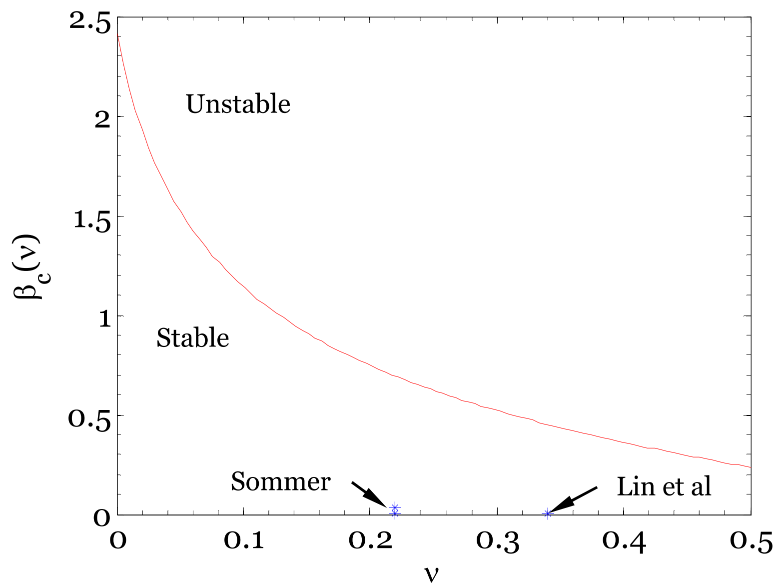

Figure 1.2. Instability prediction from Leblond et al. (2011) corresponding to a helicoidal perturbation of the crack front. The experimental observations from Sommer (1969) and Lin et al. (2010) are shown by the asterisks.

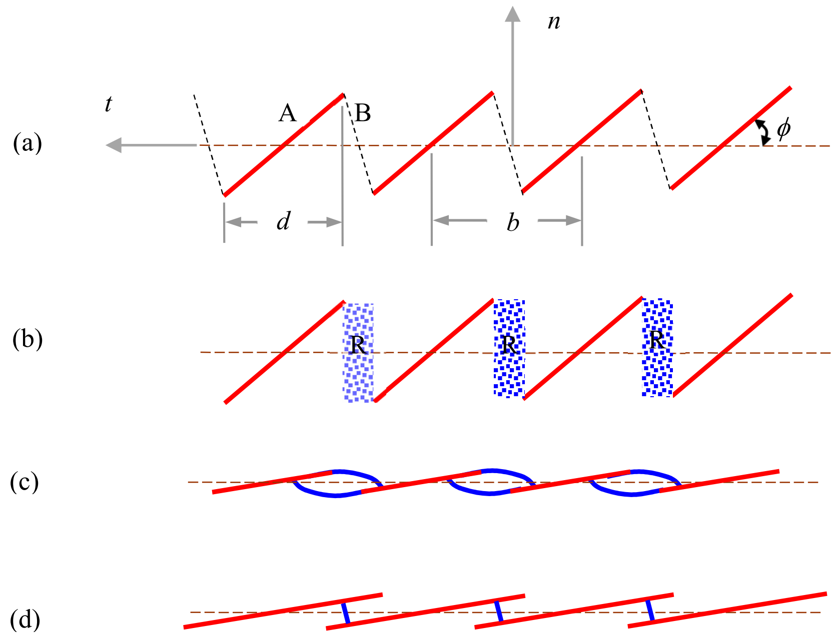

Figure 1.3. (a) Geometry of the "factory roof" profile in the (**n-t**) plane; the red lines indicate type A cracks inclined at an angle ϕ_c with respect to the nominal crack plane and the black dashed lines indicate possible type B cracks; (b) Representation of bringing regions R that connect the type A cracks and provide energy penalty for the overall extension of the crack. (c) "Hand-shaking" mode of linking of the type A cracks; (d) Bridging cracks linking type A cracks, formed after rearrangement of the stress field (modified from Lin et al, 2010)

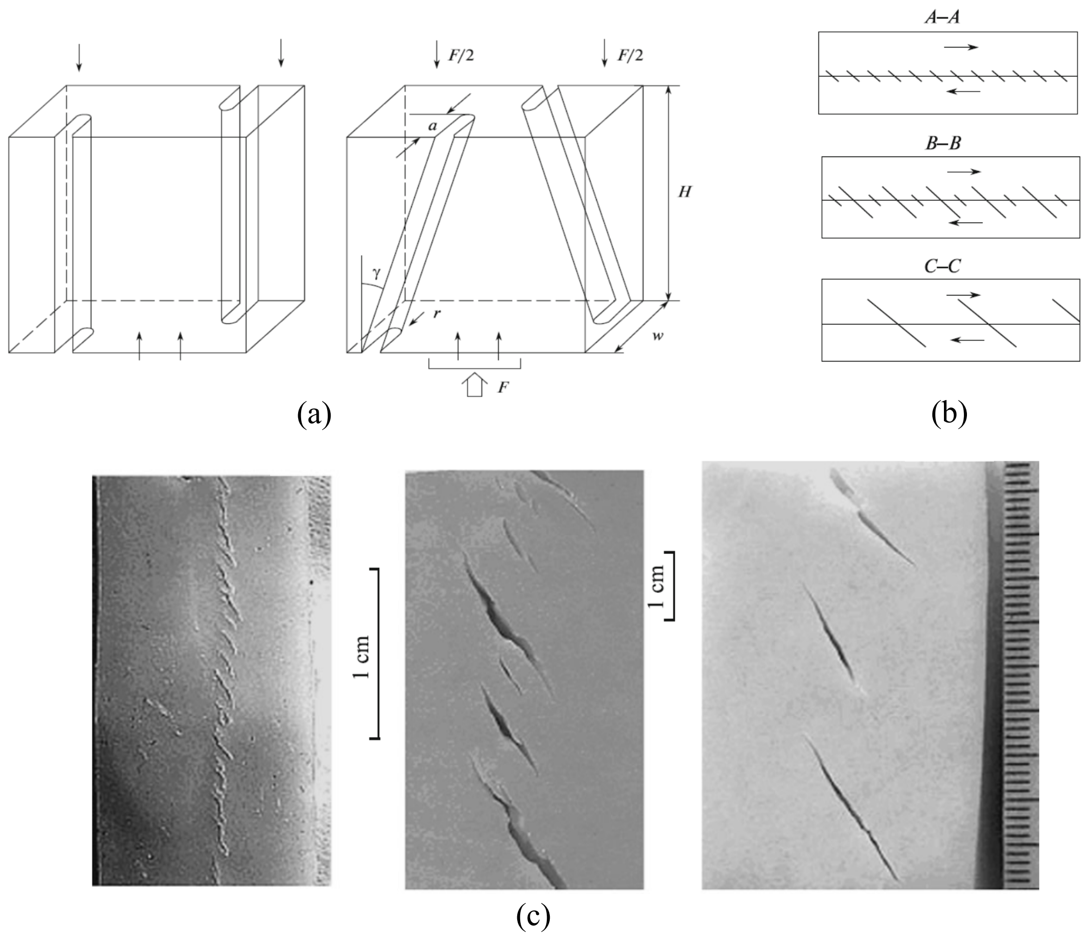

Figure 1.4. (a) The specimen configurations used by Goldstein-Osipenko. (b) Schematic representation of sections of the specimen at different distances from the notch. (c) Images of similar sections from the notch on cheese specimens indicating (i) the absence of type *B* cracks and (ii) the coarsening of the fractures (reproduced from Goldstein and Osipenko, 2012)

Chapter 2: Characterization of Crack Initiation and Growth under Mixed-mode I+III Far-Field Loading[4]

The focus of this chapter is on the initiation and growth of cracks under arbitrary mixed-mode I+III loading conditions. The questions concerning the daughter crack initiation are discussed in Section 2.1: the design of specimens aimed at revealing the underlying reasons for crack front fragmentation are discussed in Section 2.1.1; the results are discussed in Section 2.1.2, with particular attention to the question of the existence of a threshold for the occurrence of fragmentation along the crack front and the question of pattern formation from the resulting crack initiation; shielding along the parent crack front resulting from the nucleation of a daughter cracks is discussed in Section 2.1.3 through boundary element calculations. In Section 2.2, we discuss the fragmentation and coarsening of continued growth of daughter cracks under mixed-mode I+III loading: different experimental configurations designed to vary the crack tip stress state are described in Section 2.2.1, along with the calculations of the initial stress intensity factor along the crack front; results of experiments performed on Homalite-100 with the goal of demonstrating crack front fragmentation, as well as coarsening of the spacing with distance of propagation are discussed in Section 2.2.2; the shielding of daughter cracks is examined in Section 2.2.3 through a calculation of the stress intensity factors at the tip of perturbed daughter cracks. Another set of experiments was performed on hygrogels in both a confined compression configuration and in an edge-cracked configuration; these results are reported in Section 2.3; these experiments provide a complete view of the processes occurring during mixed mode I + III fracture. The main conclusions are summarized in Section 2.4.

---

[4] Section 2.1 of this chapter is based on the published journal article "Pham KH, Ravi-Chandar K. (2014) Further examination of the criterion for crack initiation under mixed-mode I+III loading. Int J Fract, 189:121-138."

2.1 CRACK INITIATION UNDER MIXED-MODE I+III LOADING

The focus of this section is on the initiation of mode I+III cracks, addressing the two fundamental questions (i) Whether there exists a threshold ratio $K_{III}^{\infty} / K_{I}^{\infty}$ below which continuous extension of the crack may occur? (ii) What, if anything, sets the intrinsic scale for the spacing between the nucleated crack front fragments? We examine the initiation of mixed mode I+III cracks through a systematic variation of specimen design that enables addressing the issue of the existence of a threshold as well as an intrinsic length scale for the fragmentation of the crack front.

2.1.1 Specimen Design

As discussed in Chapter 1, different specimen geometry and loading configurations have been explored in the literature in order to elucidate initiation and growth of fracture under mixed mode I+III conditions. However, controlling the exact combination of mixed mode loading is quite difficult; in particular, while the primary interest is in the combination of modes I+III, it is extremely difficult to eliminate mode II loading, except in some special cases, such as the internal pressure combined with superposed torsion which was used by Sommer (1969). In this section, we begin with the geometry and loading considered by Goldstein and Osipenko (2012) (see Figure 1.4 of Chapter 1). Then, we consider modifications to this geometry and loading in order to control the crack tip state; specific designs of specimens were based on accurate calculations of the stress intensity variations using a boundary element technique, and are aimed at examining crack path selection at nucleation, threshold behavior of crack front fragmentation, and the spacing of fragmentation. Using these variants of the Goldstein-Osipenko geometry, we are able to expand the range of $K_{III}^{\infty} \big/ K_{I}^{\infty}$ that can be examined.

A. Goldstein-Opisenko Geometry and Variants

We performed a number of simulations to calculate the SIFs using a Symmetric Galerkin Boundary Element code (Li and Mear, 1998; Li et al, 1998). First, the Goldstein-Osipenko geometry shown in Figure 1.4 of Chapter 1 was simulated with the following dimensions: $H = 2.0$, $w = 1.0$, $\gamma = 15°$ and $a = 0.25w$. The variation of the mode I, II and III SIFs for this geometry along one of the cracks is shown in Figure 2.1[5]; it is clear that the mode I SIF is negative, indicating crack closure/contact for sharp cracks, and that the mode III SIF reaches very large values. We note that the simulations considered an ideally sharp crack, while the experimental crack would have some bluntness arising from the fabrication process. At the central portions of the crack front, this combined mode I+III SIF will cause crack initiation with an angle ϕ_c with respect to the main crack plane and possibly trigger crack front fragmentation. However, in addition to these two modes, it can be identified readily that the mode II SIF is singular at the surface where the crack intersects the free surface and varies monotonically across the specimen. Such variation of K_{II}^{∞} was pointed out by Lin et al (2010) for the bending specimen. The role of this K_{II}^{∞} is to kink the crack to attain local mode I conditions; in brittle materials such as glass and H-100, the effect of mode II is very strong and causes the crack to follow a tortuous surface under all three modes. Therefore, we sought a modification to the Goldstein-Osipenko geometry that would eliminate or minimize the mode II SIF.

B. Calculation of Stress Intensity Factors

In the second set of simulations, the geometry was modified with a design of a part-through crack as shown in Figure 2.2; for the loading configurations considered, the part through crack is not expected to generate a mode II stress intensity factor at the point where

[5] In this and other plots showing the stress intensity factor variation, the curvilinear coordinate normalized by the total crack front length along the pre-crack front is used as the normalized crack front position *s*.

the crack meets a free surface. Two interesting specimen types were found, Type I that introduces predominantly mode I+III loading, while Type II generates negative mode I along most of the pre-crack front.

Specimen Type I: The geometry is shown in Figure 2.2a. The specimen is loaded from the top and supported at the bottom of two pre-cracks. The specific dimensions used are as follows: $L = 3.0$, $H = 2.0$, $d = 2.25$, $a = 0.186$, $b = 0.2$, $r = 1.5$, $\gamma = 26.6^{\circ}$, and $D = 0.5$ for H-100 and $D = 0.75$ for glass. The variation of the stress intensity factors for all three modes along the curved crack front are shown in Figure 2.3. There exist some interesting characteristics to the variation of the SIFs along the crack front that are useful in mixed-mode I+III investigations. K_I^{∞} is positive and dominates the loading with a very large amplitude. K_{II}^{∞} is very small in the central regions of the CF $0.4s - 1.0s$; it should also be noted that, as expected, it goes to zero at $s = 0$ and $s = 1$, where the crack pierces to the free surface. K_{III}^{∞} is large over some portion of the crack front, but only in locations where K_I^{∞} is small. The most interesting part is that K_{III}^{∞} switches sign along the pre-crack front; at $s = 0.82$ K_I^{∞} reaches the maximum value, and both K_{II}^{∞} and K_{III}^{∞} nearly vanish; (we will refer to this location as the *transition point*). The importance of this specimen design is that it can provide a critical test to the existence of a threshold for the fragmentation of the crack front. First, according to the criterion postulated by Lin et al (2010), we expect the initiation of crack growth to occur at the transition point, where K_I^{∞} approaches the critical value K_{IC}, while K_{II}^{∞} and K_{III}^{∞} both vanish; the principle of local symmetry would also suggest crack initiation at this location. Based on Eq.(1.4), we would also expect to see the twist angle on either side of the transition point to be of opposite signs. However, if there exists a threshold ratio of $K_{III}^{\infty} / K_I^{\infty}$ where the fragmentation does not occur, we should observe a continuous evolution of the crack front without fragmentation in region around the transition point. The extent of this region can be estimated from the Sommer's results (Sommer, 1969); if a minimum twist angle of 3.3° is necessary for fragmentation to occur in glass, based on Eq.(1.4), this yields a threshold ratio of $K_{III}^{\infty}/K_{I}^{\infty}$ equal to 0.029 for glass assuming $\nu = 0.25$. From the simulation result for the SIFs, one should observe a flat portion of normalized length 0.042 (equivalent to 2.044 mm for the specimen dimensions indicated earlier) around the transition point. We will address this through experiments on glass and H-100.

Specimen Type II: Specimen Type I has a very large mode I stress intensity factor. As a result, when crack initiation occurs (particularly in the somewhat blunted specimens that were manufactured), further growth is extremely dynamic and interpretation of the fracture surface beyond the onset of crack initiation becomes quite difficult. In an effort to modify the stability of crack growth in the specimen, we flipped the orientation of the specimen with respect to the loading direction for specimen Type I as shown in Figure 2.2b, making it close to the Goldstein-Osipenko specimen geometry, with the exception of the curved crack fronts. The variation of the three stress intensity factors along the crack front is shown in Figure 2.4. In contrast to the Type I specimen, K_{I}^{∞} is negative over most of the crack front except for the portion close to the bottom of the specimen; the largest compressive values of K_{I}^{∞} occur in the same region where K_{III}^{∞} is also large; $K_{II}^{\infty} \approx 0$ in this segment, indicating that we have a segment over which crack initiation will be governed by K_{III}^{∞} and K_{I}^{∞}, but with twist angles that are opposite to that expected in Type I specimens. The nucleation should occur first in the central regions and the cracks may grow in a stable manner until nucleation occurs in the region of positive K_{I}^{∞}.

Other variants of the Goldstein-Osipenko geometry were considered; for example, in order to prevent the possible nucleation of cracks from the positive K_{I}^{∞} in specimen Type II, a compressive stress was applied on the two vertical surfaces as indicated in Figure 2.2c; The resulting variation of the three stress intensity factors is shown in Figure 2.5.

This geometry provides a nice symmetry in the loading; compressive K_I^{∞}, nearly negligible K_{II}^{∞}, and a large K_{III}^{∞} are observed. However, the large compression in the vicinity of the maximum shear makes it difficult to initiate crack growth in this geometry. Preliminary experiments indicated that prior to crack initiation from the machined crack tips, cracks nucleated from other defects near the free surfaces of the specimen under mode I conditions and grew dynamically. Tabulated values of the stress intensity factor variation for the Goldstein-Osipenko geometry and its three variants considered here are given in the Appendix A.

2.1.2 Experimental Results

Parallelepipedic specimens 50.8×76.2 mm (2×3 in; height$\times$length;) were machined from 12.7 mm (0.5 in) thick H-100 and 19 mm (0.75 in) thick glass sheets. The cracks were cut according to the specimen design of types I and II, using a diamond blade with radius 38.1 mm (1.5 in) and thickness 0.178 mm (0.007 in). Although an extremely thin diamond blade was used to machine the crack, the pre-crack front is far from the idealized sharp crack front. There also exist many groove lines along the blunt pre-crack front that are caused by the hard particles that form the diamond-coated cutting blade. The experiments were performed under displacement control in an Instron Model 4482 testing machine. The load vs load-point displacement was monitored. However, in all the tests performed, the response was linear until abrupt and unstable fracture initiation. The critical load varied significantly from test to test due to the fact that there were variations in crack tip state; however, the geometric aspects of the response were repeatable to permit interpretation of the threshold behavior, fragment spacing etc.

A. Threshold Behavior

The main objective of the tests performed with specimen of Type I was to examine the response of the crack when K_{III}^{∞} passes through zero. Therefore, the fracture surface of the glass and H-100 specimens of Type I were examined using a scanning electron microscope (SEM) (Model Quanta 650 FEG) at different magnifications. The fracture surface was coated with a very thin layer of Pd/Pt material before performing SEM observations to prevent charging of the specimens from the electron beam. Figures 2.6 and 2.7 show the detailed fractography of the glass and H-100 specimens, respectively. The fracture surfaces of these materials exhibit many similar features at the early state of the crack growth. First, it appears that initiation of the crack occurred on the pre-crack front very close to the transition point identified through the analysis presented in Section 2.1.1. The fact that nucleation occurs at the transition point is not surprising; either the PLS fracture criterion or its extension would indicate such initiation. The key difference is in the prediction of the onset of fragmentation of the crack front. Second, the fragmentation of the crack front into multiple facets is immediate! This is clearly observed by noting that in the neighborhood of the transition point there does not exist a flat area where pre-crack front grows without fragmentation. For the glass specimen, if the threshold twist angle of 3.3° indicated by Sommer (Sommer 1969) is to hold, a straight extension of the crack front is expected over a length of about 2.044 mm, but it is seen that fragments appear within the distance of 100 μm from the transition point. Within this distance the value of $K_{III}^{\infty}/K_{I}^{\infty}$ is only marginally different from zero. The same behavior is also observed in Figure 2.7 in H-100, with immediate fragmentation of the crack over a length that is nearly the same as in the glass specimen. Taken together, these observations suggest that there appears to be no threshold value of $K_{III}^{\infty}/K_{I}^{\infty}$ required for fragmentation of the crack front; a crack front will fragment immediately as soon as it is perturbed by mode III. It remains to identify the scale on which such fragmentation is observed and we will consider some aspects of this problem in the next section. Finally, beyond the initiation of crack growth at the transition point, further crack growth occurred dynamically, dominated by mode I loading. This specimen design was not suitable for examining continued crack growth, if any, under the combined mode loading

B. Intrinsic Length Scale

While the specimen Type I was well suited for considering the possible threshold behavior, continued growth was dominated as indicated above by mode I. Therefore, experiments were performed on H-100 with specimen Type II, where it was anticipated that as a result of the negative K_I^∞, the nucleated fragments along the crack front may get arrested. However, cracks initiated along the region of the positive K_I^∞ on the pre-crack front (see Figure 2.4, between $0.9s$ and $1.0s$, grew faster than the cracks nucleated in other regions, and quickly reached an unstable state, popping across the entire specimen dynamically. Nevertheless, the unstable cracks deviated away from the machined crack fronts, and left parts of specimen containing "unbroken" portions of the pre-crack that could be examined to evaluate the nucleation of fragments from the machined pre-crack. These unbroken portions were recovered, polished to extremely thin sections on planes above and below the pre-crack surface and imaged by an optical microscope with magnification of $100x$, $200x$ and $300x$; these images are shown in Figure 2.8. It is worth emphasizing that fragmentation spacing can be observed at three different length scales in these specimens. The third level, the largest scale observed, is shown in Figure 2.8a. The pre-crack front is identified by an arrow; the width of the crack is dictated by the blade used to cut the crack and as indicated earlier, this is on the order of 175 to 200 μm. At this level, the nucleated cracks are easily observed, and are indicated in Figure 2.8a and 2.8b;

they appear to form a nice nearly periodic pattern with a spacing of about two pre-crack thicknesses, but also indicate significant fluctuations. There exists a smaller length scale – the second level – that is associated with the width of the groove lines on the pre-crack front. As indicated earlier, in addition to the thickness of the blade that dictates the thickness of the pre-crack, the crack front is decorated with grooves that arise from the size of the cutting particles that are part of the cutting blade. These grooves are on the order of a few tens of microns in size and run along the entire crack front. Nucleation of fragments that occur at these grooves results in fragments with a spacing of a few tens of microns. Finally, fragmentation at the smallest length scale – the first level – was discovered along natural crack front (Figures 2.8c and 2.8d). The thickness of a naturally formed crack is typically much smaller than the machined cracks and is of the order of the fracture process zone. Therefore, one expects the lower bound of the fragment spacing to be dictated by this microstructural scale, as indicated by the results of Lin et al (2010). Indeed, fragments that were nucleated from a natural crack exhibited a much smaller fragmentation spacing in comparison to the machined cracks; optical microscopy resolved this spacing to be about 10 μm, but there could be much smaller features that are not resolved optically.

The SEM images for glass specimen discussed in Section 2.1.2A (Figure 2.6a2) also manifest the cascading length scale of fragment spacing. The larger spacing in Figure 2.6a is associated with the width of the machined pre-crack. But in Figure 2.6a2 a small region along the natural crack front captured at extremely high magnification is shown. It is worth emphasizing that the fragmentation spacing of a natural crack front is of the order of 0.5 – 1.0 μm which is much smaller than the fragmentation spacing for the machined crack front for glass.

For the specimens used in Section 2.1.2A, over the distance of 100 μm near the transition point, the ratio of $K_{III}^{\infty}/K_{I}^{\infty}$ is nearly the same for both the glass and H-100 specimens ($K_{III}^{\infty}/K_{I}^{\infty} \approx 0.001$). Based on the dependence of the fragmentation spacing on the fracture process zone predicted by the stability analysis of Pons and Karma (2010) one would expect differences between glass and H-100, because the fracture process zone size in H-100 is about two orders of magnitude larger than that of glass. But it can be observed clearly that the fragmentation spacing is approximately of the order 30 μm for both materials (see Figures 2.6 and 2.7).

Together, these observations indicate that an intrinsic length scale for the crack front fragmentation spacing does not exist, but that the spacing depends on the characteristic dimension of the driving crack (thickness of the crack). This provides an explanation for the fact that fragmentation of the crack front has been observed in scales ranging from the microscale to the geological scale where the fragmentation space may be on the order of meters. In the following, we will explore the effect of the stress field shielding from one nucleated crack front on the neighborhood of this nucleus.

2.1.3 Boundary Element Calculation for Shielding along the Crack Front Resulting from Nucleation of a Fragment

As discussed in Chapter 1, there have been many attempts at understanding the initiation of cracks under mixed mode I+III. Almost without exception, these investigations have used the approach of getting the stress intensity factor using a perturbation approach in which a continuous (smooth) evolution from the "parent" crack was considered. Linear stability analysis was then considered on the basis of the PLS criterion; as discussed earlier, the predictions of such analysis, for example by Leblond et al (2011), indicate that the crack path is stable for much larger values of $K_{III}^{\infty}/K_{I}^{\infty}$ than observed experimentally. However, if the PLS generalization in Eq.(1.3) is used, we expect crack front to fragment into multiple cracks; we explore the possible origins of the fragment spacing under this criterion through a series of numerical simulations. In order to explore the changes in the

SIF that is triggered by the nucleation of crack front fragments, we introduce a daughter crack in the middle of the parent crack. Because of limitations in the BEM code in representing intersecting cracks, the following strategy was adopted. The parent crack was represented as a sharp crack in a large block of size $(a \times b \times c)$. The specimen was subjected to boundary loading that generated a mixed mode loading $(K_I^\infty, K_{III}^\infty)$ along the straight crack front. The daughter crack was represented by a three-dimensional geometrical feature: the daughter crack was idealized as a disk-like geometrical feature with a "crack tip radius" $r_{\text{micro}} = 12.7\ \mu$m, with a circular crack of radius $a_{\text{micro}} = \alpha r_{\text{micro}}$, and $\alpha \in [5, 50]$. The nucleated crack was taken to be orientated at an angle ϕ_c, as dictated by Eq.(1.4). The system of the parent-daughter cracks is shown in Figure 2.9a. The variation of the stress intensity factors (k_I, k_{II}, k_{III}) along the original crack front that results from nucleation of the daughter crack was calculated from the boundary element simulation. This variation is shown in Figure 2.9b, where the stress intensity factors are normalized by K_I^∞ and the distance along the crack front from the daughter crack is normalized by the radius of the daughter crack. The results shown correspond to $K_{III}^\infty / K_I^\infty = 0.42$, resulting in $\phi_c = 35°$, and for $\alpha \in [5, 50]$, corresponding to a daughter crack of radius $a \in [63.5, 635]\ \mu$m. The shielding effect of the nucleated crack on either side of the daughter crack is evident: the stress intensity factors for modes I and III on the parent crack drop in the immediate vicinity of the microcrack; with distance away from the site of the daughter crack, the stress intensity factors along the parent crack gradually return to the far-field values that correspond to the imposed uniform values, with a small peak at about one radius from the daughter crack. A local fluctuation in the mode II stress intensity factor is also introduced, indicating the inherent coupling of all three modes. It is clear that any crack nucleation that occurs along the crack front will shield – by elastic unloading – a neighborhood whose size depends on ϕ_c and α. In order to obtain a quantitative measure of this shielding, we need to identify the location at which the next crack may nucleate: this could be at the site of maximum k_I located at a distance b_1 from the nucleation point. However, there is a significant amount of k_{III} at this location; nucleation could also occur at the location of minimum k_{III}, which is located at a distance b_3 from the nucleation point. The distances b_1 and b_3 could be considered to indicate the spacing between the nucleated cracks corresponding to any twist angle ϕ_c and crack size α. These simulations were repeated for values of $\phi_c \in [10,35]$ at fixed $\alpha = 20$ and the results of mode I and III stress intensity factors, $\left(k_I / K_I^{\infty}, k_{III} / K_{III}^{\infty}\right)$ were obtained. From these results, the dependence of the distances b_1 and b_3 on ϕ_c were extracted and are plotted in Figure 2.10. From these results, it is seen that b_1 increases with ϕ_c while b_3 indicates a decrease with an increase in ϕ_c; the latter trend is similar to that indicated in the experimental results of Lin et al, (2010) (see Figure 7c of that reference). The implication of this result is that the shielded length (and therefore the fragment spacing) depends on the size of the daughter crack, which in turn, would depend on the characteristic thickness of the parent crack that drives the nucleation. We conclude this discussion by pointing out that we have only considered the nucleation of the crack fragments and not its further evolution. Upon further loading, the nucleated population of daughter cracks will interact with each other, and create a quite complex state of local mode mix; this subject will be discussed in the following section.

2.2 Growth of Cracks under Mixed-mode I+III Loading: Fragmentation and Coarsening

In this section, we address the problem of the growth of cracks under arbitrary mixed mode I + III loading conditions. Specifically, our aim is to answer the following questions: (i) Does fragmentation occur through an instability of planar growth along the lines discussed above? (ii) Does coarsening of the fragmented crack fronts occur in brittle materials, and if so, how? and (iii) how do the type A cracks interact/merge? This section is organized as follows: different experimental configurations designed to vary the crack tip stress state are described in Section 2.2.1, along with the calculations of the initial stress intensity factor along the crack front. Results of experiments performed on Homalite-100 with the goal of demonstrating crack front fragmentation, as well as coarsening of the spacing with distance of propagation are discussed in Section 2.2.2. These results provide a clear picture of the nucleation of crack front fragmentation, and coalescence/coarsening behavior. The shielding of daughter cracks is examined in Section 2.2.3 through a calculation of the stress intensity factors at the tip of perturbed daughter cracks.

2.2.1 Specimen Design

Different specimen geometry and loading configurations have been explored in the literature in order to elucidate the initiation and growth of fracture under mixed-mode conditions (see Sommer, 1969; Knauss, 1970; Cooke and Pollard, 1996; Lazarus et al., 2008; Lin et al., 2010; Goldstein and Osipenko, 2012; Ronsin et al., 2014; Pham and Ravi-Chandar, 2014). However, controlling the exact combination of mixed-mode loading, and generating stable crack growth are quite difficult to achieve experimentally. Furthermore, whenever a crack intersects a free surface, the presence of mode II loading is unavoidable as demonstrated by Lin et al., (2010); this component has the effect of tilting the crack and makes interpretation more difficult. Lazarus et al. (2008) overcame the first difficulty by performing fatigue crack growth experiments with the justification that the crack paths are dictated by the ratio of $\beta = K_{III}^{\infty} / K_{I}^{\infty}$, even if the mechanisms of fracture are different between fatigue and monotonic cracks. In Section 2.1, we considered modifications of the Goldstein-Osipenko crack geometries to obtain specimens with $\beta = K_{III}^{\infty} / K_{I}^{\infty}$ varying from negative to positive values so as to examine the existence of a threshold; the results indicated that crack fronts fragmented and developed type A cracks without a measurable threshold of $\beta = K_{III}^{\infty} / K_{I}^{\infty}$. This study also showed that the fragment spacing was dictated by characteristic dimensions of the parent crack. Here we focus on the continued growth of the fragments.

In the modified Goldstein-Osipenko geometries considered in Section 2.1, the crack fragments interacted with each other, modified their path and coalesced to form a curved crack surface roughened by the fragmented cracks, a process that was aided by the presence of mode II loading. In an effort to control crack coalescence, a compressive stress state around the crack tip was generated by applying a side displacement constraint to the modified Goldstein-Opisenko three point bending configuration (see Figure 2.2c and 2.5). Unfortunately, it is quite difficult to initiate a stable crack under such conditions in order to follow the growth of the fragmented echelon cracks. In this section, we consider a biaxial loading configuration which give us greater flexibility in controlling the combination of mixed-mode I+III loading as well as the stability. The designs of specimens were based on accurate calculations of the stress intensity variations using a boundary element technique, and were aimed at examining coarsening of the fragmented type A cracks.

A sketch of the specimen geometry with loading state is shown in Figure 2.11. A right angle V-notch of depth $0.25D$ is cut from one face of a rectangular block of size $L \times H \times D$. The V-notch is oriented at an angle α with respect to the *L*-side of the rectangular block. On the edge of the V-notch, there is a part-through machined crack of the depth $0.25D$. The part-through crack is intended to reduce the mode II SIF at the location where the crack front meets the free surface. Mode I loading can be generated by inserting a wedge to the V-notch to open the machined crack (we will call this the wedge load). At the same time, a confining load can be applied to both *H*-sides of the specimen to produce mode III loading along the machined crack front as well as a global compressive stress field ahead of the crack front (we will call this the confining load). By varying the angle α, the value of wedge load and confining load, the combination of mode I and III loading along the crack front can be controlled.

The symmetric Galerkin boundary element program of Li and Mear (1998) and Li e al. (1998) is used to determine the SIFs along the crack front accurately. The dimension used in the simulation is $3\times2\times0.5$ in^3, $\alpha=25°$. Two separate sets of simulation were performed: one with the wedge loading (the wedge has the length equal to a half of the V-notch length) and the other with the confining loading. Then superposition is used to produce the SIFs for the final biaxial loading. The variation of the SIFs along the crack front is shown in Figure 2.12. Under the confining load (Figure 2.12a), it is seen that a significant magnitude of mode III SIF, K_{III}^{∞} is generated. Negative values of the mode I SIF K_{I}^{∞} indicates closure of the crack; however, the combination with the wedge loading can create a positive mode I condition. Under the wedge loading (Figure 2.12b), mode I is dominant. In both loading cases, mode II SIF K_{II}^{∞} is zero in the central portions of the crack front, but more importantly negligibly small in the region where the crack intersects the free surface. A representative superposition of wedge and confining loads with a ratio 5:1 is shown in Figure 2.12c. Note that the mode I SIF K_{I}^{∞} is maximum in the central portion of the crack front, and the mode III SIF, K_{III}^{∞}, also reaches its maximum magnitude within this portion. Higher confining loading requires higher wedge loading to trigger crack initiation. Within the central portion of the machined crack front, the gradient of mode I SIF K_{I}^{∞} is much larger than mode III SIF K_{III}^{∞}, and one may expect crack nucleation to occur at the central portion. The nearly uniform stress state within the central portion can trigger multiple nucleation simultaneously, and then the continued growth of the nucleated cracks will provide the scenario of coarsening under the global compressive stress state.

2.2.2 Experimental results on Homalite H-100

A. Crack Initiation and Growth in Homalite-100

Parallelepipedic specimens of dimensions $76.2\times 50.8\times 12.7$ mm^3 ($3\times 2\times 0.5$ in^3) were machined from Homalite H-100, a brittle thermoset polymer. The crack was cut with the geometry according to the specimen design in Figure 2.11 with parent crack angles $\alpha = 10°, 25°, 45°$ using a diamond blade with radius 38.1 mm (1.5 in) and thickness 0.178 mm (0.007 in). The final crack front was sharpened by scraping the crack front with a sharp razor blade. This procedure still results in a blunt crack front, and hence crack initiation occurs above the Griffith threshold. However, our interest in the present experiment is in the subsequent growth of the sharp cracks that are nucleated and hence initiation above the Griffith threshold does not pose a serious problem in the interpretation of the results; the nucleated cracks will each grow at the Griffith threshold. The experiments were performed under displacement control in an Instron Model 4482 testing machine; the rate of wedge displacement was maintained at the lowest value possible for this test machine: 0.4 μm/s. The wedge load vs load-point displacement was monitored. The confining load was produced by two hydraulic pistons connected to a hydraulic pump. The pressure in the hydraulic piston was monitored by a pressure gauge and then used to calculate the confining load.

The control of the combination of mixed-mode I+III is challenging. We probed a large enough range of $K_{III}^{\infty} / K_{I}^{\infty}$ at the nucleation location to produce a large range of crack twist angles. But a larger amount of mode III loading also requires a larger mode I loading to nucleate cracks. This leads to a large amount of elastic energy stored in the specimen at the time of nucleation which may cause dynamic growth of the cracks. Thus, the challenge in the loading constraint is to achieve a large enough ratio of $K_{III}^{\infty} / K_{I}^{\infty}$, but with the cracks still growing quasi-statically. To this end, we used the following loading path, illustrated in Figure 2.13a for three different specimens. First, the application of compression from the hydraulic cylinders generated a linear increase in the (negative) mode I and mode III SIFs, identified as segment 1 in Figure 2.13a[6]. It should be noted that the negative mode I loading inhibits crack initiation and hence very large levels of mode III SIF can be generated without triggering crack initiation; loading was stopped below the threshold of initiation of dynamic crack growth. Second, while holding the hydraulic pistons at fixed position, the wedge loading was increased; due to the Poisson effect associated with the increase in the wedge load, there was a small increase in the confining load. This loading step causes an increase in the mode I and mode III SIFs, with the mode I SIF eventually going into positive values, and is identified as segment 2 in Figure 2.13a. Continued insertion of the wedge can generate mode I SIF that can exceed the toughness of the material and result in crack nucleation. However, this procedure was always found to initiate unstable dynamic cracks. In order to explore stable crack growth or at least a short unstable burst of crack growth and arrest, another loading step was introduced. Third, after the wedge load reached the target value below the unstable cracking threshold, the confining load was reduced very slowly by opening a bleed valve in the hydraulic system until the formation of daughter cracks along the parent crack was observed; this is identified as segment 3 in Figure 2.13a. The formation of these daughter cracks generated audible pops and this was used to halt the wedge insertion and terminate the experiment.

The loading along the black dash-dot path in Figure 2.13a contains only two states (confining and wedge load); this specimen failed at a small magnitude of mode III SIF. The daughter cracks grew dynamically in this case. For the loading along the solid magenta line a higher confining load was applied and then the confining load was decreased; this

[6] The difference between the three specimens arises from the use of two different loading apparatus with different load-train stiffness.

loading path produced stable growth of the daughter cracks. The loading path associated with the dash blue line shows an attempt to reproduce the failure of the second specimen. A combination of $\left(K_I^\infty, K_{III}^\infty\right)$ that was close to the failure point of the second specimen was reached, but daughter cracks did not initiate, possibly because of differences in bluntness. We searched for nucleation of the daughter cracks by alternately increasing and decreasing the confining and wedge loads; initiation occurred a point of higher mode I and lower mode III loading with the crack exhibiting unstable growth. These three loading cases demonstrate that one needs to expend a significant amount of effort in performing this kind of experiment. While the loading paths from only three tests are identified in Figure 2.13a, the red circular points represent the point of nucleation of the daughter cracks in a total of 17 experiments in this configuration; these data points can be used to construct a lower-bound failure envelope (indicated by the red dashed line in Figure 2.13a) inside which the failure cannot occur, but this should be interpreted with care since the initial crack was blunt. The wide scatter of failure points that is observed is due to the variations in specimen geometry and the bluntness of the parent crack.

It is interesting to note that the critical mode I K_I^∞ required for initiating a crack increases initially with increasing K_{III}^∞; this behavior was also revealed in the data shown in Lin et al. (2010). The failure envelope obtained by imposing the energy criterion in Eq.(1.2) is also shown in this figure by the red dash-dot line. The differences are explored further through the following thought experiment: consider a straight crack front under pure mode I that is on the verge of the Griffith threshold; next apply a small mode III. According to Eq.(1.2), a small value of the mode III loading is sufficient to take the crack over the Griffith threshold and extend the crack along the original plane. However, the mode III loading prevents the possible straight extension of the crack by forcing the crack to tilt according to the orientation given by Eq.(1.4), and therefore fragment. Hence, under combined modes I+III, we observe nucleation at the angle ϕ_c, at a mode I SIF that exceeds the failure level under pure mode I.

B. Nucleation of Daughter Cracks from a Blunt Crack Tip

In order to probe the nucleation of daughter cracks further, we stopped some tests at the point where the daughter cracks had just initiated but not grown far away from the parent crack, but in other tests allowed the daughter cracks to grow all the way to the free surface of the specimen. Then we cut a small rectangular slab surrounding the parent and daughter cracks and polished all of its surfaces in order to visualize and quantify the geometry of the daughter cracks. Figure 2.14 shows the images taken using an optical microscope of the slab isolated from the specimen with the parent crack angle $\alpha = 25^\circ$; at onset of daughter crack nucleation, the loading mode mix was $K_{III}^{\infty} / K_I^{\infty} = 0.58$. Figure 2.14a shows a projection (facing the parent crack front or looking at the –***b*** direction); clearly four isolated nucleated crack fragments are observed along the parent crack front. Notice that these correspond to type A cracks and that type B cracks are not formed. The sequence of nucleation of these daughter cracks is indicated in the figure; each crack popped dynamically with an audible pop and arrested. Subsequent cracks nucleated within about ten seconds of each other, each with an audible pop[7]. Figure 2.14b shows that the spacing between the daughter cracks is on the order of 5 mm and the tilt angle of the crack with respect to the parent crack is around 29-36 degrees. The tilt angle expected based on the criterion of identifying the plane of zero shear stress for the ratio of $K_{III}^{\infty} / K_I^{\infty}$ is 37°. After obtaining this image, the specimen was sliced on planes parallel to the daughter cracks and polished so as to observe the geometry of the daughter cracks along their normal; this view is shown in Figure 2.14c for crack number four; the other cracks

[7] The time dependence was most probably due to small pressure fluctuations in the hydraulic system that has a number of rubber hoses and seals.

exhibited nearly similar features. These images were acquired with a Keyance microscope that uses z-stepping to compose a fully focused 3D image; this image contains 3D topographic data that can be used to extract geometrical measurements of the crack surface. A number of remarks are in order:

- First, color fringes that are observed are the result of interference between the light reflections from the top and bottom surfaces of the crack. They indicate that the residual crack opening displacement is quite small – on the order of two to three microns at most; some of this opening is caused by trapped oil and polishing compound used in polishing the specimen for observation.
- Second, the shape of the crack in its plane is nearly elliptical, as indicated by the red dashed line overlaid on the optical image; this shape is somewhat different from the observations of Goldstein and Osipenko (2012) who measured the shape by slicing at a few planes and observing the dimension of the cracks on the sliced planes. It is possible that the extremely brittle nature of H-100, the dynamic nature of crack growth, and the differences in the loading condition contributed to this difference.
- Third, the height variation across the daughter crack along the blue and red dash-dot lines drawn in Figure 2.14c, with reference to an arbitrary datum, is shown in Figure 2.14d; this indicates that the fracture surface has a only very small curvature, and suggests considering the daughter cracks as nearly planar cracks. Therefore, the orientation of the daughter crack can be characterized by a single "twist angle", ϕ_c; this twist angle was measured from all the experiments indicated in Figure 2.13a, and is plotted with respect to the mode mix ratio, $\beta = K_{III}^{\infty} / K_I^{\infty}$, as shown in Figure 2.13b. The anticipated twist angle, based on the criterion of vanishing k_{II}

and k_{III} at the crack tip is given by Eq.(1.4), and is also plotted in Figure 2.13b. Clearly, within experimental scatter[8], the measured orientation of the daughter crack agrees well with the prediction from this criterion. This suggests that when the crack initiation is governed by *nucleation* of daughter cracks as in the case of the blunt parent crack considered in this work, the fracture criterion is simply that the daughter cracks nucleate directly at the angle ϕ_c.

- Finally, the daughter crack arrests, indicating that under slowly varying displacement control, the stress intensity factor at the daughter crack diminishes below the Griffith threshold.

C. *Growth of Daughter Cracks under Confining Compression*

Continued growth can only occur when the wedge loading is increased or the confining pressure loading is decreased. In order to examine crack growth, in some of the experiments performed, the bleed valve was left open after nucleation of daughter cracks was detected in order to continue to decrease the confining load and permit growth of the daughter cracks until complete failure of the specimen. In these experiments, the nucleated daughter cracks propagated in spurts of dynamic growth, with each spurt accompanied by an audible pop. Figure 2.15a shows an overview of one daughter crack, observed along the –***n*** direction, similar to Figure 2.14c (the test conditions correspond to $K_{III}^{\infty} / K_I^{\infty} = 0.67$); the height variation across the daughter crack along the white dash-dot and dash-dot-dot lines drawn in Figure 2.15a, with reference to the mean daughter crack plane is shown in

[8] It should be noted that there are two sources for the observed scatter: measurement error in the identification of the twist angle, and the determination of the ratio of mode III to mode I loading. The first source is rather small since the angles were measured with quantitative microscopy. The second source, on the other hand, could be substantially large and difficult to quantify. It arises primarily from the fact that we use global loading conditions to calculate the ratio, but at nucleation, local perturbations in the crack profile, misalignments in the wedge relative to the specimen notch, and variations in the bluntness.

Figure 2.15b. A magnified view of a portion of the daughter crack surface identified by the white rectangle in Figure 2.15a, spanning from nucleation at the parent crack tip to penetration at the far boundary, is shown in Figure 2.15c; the color scale indicates height differences relative to a datum parallel to the plane of the daughter crack surface close to nucleation. Further magnified views of the white rectangles within Figure 2.15c that focuses on two different region of crack arrest and reinitiation are shown in Figure 2.15d and Figure 2.15e. The height profiles along the blue, red and black dash-dot lines of Figure 2.15c are shown in Figure 2.15f. A number of observations can be made from these fracture surface images:

- Nucleation of a number of daughter cracks begins with a pattern similar to that shown in Figure 2.14a, with the angle ϕ_c determined by the ratio $\beta = K_{III}^{\infty} / K_I^{\infty}$; the initial burst of crack forms an elliptical shape as in the previous example. From Figures 2.15a, 2.15b and 2.15f, it is clear that under continued loading (release of the confining stress resulting in an increase in the mode I SIF along the daughter crack), growth of the daughter crack persists in nearly the same plane as at nucleation, without significant changes until the crack reaches the opposite surface of the specimen.
- Although the "average" crack appears to lie in a plane, suggestive of a mode I crack, numerous surface roughening features – striations on the fracture surface – are observed on the daughter crack surface. From the high magnification view shown in Figure 2.15c, where these are marked as "river" lines, these can be recognized as steps on the fracture surface across which the cracks are on different levels. The resolution of 1 μm minimum height in these micrographs is not adequate to resolve the step heights or the orientation differences across the steps; however, such steps

have been observed in this material during dynamic fracture by Ravi-Chandar and Knauss (1984), who attributed this to interaction with defects, and in epoxies by Hull (1995), who attributed it specifically to small fluctuations in mode III superposed on mode I. These features are really expected to contribute only to the overall energy required for crack growth, and not change the orientation of crack extension.

- Crack growth occurs in dynamic spurts, as a sequence of run-arrest events. In accord with this, numerous arrest lines can be seen on the fracture surface, each corresponding to a spurt of crack growth; these are identified in Figure 2.15c by the white arrows. When the daughter crack arrests, it appears to generate a non-smooth fracture front as can be observed from the higher magnification images in Figures 2.15d and 2.15e; as the crack comes to a stop, its front breaks up into surface steps that are spaced about 5 μm apart, and this break up is seen in the last ~30 μm leading up to crack arrest. When the arrested crack reinitiates, the crack front fragments into stepped cracks spaced about 10 to 40 μm apart. This break up is immediate; it should be noted that since the arrested crack is a naturally formed, sharp crack, it should reinitiate close to the Griffith threshold. Furthermore, since the tilt angles are extremely small, the value of $\beta = K_{III}^{\infty} / K_{I}^{\infty}$ is also very small. Clearly, reinitiation occurs rather abruptly, with a fine scale of twisted cracks confirming the absence of a threshold as indicated in Section 2.1. Recently, Ronsin et al. (2014) observed a similar feature in gelatin gels in an experiment in which a steadily propagating crack was forced to generate fragmented crack fronts by perturbing the state at the crack tip; instantaneous nucleation of fragments was observed. These results suggest that the crack front fragmentation is nucleation driven rather than the result of a loss of stability as indicated by Pons and Karma (2010). Some of the nucleated crack front fragments coalesce, but others continue unhindered (see Figure 2.15d) until the next arrest event.

- From the topographic images in Figures 2.15a and 2.15c, it is observed that there is no rotation of the crack plane as the crack continues to grow away from the nucleation site. The neighboring daughter cracks also maintain their orientation (not shown) and hence the system of daughter cracks grows in parallel, without any rotation. The absence of such rotation is due to the fact that this loading configuration has eliminated any far-field mode II.
- Linking up of the type A daughter cracks through the formation of type B cracks was not seen; perhaps the specimen thickness was small and hence we could not continue the grow the type A cracks farther to determine if type B cracks would (or should) initiate. One may envision that as the type A daughter cracks grow, the compliance of the cracked region increases, but the bridging regions would have to find a way to crack eventually (Figure 1.3). This aspect will be investigated further in the Section 2.3.

D. Nucleation and Growth of Daughter Cracks from a Sharpened Crack

As we had indicated in Section 2.1, the spacing between the nucleated of the daughter crack was dictated by the size of the smallest feature in the parent crack. In an effort to drive this nucleation scale to smaller lengths, the crack tip was scraped with a sharp razor blade in a number of experiments. As a result, we could drive down the distance between the nucleated daughter cracks to about 50 μm. Figures 2.16a and 2.16b show a high resolution optical image of a projected view looking in the –**b** and –***n*** directions respectively ($\beta = K_{III}^{\infty} / K_{I}^{\infty} = 1.0$ and $\phi_c = 37.7^{\circ}$); since this image shows a projection of all fragments, it is difficult to identify individual crack fragments. In order to resolve the cracks clearly, another set of images was acquired with the Keyance microscope to compose a fully focused 3D topography; one such image is shown in Figure 2.16d, where the parent crack plane is used as the reference plane for the color scale. Figure 2.16e shows the height profiles along different lines parallel to the parent crack front identified in Figure 2.16d. For ease of visibility, each trace is shifted by a specific height (1000, -1500 and -3500 microns for lines 1, 2 and 3 respectively). There are a number of observations about crack front fragmentation that can be obtained from these images:

- Daughter cracks, more numerous than in the earlier blunt cracks, are nucleated at discrete locations along the crack front (see Figure 2.16a). In each experiment, these cracks are once again parallel to each other and oriented at a fixed angle relative to the parent crack governed by the local ratio of $K_{III}^{\infty} / K_{I}^{\infty}$. As in the previous cases, the daughter cracks continue to grow straight ahead and maintain their orientation relative to the parent crack (see the slopes of the daughter cracks in Figure 2.16e).
- As indicated in the Section 2.1, the spacing of daughter cracks at initiation is dictated by the length scale associated with the parent crack. This is evident in Figure 2.16a, where there are numerous crack fragments oriented parallel to each other and with different spacing between them at different scales, with the smallest ones spaced about 50 μm apart.
- Type B cracks are not nucleated; the type A daughter cracks are not connected to each other, but only to the parent at the site of the nucleation. In other words, crack growth does not occur through a continuous evolution from the parent crack, but directly through nucleation.
- Figures 2.16a and 2.16e show clear evidence of coarsening of the daughter cracks; while many are nucleated with very small spacing between them, with continued

growth of the daughter cracks, some get arrested, thereby increasing the spacing between the active daughter cracks. This coarsening is similar to that observed by Goldstein and Osipenko (2012) and discussed by Pons and Karma (2010) and Leblond et al. (2011). We will examine this behavior further through a calculation of the elastic field in the next section.

- As the daughter cracks grow further, type B cracks are never formed in this case as well. Due to the large compression parallel to the crack, the specimen indicates continued growth of the type A cracks and they remain unconnected to each other. Because the global load is compressive, the nucleated type A daughter cracks, whose normals are along the direction of minimum compression cannot turn; therefore, as they grow, the daughter cracks maintain the orientation dictated by the ratio of $K_{III}^{\infty} / K_{I}^{\infty}$ at nucleation, with only minor perturbations.
- The behavior described above was observed consistently in specimens with different parent crack orientations ($\alpha = 10°, 25°, 45°$).

2.2.3 Crack Interaction/Shielding Simulation

The coarsening of cracks is explored further by considering the interaction of the daughter cracks nucleated along the parent crack front which is under the global compressive stress field. The geometry with a parent crack and loading condition are the same as confined shear test described in Section 2.2. Because of limitations in the BEM code in representing intersecting cracks, the same strategy adopted in Section 2.1 is used: the parent crack is idealized as a three-dimensional geometrical feature with a "crack tip radius" r_0, with $r_0 = 127$ μm, the daughter cracks are represented as sharp, circular cracks of radius $a = \alpha r_0$, with $\alpha = 50$. Two sets of simulation are performed: one with a family of seven type A daughter cracks of the same size, the second one with the central daughter crack growing 10% in size (Figure 2.17). The twist angle ϕ relative to the parent crack follows the stress state $K_{III}^{\infty} / K_{I}^{\infty}$ of the parent crack front according to the local opening mode criterion (Eq. (1.4)). The spacing between the daughter cracks is chosen based on the location of minimum k_{III} of the perturbed parent crack front when considering only one daughter crack (see Section 2.1).

Figures 2.17b and 2.17d show the plots of SIFs k_I vs. normalized distance along the daughter crack front [$s \in (0,1)$] (at the intersections of the daughter crack front and the parent crack surface). In the first simulation (Figure 2.17b), the SIFs k_I are nearly the same for the inner cracks 2-3-4-5-6. The outer cracks 1 and 7 experience higher SIF because periodic boundary conditions have not been built into the current version of the BEM code used and therefore, they see a free surface effect; thus, the two outer cracks 1 and 7 will play the role of dummy cracks and we will focus attention only on the inner cracks. As the central crack 4 grows 10% in size with a fixed SIF at the far-field, the SIFs k_I for cracks 3-4-5 change significantly: the SIF k_I for central crack 4 increases as one may expect, but it decreases for the neighbor cracks 3 and 5, and does not influence cracks 2 and 6 that are farther away. The upshot of this calculation is that any perturbation that results in one of the daughter cracks propagating ahead of the rest is to shield at least its nearest neighbors. If the perturbation of the daughter crack is larger than the 10% assumed in this calculation, perhaps from dynamic growth, it is conceivable that more than the nearest neighbor gets shielded. Since all the daughter cracks are initially at the Griffith threshold (and hence growing), the result of the elastic shielding is to arrest the shielded daughter cracks, resulting in a coarsening of the spacing between the surviving daughter cracks. It is not clear that this shielding process can (or needs to) continue unhindered as the daughter cracks continue to grow; one limitation of the analysis is that we have considered circular daughter cracks. From the measurements of Goldstein and Osipenko (2012) and the images shown in Figure 2.14c, it can be seen that the daughter cracks have limited extension in the direction perpendicular to the original crack plane, and hence the perturbation calculations need to be examined accounting for the crack shape effects.

2.3 MIXED-MODE I+III FRACTURE IN GELS-MODEL FOR THE FORMATION OF ECHELON CRACKS

In contrast to the experiments performed in brittle, hard polymers where the precrack was a machined blunt notch, brittle, soft polymers such as hydrogels provide the opportunity to generate sharp cracks easily by simple cutting procedures. It should be emphasized that although these materials exhibit large deformations, the fracture behavior is "brittle" since there is very little inelastic[9] deformation prior to fracture. Therefore, the mixed mode I + III experiments were performed in a gelatin based hydrogel in two configurations as described below.

2.3.1 Gel Manufacturing Process

The gelatin-based hydrogel was prepared by dissolving Fisher gelatin type A (G8-500) into a solvent with the weight fraction of 15% of gelatin and 85% of water or the equal weight fraction of water and glycerol mixture. The solution then was heated to a temperature of 70 – 80 °C with continuous stirring. The solution was held at this temperature for 5 minutes to remove large bubbles and then poured into a glass mold to form suitable specimens. Fully transparent gels were formed, with bubbles, if present, below sizes where their presence would scatter light.

[9] These hydrogels may exhibit visco and poroelastic response; but we anticipate that these effects will influence only the energy balance, and not the fracture patterns.

2.3.2 Calibration of the Material Properties of the Gel

The elastic behavior of the hydrogel containing of 15% gelatin and 85% equal weight fraction of water and glycerol mixture was evaluated using a uniaxial tension test. The hydrogel solution was poured into a planar mold to generate a strip specimen with cross-sectional dimensions of 12.7×1.5 mm^2. The specimen was mounted on an Instron Model 5582 testing machine using self-tightening grips. The load and cross-head displacement were monitored using the sensors in the Instron Model 5582 testing machine. The stretch was measured locally using digital image correlation. The variation of nominal stress vs stretch ratio from two different specimens is shown in Figure 2.18. Quite remarkably, this hydrogel exhibits a nearly linear response up to a stretch level of about 2! Beyond this stretch, a stiffening response is observed. Failure was triggered by stress concentrations and defects in the grip region; it is likely that the failure strain levels are even greater than reported here. It is not possible to fit this response with a neo-Hooekan or Mooney-Rivlin material model, but a higher order polynominal generalization of these models could be fitted to this response. The linear portion of the gel response yields an elastic modulus of the gel $E = 90$ kPa. We also performed a single-edge-notched tension test to calibrate the critical stress intensity factor at onset of crack growth (described in Section 2.3.3B). The critical stress intensity factor was found to be $K_{IC} = 1.68$ kPa m$^{1/2}$. Note that this ignores completely the nonlinear material response as well as the large deformations in the vicinity of the crack tip; the main purpose of this exercise was to get an order of magnitude estimate of the fracture energy; this works out to about $G_c = 30$ J/m^2. This value is in the range reported by Baumberger et al.(2006) for a similar gel. One can extract a length scale associated with nonlinearity $l_{NL} = G_c / E \sim 333$ μm; the process zone associated with fracture is expected to be significantly smaller than this, and will be identified in the following.

2.3.3 Mixed-Mode I + III Fracture in the Hydrogel

Two types of specimens/loading conditions were considered for the experiments in the hydrogel. In the first loading configuration, a compressive loading that generated mode III and a negative mode I (closure of the crack) was applied; in fact, closure of the crack could be observed easily in the optically transparent gel specimens; this was followed by insertion of a wedge into the crack faces, generating an opening mode loading of the crack resulting in fracture under a combination of modes I and III (similar to the experiments on Homalite-100 reported in Section 2.2). The second loading configuration was a specimen under uniaxial tensile loading, with an inclined, part-through crack.

A. Confined Compression Experiments

Parallelepipedic specimens of dimensions $76.2\times76.2\times63.5$ mm^3 were prepared by casting the hydrogel (of the composition indicated in Section 2.3.1) into a glass mold. A notch that facilitates wedge loading was cast directly into the mold; this notch was oriented at an angle (typically at 25°) with respect to the faces of the specimen in order to facilitate the generation of a mode III loading by application of a constraint on the two opposite faces. After forming the hydrogel, a very sharp crack was introduced ahead of the V-notch using surgical scalpel that was mounted on a motorized stage to translate along the crack path with a constant speed, typically in the range of about 1-2 mm/s. Figure 2.19 shows a diagram of the specimen, the loading directions, and the arrangement of the two cameras used to observe the nucleation and growth of cracks. One camera (view #1) was positioned in the direction perpendicular to the side surface that was free and therefore provided an oblique view of the crack plane, and the other camera (view #2) was positioned below the specimen so as to be facing the parent crack front (viewing in the –***b*** direction). The loads required for both the confinement and the wedging were very small and difficult to measure; therefore, the exact mixed mode state could not be determined. Nevertheless, given the results from a collection of experiments that strongly confirm the hypothesis that the orientation of the daughter cracks is given by Eq.(1.4), corresponding to the orientation of the local principal tensile stress, we could infer the mode mixity from a measurement of the daughter cracks.

Figure 2.20 shows a time sequence of images from the two cameras. A video of this experiment is available as Supplementary Material G1. Since the gel is optically transparent, imaging the crack requires careful positioning of the lighting in such a way that only the light reflected (or scattered) from the crack front could be observed in the two cameras. Figure 2.20a shows images from view #1, an oblique view of the parent crack surface; the parent crack front is visible in the middle of image 1 as a bright white line identified by an arrow. A 2 mm scale bar is shown in the top right. The nucleation process of the daughter cracks can also be seen in this image, and is identified as the 1st group of nucleation towards the right side of image 1; with proper obliquity relative to the $-\boldsymbol{n}$ direction (parallel to the daughter crack plane), the daughter cracks should appear as straight lines as seen in the images (Note: except for perspective effects). Due to a small nonuniformity in the loading along the parent crack front, daughter crack nucleation begins in the right side of these images first, and then with continued wedge loading, causes further growth of the 1st group of daughter cracks and triggers further nucleation in their neighborhood along the parent crack front; two other groups are identified in the figure. Note that these daughter cracks correspond to type A daughter cracks. The absence of any connection between these cracks clearly reveals the absence of type B cracks. The propagation of nucleation sites along the parent crack front can be explained by the shielding along the parent crack front resulting from nucleation of a daughter crack (see Section 2.1.3): when the daughter crack is nucleated, it perturbs the stress state of the parent crack front portion around its location; this perturbation gives rise to the increasing of mode

I SIF locally and triggers the next nucleation to occur at the location next to the daughter crack.

A coarsening phenomenon similar to that observed in the experiments on Homalite-100 is also readily observable in the hydrogel; in fact, because the crack growth in these specimens is stable, it was possible to track the growth of the daughter cracks over long lengths. This is shown in the images in Figure 2.20b; the time sequence of images shown here is a continuation of the sequence in Figure 2.20a. Both views #1 and #2 are shown in these figures, one below the other as pairs. As the system of type A daughter cracks grows further, clearly some of the daughter cracks grow more at the expense of the closest neighboring daughter cracks through an elastic shielding mechanism already discussed in Section 2.2.3; the surviving daughter cracks continue to grow in the plane parallel to each other maintaining the same plane. The daughter cracks could not be grown further because the wedge used for loading the crack approached the tip of the parent crack and obliterated the traces of the daughter crack. We will explore continued growth in another configuration – the tensile loading test in Section 2.3.3B.

In all the experiments reported here, the crack was introduced either by a notching or a cutting process; as a result, the crack is equivalent to a blunt notch. The question of whether this results in a fundamentally different response from a sharp crack was addressed by Ronsin et al (2014); they performed a step jump experiment in which the energy release rate was altered abruptly so as to transition from a smooth extension of the crack front to a fragmented crack front. The resulting fragmentation was shown to be homogeneously nucleated from the straight crack front; Ronsin et al. (2014) attributed this to a nonlinear material behavior in the vicinity of the crack tip. We examine the issue of the sharpness of the parent crack front. Specimens for wedge loading were prepared as described above and then subjected to a precracking procedure: the specimen was loaded under mode I using the wedge. The wedge loaded cracks still fragmented due to heterogeneities in the initial crack front; however, crack growth was planar and large segments of the crack front were indeed sharp natural mode I cracks (see Figure 2.21). The mode I loading was stopped before the crack had penetrated by about 15 mm; the specimen then was unloaded; the confining load was applied, and then the wedge loading was resumed in order to generate a mixed mode I + III crack. The evolution of the crack under this mixed mode I + III loading is shown in Figure 2.21. Image 1 corresponds to the crack front at the location attained at the end of the precracking procedure. The nucleation starts at a very small scale as can be identified in images 2 -4. The last image on the left column of Figure 2.21 (Image 7) shows that crack front fragmentation occurred everywhere along the natural parent crack front. The resolution of these images is not high enough to identify that these are the type A daughter cracks, but becomes apparent as the loading progresses, and the nucleated cracks grow exhibiting coarsening: it can be seen clearly that the number of daughter cracks decays through each image from 9 to 14. Furthermore, each crack grows in its own plane. The coarsening schema observed within the hydrogel experiment exhibits a similar coarsening scenario as that observed in other experiments for Homalite-100 (Section 2.2.2) and hydrogel with a scalpel-cut crack front.

In order to examine the nucleation of the daughter cracks in greater detail, the unloaded specimen was extracted from the testing device, and observed in a Keyance microscope that provides fully focused images of three-dimensional objects by a z-focusing technique. We note that the specimen was not broken, sliced or altered in anyway; the crack front region was kept open by keeping the wedge used for loading still in place and viewed in the microscope. One image of the crack front region is shown in Figure 2.22a. The parent crack front and surface are identified in the figure. The parent crack surface was optically smooth, implying that any roughness would be in the submicron range. Nucleation of daughter cracks is clearly visible in this image. Higher magnification views of the nucleation region are shown in Figures 2.22b, 2.22c and 2.22d; illumination was adjusted so as to be able to focus on the primary nucleation. It is clear from these two sets of images that initiation of daughter cracks under mixed mode I + III occurs by the rather abrupt nucleation of facets at a fixed length scale – in this case, varying between 20 and 40 μm; Comparing this length scale to the nonlinearity scale $l_{NL} \sim 333\mu m$, it can be argued that the fracture process scale is at least an order of magnitude smaller. The absence of daughter cracks at lengths smaller than ~20 μm (noting that the optical images can distinguish features as small as 1 μm) suggests that the formation of daughter cracks does not follow the linear instability mechanism suggested by Leblond et al. (2011), but is more directly a nucleation at a specific scale as indicated by Ronsin et al. (2014) for gels and Section 2.1 for brittle polymers. Coarsening – regular arresting of the daughter cracks – is also observed in Figure 2.22a; however, this is not always through a doubling of the spacing, as would be implied by shielding of just the nearest neighbor of each daughter crack. While the first family of daughter cracks are spaced about 20 to 40 μm, the second family is spaced at about 200 μm; the last two families visible in Figure 2.22a are at spaced about 1.5 mm and 6 mm apart, respectively. The linear elastic shielding calculations in Section 2.1.3 indicated only nearest neighbors are influenced; it appears that the nonlinear kinematics of the gel may have a role in how the shielding decays in this material and needs to be explored further.

We complete this section with two open questions: first, in the experiments reported in this section, there was a significant compressive stress parallel to the plane of the daughter cracks that may play a role in the suppression of the type B cracks. Does this same behavior persist in the absence of such compressive stress? Second, how long does the coarsening behavior continue? It is clear that at some point the energy associated with elastic deformation of the bridging regions (where the type B cracks did not form) must become large enough to trigger failure in these regions (see discussion in Lin et al. 2010). We address these issues in the next section.

B. Uniaxial Tension Experiments

Hydrogels are soft and in general failure occurs at the grips in the tension test configuration. Thus special care is needed in designing the holding fixture for the specimen. Ronsin et al. (2014) overcame this limitation by using Velcro strips and casting the gel into the hooks of the Velcro. We designed a dumbbell shape mold which is composed of two outer hollow cylinders and two flat rectangular bocks in the center (Figure 2.23). The top and bottom of the mold are covered by two flat plates to which a half cylinder is attached (to reduce the width of the central portion of the specimen). After the gel is poured into the mold and cured completely, the two flat plates on both sides and the top and bottom plates could be removed to reveal the gel specimen. Two hollow cylinders at the ends are kept together with the gel and play the role of the loading grips. Proper contouring of the corners in the end grips prevents any tendency for the gel to tear or crack at any location. This procedure generated specimens that were suitable for tensile tests to average strain levels of about 20% and was adequate for the fracture tests considered. A sharp crack, oriented with an angle θ with respect to the horizontal direction, is introduced by using sharp surgical scalpel mounted on a motorized stage, as indicated in Section 2.3.3A. The crack front has a curved shape at the ends and is straight in the central portion. This curved part-through crack eliminates (or minimizes) the mode II component of loading, except near the curved portions. Our focus will be on the central portion of the specimen. Typically, the crack depth was about 0.4 of the specimen thickness. We will refer to this as the edge-cracked tension specimen. The specimen was mounted in an Instron testing machine; the weight of the end grips, and the high compliance of the gel specimen, dictated that this mounting process had to be performed carefully – this required basically keeping the rigid mold blocks in place until the specimen was fully mounted in the machine. Two video zoom cameras were positioned in order to visualize the crack front as described in Section 2.3.3A, one providing an oblique view of the crack plane (view #1) and the other providing a view of the crack front (view #2).

A series of experiments was performed with different crack orientations $\theta = 0^\circ, 3^\circ, 10^\circ, 20^\circ, 30^\circ$. The load vs the cross-head displacement was monitored with the load cell in the testing machine; one example from a test with $\theta = 0^\circ$ is shown in Figure 2.24. The load level at the onset of crack initiation is indicated by the red dot; note that the crack growth is stable under displacement control all along the path. The critical load at onset of crack growth for the specimen with crack angle $\theta = 0^\circ$ was used to calculate the fracture toughness. This result was described in Section 2.3.2; the fracture toughness was estimated to be $K_{IC} = 1.68$ kPa m$^{1/2}$.

All the edge-cracked tension specimens with crack angles $\theta \neq 0^\circ$ showed quite similar behavior: the parent crack front fragmented into facets or daughter cracks; only type A daughter cracks were nucleated; these cracks were oriented in the direction nominally perpendicular to the tension loading direction; the daughter cracks initiated at a finer scale and coarsened as they grew. So, all features that were observed in the confined experiments described in Section 2.3.3A, were also observed in the edge-cracked tension experiments, in spite of the absence of the confining stress. Hence we conclude that the confining compression is not necessary for the suppression of type B cracks. Also, *there was no significant rotation of the type A daughter cracks* as it extended from the initial crack. This is once again due to the absence of mode II loading at the crack front.

The only remaining question relates to the continued coarsening of the daughter crack pattern; this is examined next. A sequence of images of daughter crack propagation and coarsening from an edge-cracked tension test with $\theta = 20^\circ$ is shown in Figures 2.25. The complete video sequence of this test is included as Supplementary Material G2 to this dissertation. The numbers indicate frame numbers, with each frame corresponding to 5 s time interval; the length scale for these images is shown in frame 239. It is clear that at frame 190, the daughter crack nucleation, growth and coarsening has already progressed to about 2 to 3 mm from the parent crack front, with the largest spacing of about 2 mm. The nonuniformity of daughter crack extension along the parent crack front is the result of the curved cracks at the two ends being of slightly different shapes. With further increase in the global loading, the daughter cracks continue to grow, rather slowly at first. However, near the peak load, the crack growth rate increases as can be observed from the inter-frame time intervals. From about frame 231, the daughter cracks grow under decreasing global load (the process is still stable under the displacement-controlled test conditions). Coarsening, however, appears to have stopped! As can be seen from Figure 2.25, the spacing remains at about 2 mm, and the daughter cracks grow to a length of about 15 mm. A careful examination of the video images of these experiments indicated that the halt to the coarsening is dictated by the cracking of the unbroken remnants of the parent crack when the daughter cracks have progressed far ahead. The fate of one of the daughter cracks is captured in frames 241 through 249 and is identified by the white arrow in each image in Figure 2.25. Between frames 241 and 245, the identified daughter crack stops growing while its neighbors continue ahead. But between frames 245 and 247, the back of the parent crack begins to propagate and tears into this daughter crack; this is what causes the end of coarsening! As the leading edge of the daughter cracks continue to propagate, the type B or bridging regions get cracked by the fracture of the remnants of the parent crack.

The stopping of the coarsening can also identified in *post-mortem* images of the fracture surfaces from the same specimen, shown in Figure 2.26 at two different magnifications. The color contours are height maps relative to the parent crack surface as the datum; the lower image shows a higher resolution image of the region indicated by the dashed rectangle. It is clear that the first few families of daughter cracks coarsen and lead to increasing spacing; however, beyond a spacing of about 2 mm, the coarsening stops, and a nearly steady growth appears possible, in this example until the far end of the specimen (a distance of about 15 mm). Figures 2.27a and 2.28a show similar topographic images of the fracture surfaces from specimens with $\theta = 3^{\circ}, 10^{\circ}$. Line traces along specific lines parallel to the initial crack front are also shown in Figures 2.27b and 2.28b; these profile traces, however, are to be interpreted carefully since we know from the real-time images that the crack did not occupy this line at the same time instant. To clarify this, oblique view images of the crack plane (view #1) at some stage of the growth of the crack are shown in Figures 2.27c and 2.28c. Clearly, these images indicate that the angle ϕ_c is consistent with all fragmented cracks in each test, and that the number of fragmented daughter cracks decreases with increasing distance from the parent crack. For the case of $\theta = 3^{\circ}$, there is a tendency for the fragments of drift and merge into each other at very long distances from the parent crack front, but for $\theta = 10^{\circ}, 20^{\circ}$, the coarsening stops beyond a certain distance from the original parent crack and propagates in a self-similar manner with a system of daughter cracks ahead of the main crack. This is an important aspect of mixed-mode I + III; when the coarsening of the daughter crack ends, a self-sustaining pattern of cracking is established near the crack tip and further steady growth becomes possible.

The case of $\theta = 0^{\circ}$, resulting in pure mode I creates a "cross-hatching" pattern that has been examined by Tanaka et al. (1998) and Baumberger et al. (2008). These experiments, however, present real-time visualization of the development of these patterns.

The images corresponding to pure mode-I are shown in Figure 2.29. The topographic image and a few representative profile traces are shown in Figures 2.29a and 2.29b, respectively; these reveal that the crack surface is flat in each segment, indicating mode I fracture, but that each segment is at a slightly different level. Figures 2.29c and 2.29d show an oblique view of the crack plane (view #1) and a fontal view of the crack along the –***b*** direction (view #2). the "cross-hatch" pattern can be identified as step between cracks in the different segments; the fronts of fragments 1 through 6 are identified in these figures. The fracture surfaces are also visible in both images; clearly, crack 1 leads the pack. Cracks 2 and 4 trail crack 1; crack 5 trail crack 4 and finally crack 3 leads crack 2. Clearly, the direction of the cross-hatch is now readily understood: a crack lagging on the left (from the perspective of the crack propagation direction) drags the cross-hatch to the left, while a lagging crack to the right drags the cross-hatch to the right; this is observed consistently in all the cracks visualized. This is simply a manifestation of the fact that the leading crack wants to spread into the region of the lagging crack. Coalescence of these cross-hatching lines is visible in Figure 2.29a, typically in locations where the height differences are large.

2.4 CONCLUSIONS

The criterion for initiation and growth of cracks under mixed-mode I+III loading has been examined further in this chapter. Following on the geometry suggested for such investigations by Goldstein and Osipenko (2012), we explored alternative geometries that can be tailored to address specific questions related to the initiation of cracks. All designs were supported with calculation of the stress intensity factors using a boundary element code (Li et al, 1998). With the first design, mode II was nearly completely eliminated, and the value of the mode III stress intensity factor experienced a change of sign from negative to positive in the location where the mode I stress intensity factor attained a maximum.

This allowed examination of the question of existence of a threshold for crack front fragmentation. The second design, in which the mode I stress intensity factor was negative caused crack that nucleated to be arrested, permitting examination of the spacing between the nucleated crack front fragments. Experiments were performed on two materials: glass and H-100, both of which exhibit brittle or quasi-brittle fracture behavior. Recovered specimens were examined to reveal the geometry of the nucleated crack front fragments. From this study, two major conclusions were reached:

i. Cracks subjected to combined modes I+III loading cause fragmentation of the crack front *without any threshold*; perturbations as small as $K_{III}^{\infty}/K_{I}^{\infty} \sim 0.001$ cause nucleation of fragmented daughter cracks.
ii. The distance between the fragments is dictated by the length scale corresponding to the decay of the elastic field; this decay depends on the thickness dimension of the parent crack from which the daughter fragments are nucleated. The thickness of the parent crack is governed by the local radius of curvature of grooves for a machined crack or a similar characteristic length.

Specially designed specimen configuration that provides a combination of $\left(K_{I}^{\infty}, K_{III}^{\infty}\right)$ was considered in order to examine the growth of the nucleated daughter cracks. A combination of confining pressure and a wedge load allowed generating mixed mode crack growth, but with significant confining compression in one orientation that allowed parallel type A, opening mode cracks to nucleate and grow. Microscopic examination was used to identify the structure of the nucleated daughter cracks. Another set of experiments was performed on a gelatin based hydrogel; the transparency of this material allowed good visualization of the development of the daughter cracks, both during nucleation and growth. Based on these experiments, it was concluded that:

- Type A daughter cracks are nucleated when a critical loading condition is attained and are not formed through the growth of unstable modes from a smooth extension of the parent crack.
- The orientation of the type A cracks is perpendicular to the line of major tension in the vicinity of the crack tip; the estimate of Pollard et al. (1982), given in Eq.(1.4), is adequate in identifying this orientation. In the absence of mode II loading, type A cracks do not rotate, but maintain their orientation.
- Type B cracks are not nucleated under the confined compression-shear loading or the edge-cracked tension experiments.
- Coarsening of the spacing between the type A cracks occurs through elastic shielding; a simulation with a boundary-element-code was used to demonstrate such shielding.
- Final failure that occurs through break-up of the bridging regions between the type A cracks that could not be observed in the case of the Homalite-100, but was clearly visualized in the case of the gel specimens.

Based on this collection of experiments, the sequence of events that govern the initiation and growth of cracks under mixed-mode I + III is now clearly revealed to be composed of the following steps:

- First, type A daughter cracks are nucleated from random defects in the vicinity of the parent crack. The spacing is governed by the characteristic dimension of the parent crack.
- Second, fluctuations and elastic interaction result in shielding of some subset of the nucleated daughter cracks; some daughter cracks are arrested.

- As the daughter cracks grow farther, the parent crack, pinned at the original position, experiences increased stress intensity factor and the bridging regions begin to crack and the parent crack front advances towards the daughter cracks.
- It is now possible to set up a new structure, where the leading edge is formed by the fragmented type A daughter cracks, while the trailing edge is created by the fracture of the bridging regions between the type A daughter cracks. In the absence of any mode II, there is no driving force to alter this picture, and the process can sustain itself and break the entire specimen creating a system of echelon cracks under the combined mode I + III loading.

In the next chapter, we will discuss the phase-field model with the aim of the initiation and growth of cracks under combined mixed-mode I+III discussed in the current chapter.

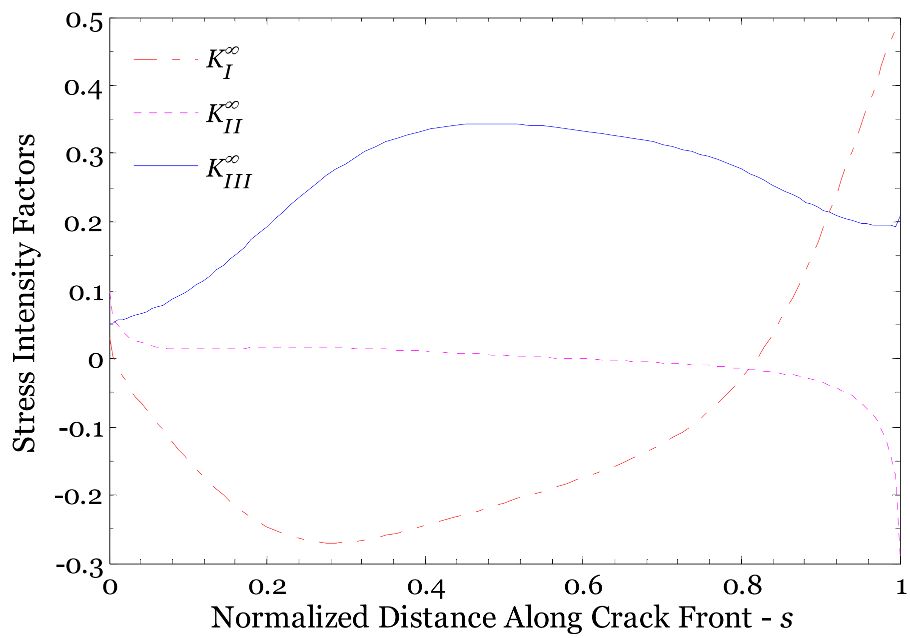

Figure 2.1. The variation of the stress intensity factors $K_I^{\infty}(s), K_{II}^{\infty}(s), K_{III}^{\infty}(s)$ along the crack front in the Goldstein-Osipenko configuration with slant cracks with $\gamma = 15°$.

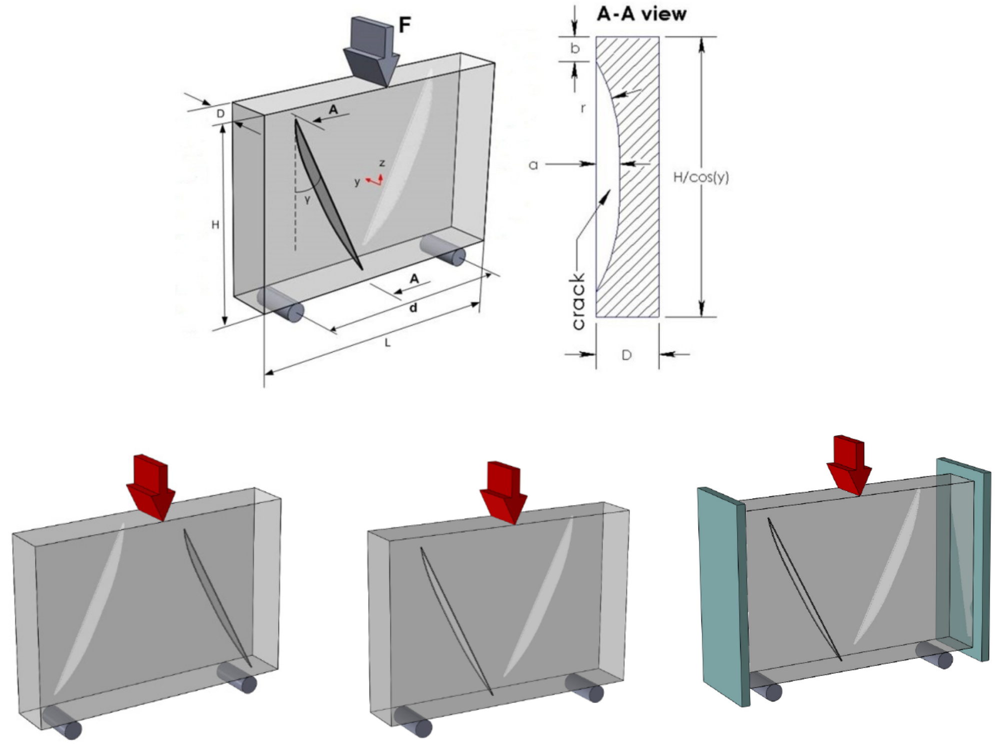

a) Specimen Type I b) Specimen Type II c) Specimen Type III

Figure 2.2. Geometry of modified Goldstein-Opisenko configurations. The crack fronts are curved and break the surface on planes $y = \pm D/2$. Specimen Type II is obtained merely by flipping the loading about the xy-plane.

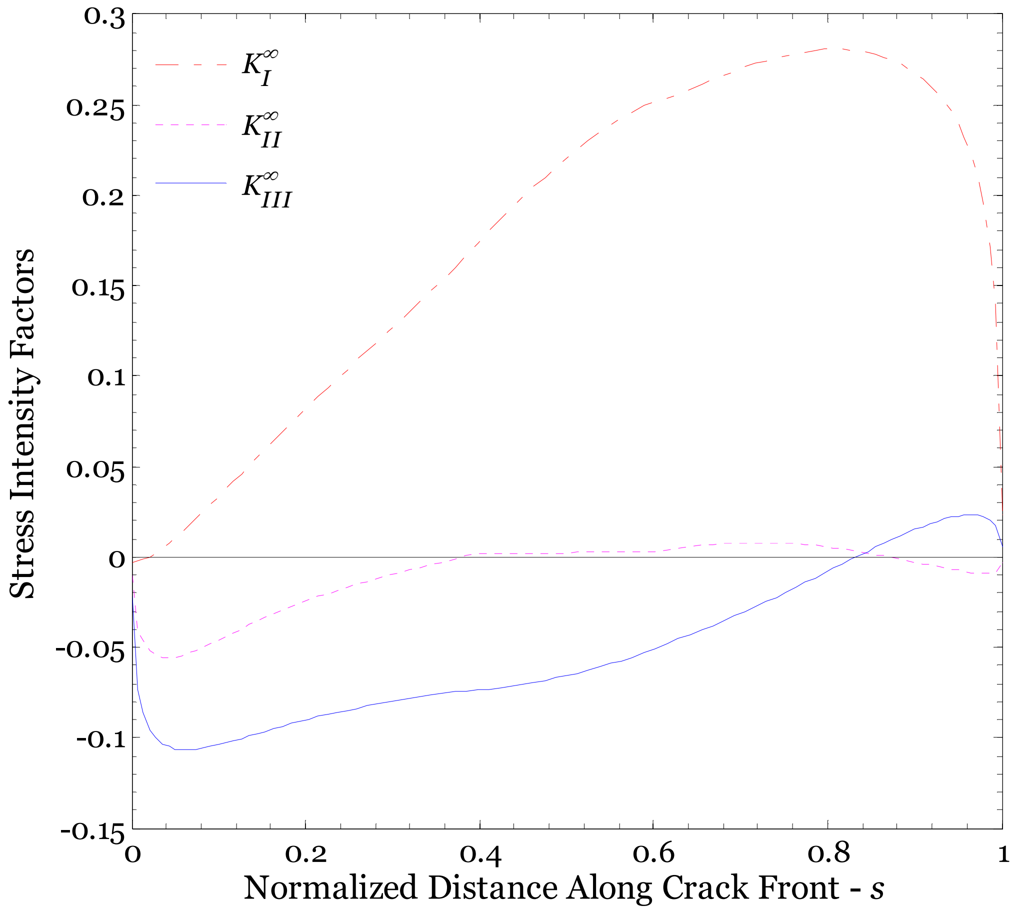

Figure 2.3. The variation of the stress intensity factors $K_I^\infty(s), K_{II}^\infty(s), K_{III}^\infty(s)$ along the crack front for specimen type I. The origin of s is located at the top of the specimen. Elastic properties of glass have been assumed in the simulations. The specimen redesign has eliminated the concentration of mode II stress intensity factor where the crack meets a free surface ($\gamma = 26°$).

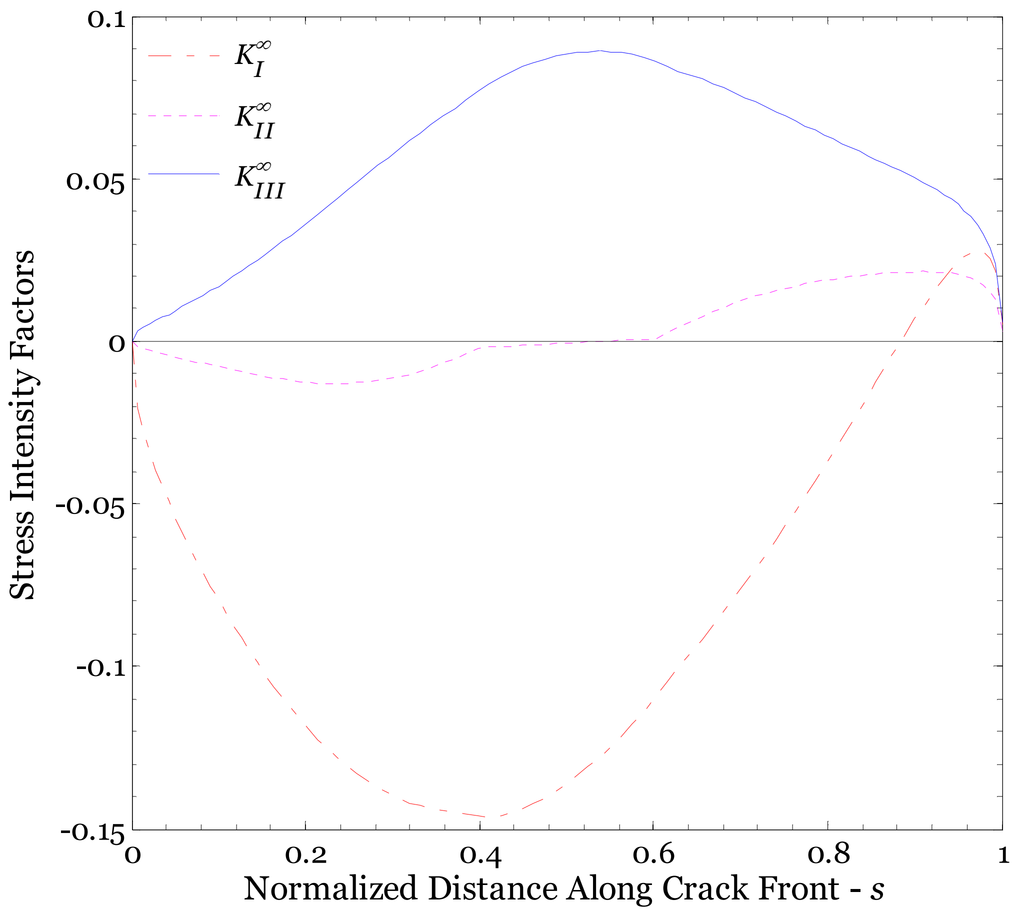

Figure 2.4. The variation of the stress intensity factors $K_I^\infty(s), K_{II}^\infty(s), K_{III}^\infty(s)$ along the crack front for specimen type II. The origin of s is located at the top of the specimen. Elastic properties of Homalite-100 have been assumed in the simulations ($\gamma = 26°$).

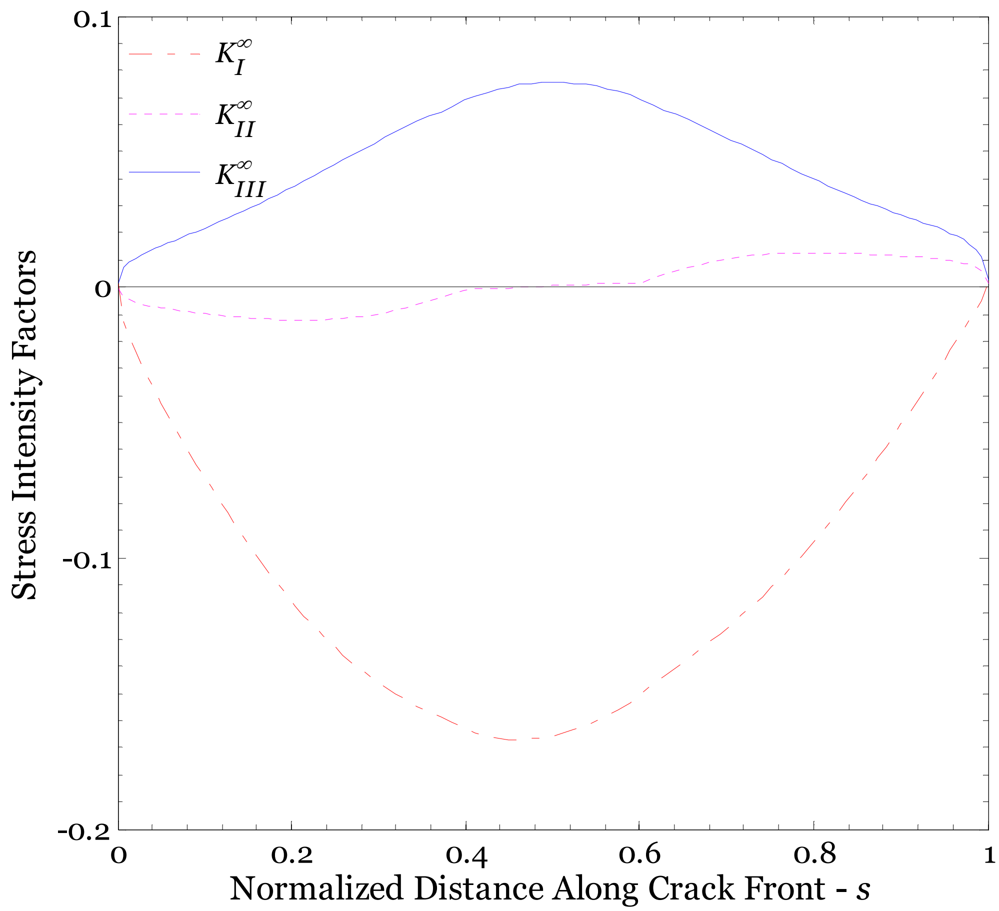

Figure 2.5. The variation of the stress intensity factors $K_I^\infty(s), K_{II}^\infty(s), K_{III}^\infty(s)$ along the crack front for specimen type III. The origin of s is located at the top of the specimen. Elastic properties of Homalite-100 have been assumed in the simulations ($\gamma = 26°$).

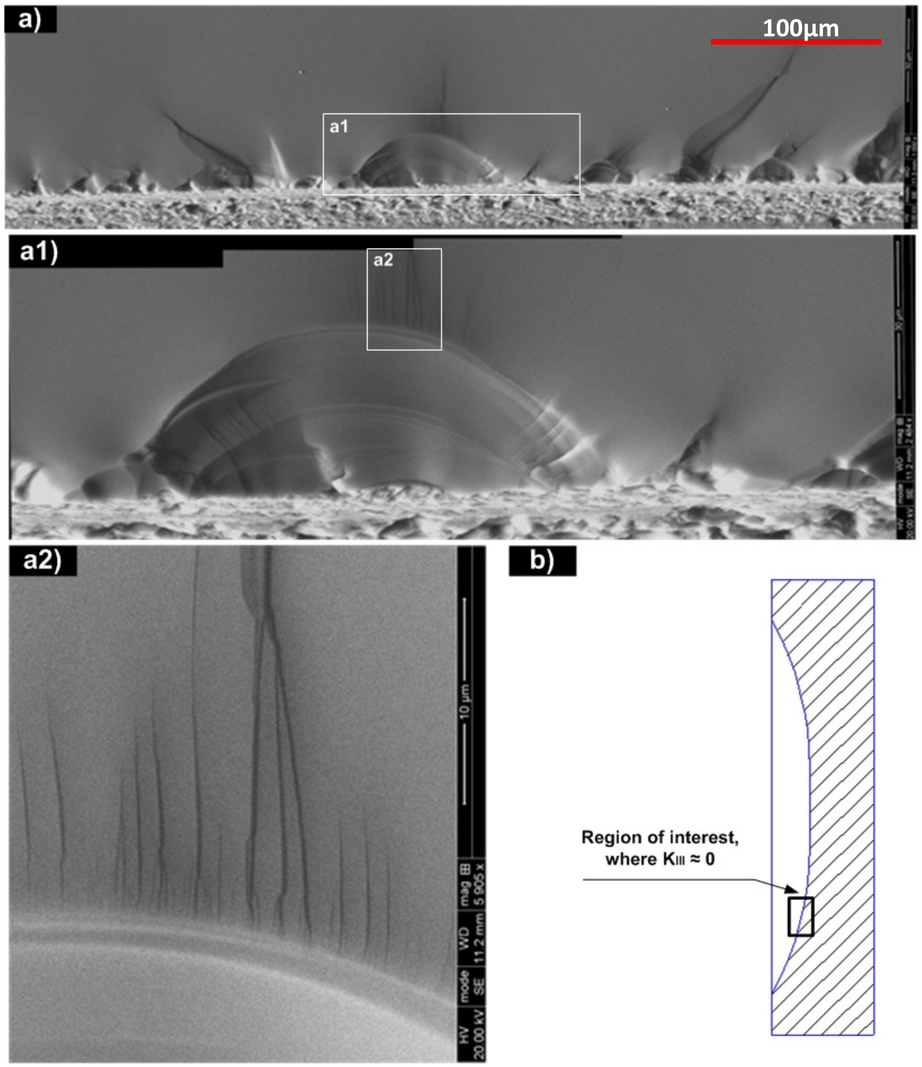

Figure 2.6. (a) Fractograph of glass specimen type I, showing the region near the transition point. (a1) shows a magnification of the boxed region in (a); (a2) shows a magnification of the boxed region in (a1). (b) identifies the region of interest (near the transition point) where there is a transition from positive K_{III}^{∞} to negative K_{III}^{∞}.

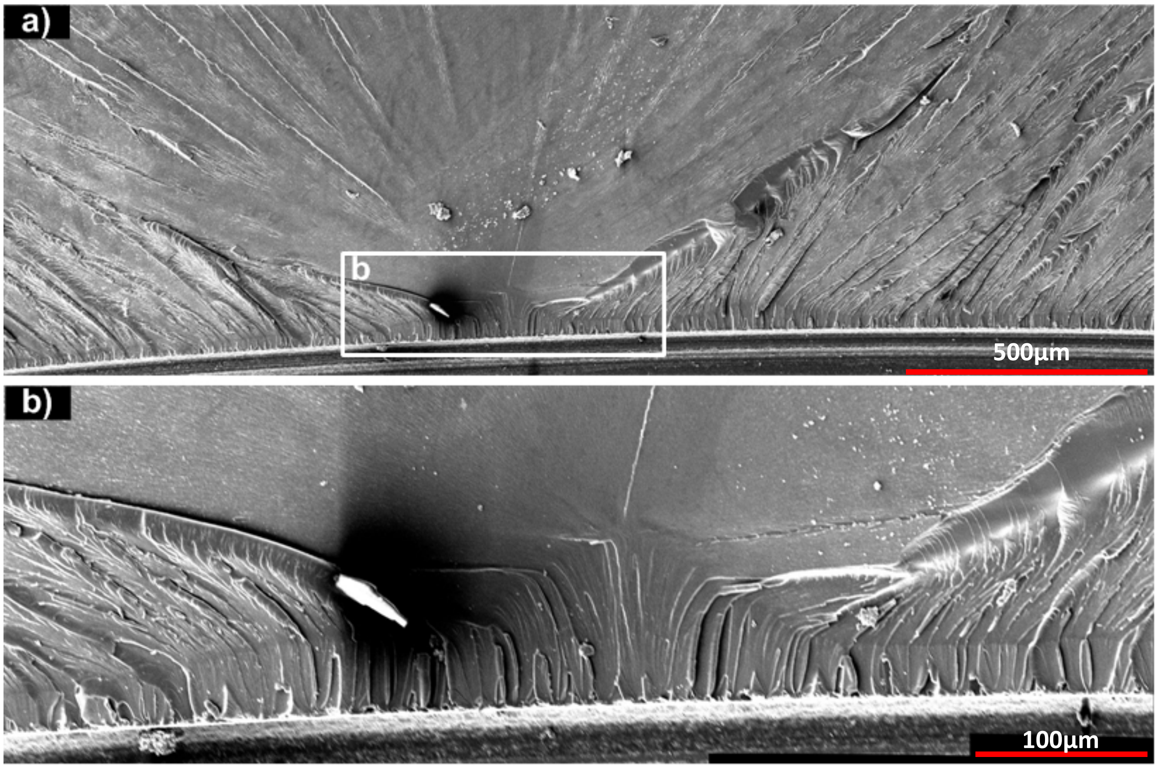

Figure 2.7. Fractograph of Homalite H-100 specimen type I, showing the region near the transition point. (b) Shows a magnification of the boxed region in (a).

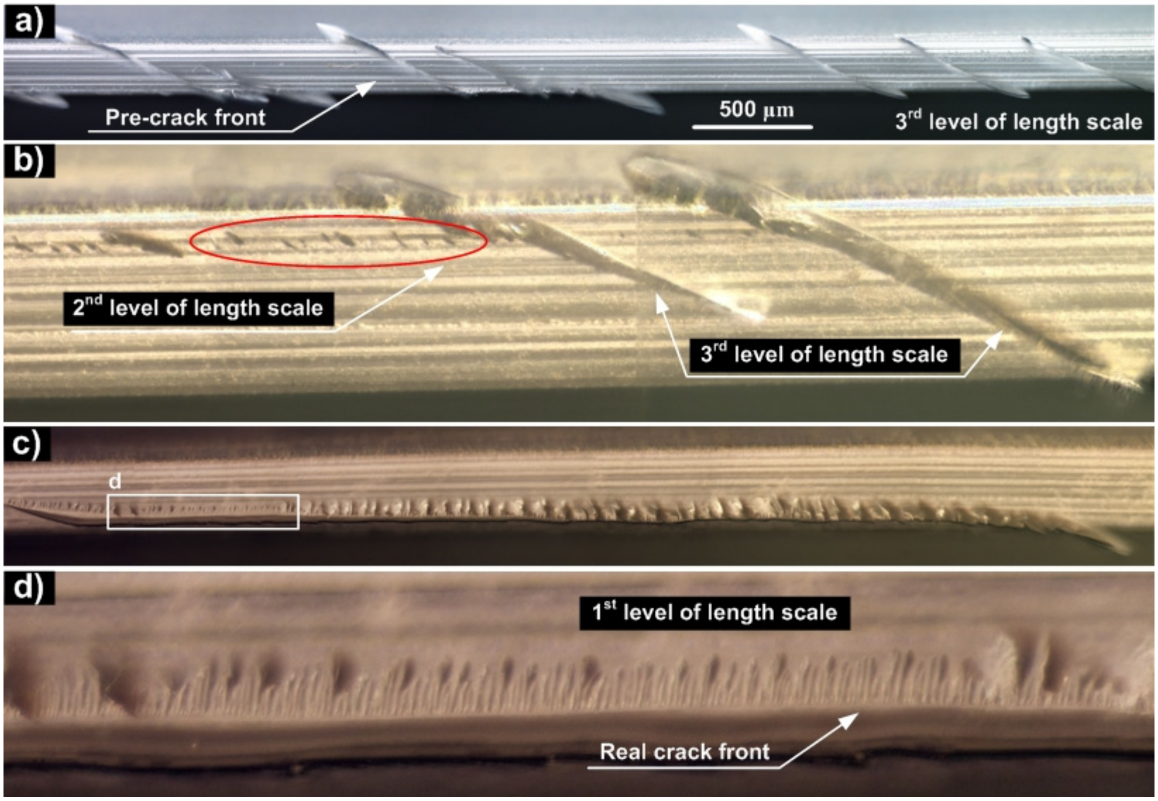

Figure 2.8. Cascading length scales of fragmentation spacing. (a) Nucleation along the pre-crack front on the scale of the thickness of the machined crack (A similar image with higher resolution is provided in Supplementary Material H). (b) Nucleation along the pre-crack front influenced by the width of the groove lines in the machined crack. (c) Nucleation along a natural crack front. (d) A magnified view of the boxed region $(100\mu m \times 500\mu m)$ indicated in (c).

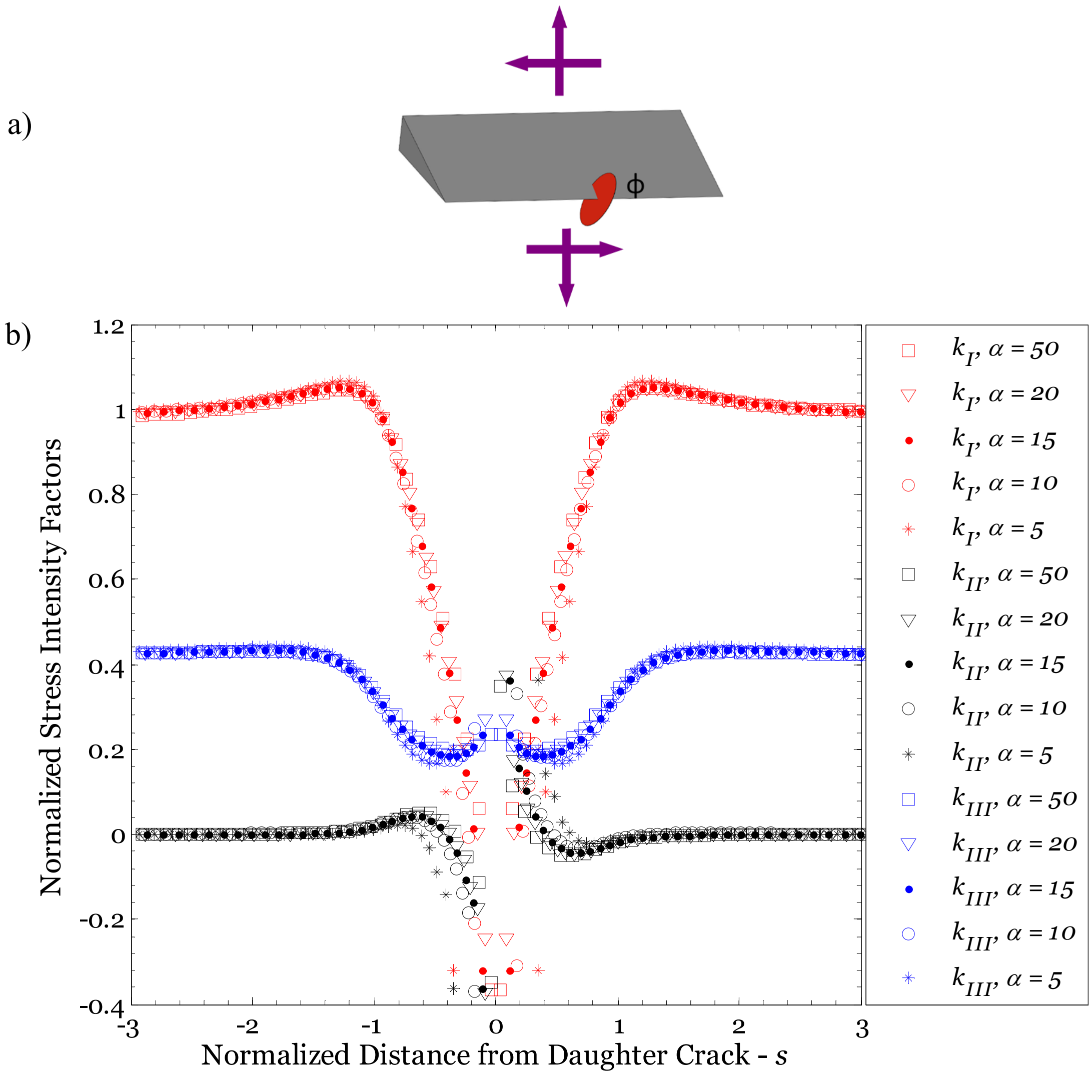

Figure 2.9. (a) Schematic diagram indicating the parent crack under a mixed mode loading, with a daughter crack that nucleated at the center. (b) Change in crack tip SIFs with daughter cracks size $a_{\text{micro}} = \alpha r_{\text{micro}}$. The daughter crack tip was idealized by a rounded geometrical feature $r_{\text{micro}} = 12.7 \ \mu m$ in the simulations. The parent crack is loaded such that $K_{III}^{\infty} / K_{I}^{\infty} = 0.42$ (to produce the twist angle $\phi = 35°$). The distance along the parent crack front from the daughter crack is normalized by a_{micro}.

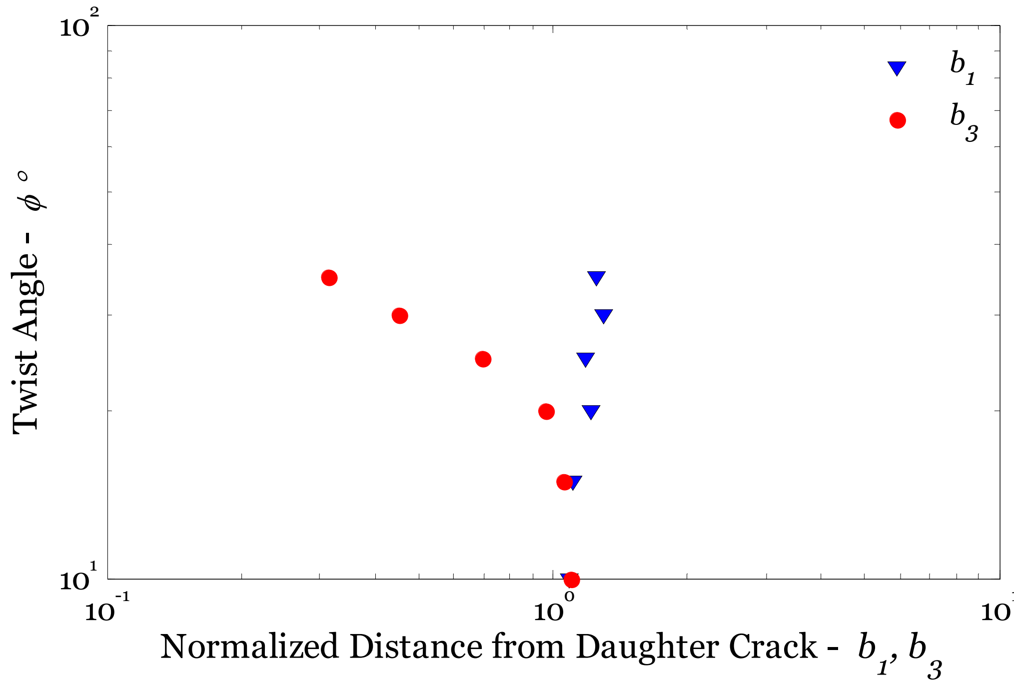

Figure 2.10. Location b_1 of maximum k_I and b_3 of minimum k_{III} for different daughter cracks angles ϕ. The daughter crack tip was idealized by a rounded geometrical feature $r_{micro} = 12.7$ μm, with crack size $a_{micro} = \alpha r_{micro}, \alpha = 20$ in these simulations.

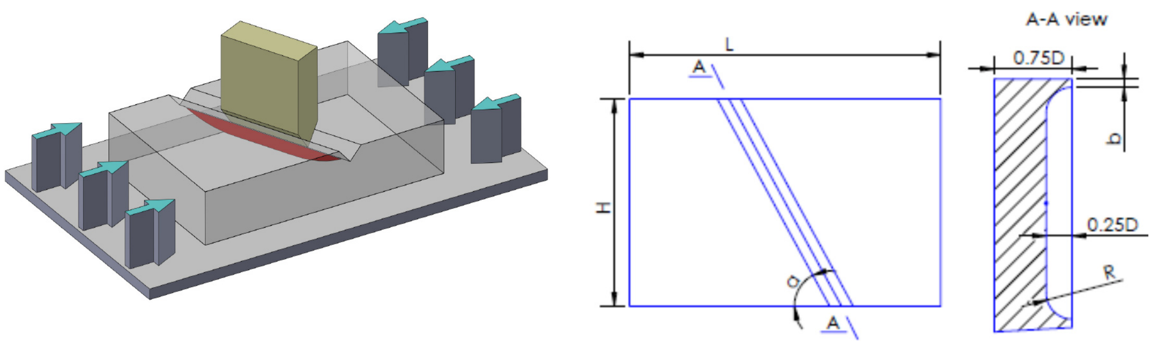

Figure 2.11. Geometry and loading configuration of the confined shear test. The crack front is curved and breaks the surface at the edge of the V-notch. Opening mode loading is produced by inserting the wedge into the V-notch; the compressive load on both sides causes the out of plane shear mode and also creates the global compressive stress state around the machined crack front. The combination of the two loading conditions results in a positive mode I stress intensity factor and a large mode III stress intensity factor.

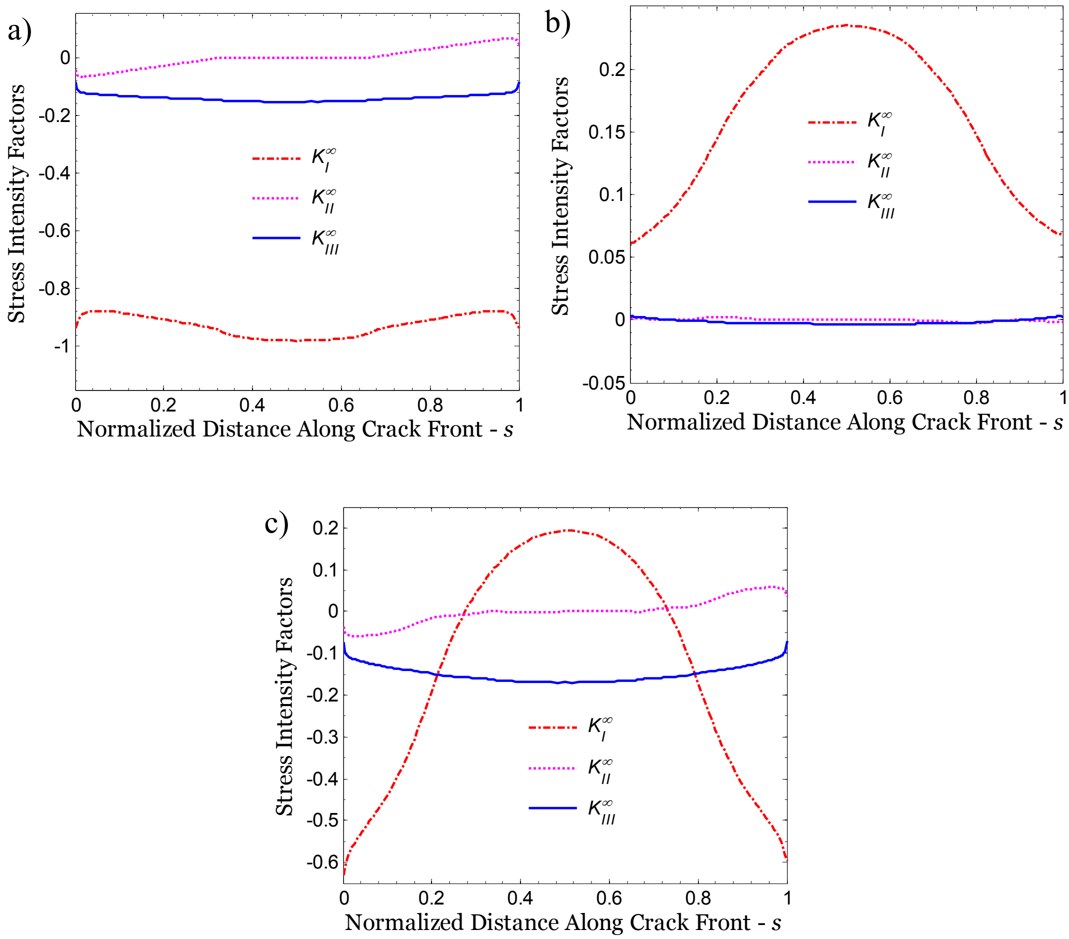

Figure 2.12. The variation of the stress intensity factors $\left(K_I^\infty(s), K_{II}^\infty(s), K_{III}^\infty(s)\right)$ along the crack front for the confined shear test specimen. Elastic properties of Homalite-100 have been assumed in the simulations. (a) The specimen is under compressive load of magnitude 1 unit,(b) the specimen is under wedge opening load of magnitude 1 unit and (c) a superposition of wedge and compressive loads with the ratio 5:1 respectively. This results in a positive mode I stress intensity factor and a large mode III stress intensity factor.

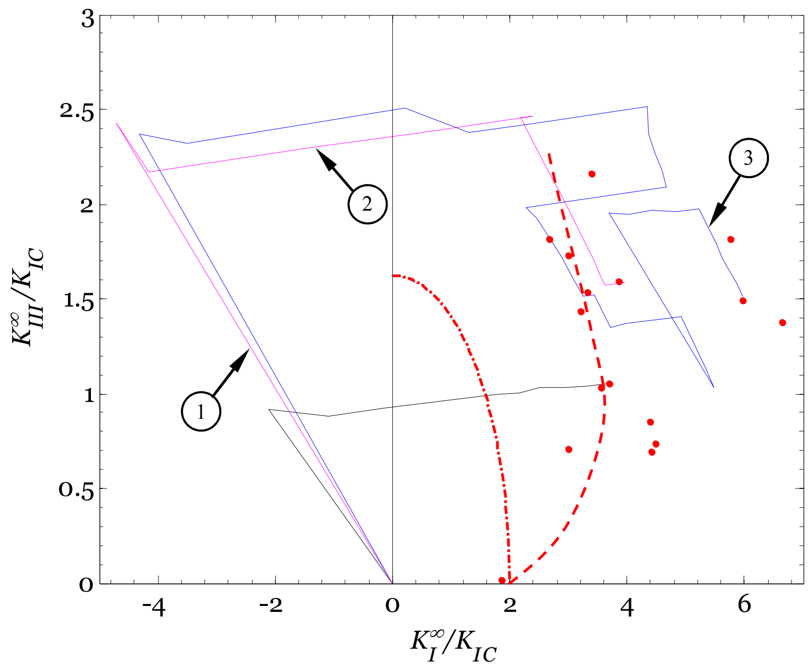

Figure 2.13a. Probing the failure envelope for mixed-mode I + III loading. The magenta, blue and black lines show the loading paths for three representative specimens. The red circular points represent the failure conditions for the tested specimens. The red dash-dot line provides a suggested failure envelope corresponding to Eq.(1.4), while the red dashed line represents the lower-bound from the data for the blunt crack. The numbers 1, 2, 3 correspond to confined load, wedge load and relaxing of the confined load path, respectively.

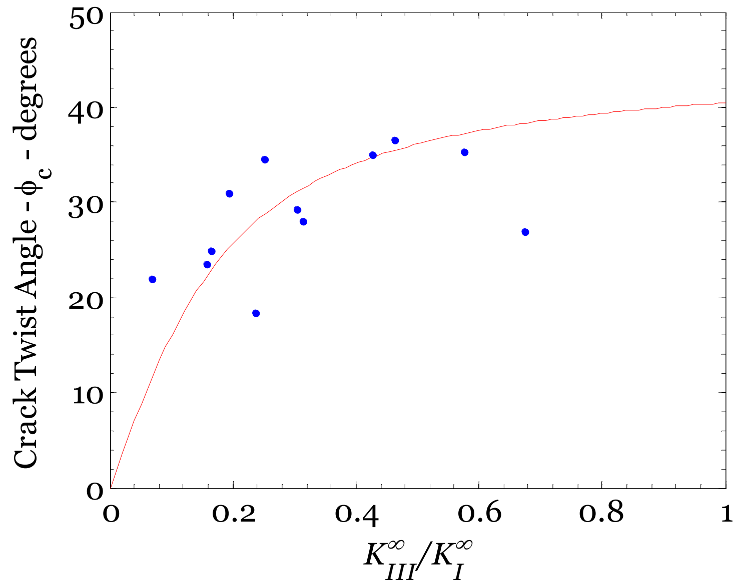

Figure 2.13b. Variation of the crack twist angle with ratio of mode III to mode I loading. The blue circular points represent the twist angles for the tested specimens; the red line provides the twist angles corresponding to Eq. (1.4).

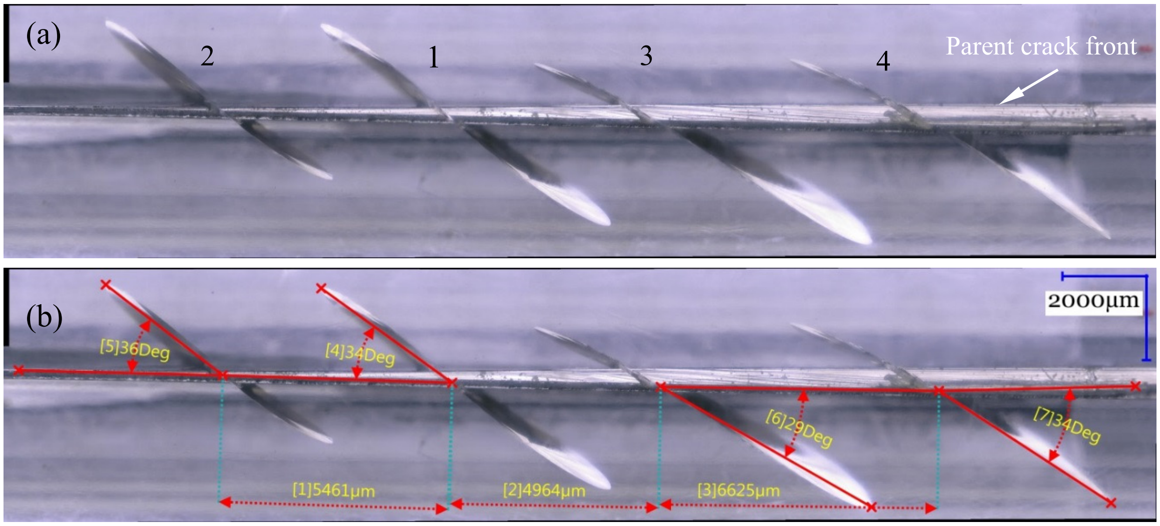

Figure 2.14. (a) Image of nucleated daughter cracks viewed in the –***b*** direction. The sequence of nucleation is indicated by the numbers. (b) Same image as in (a), with distances and angles marked.

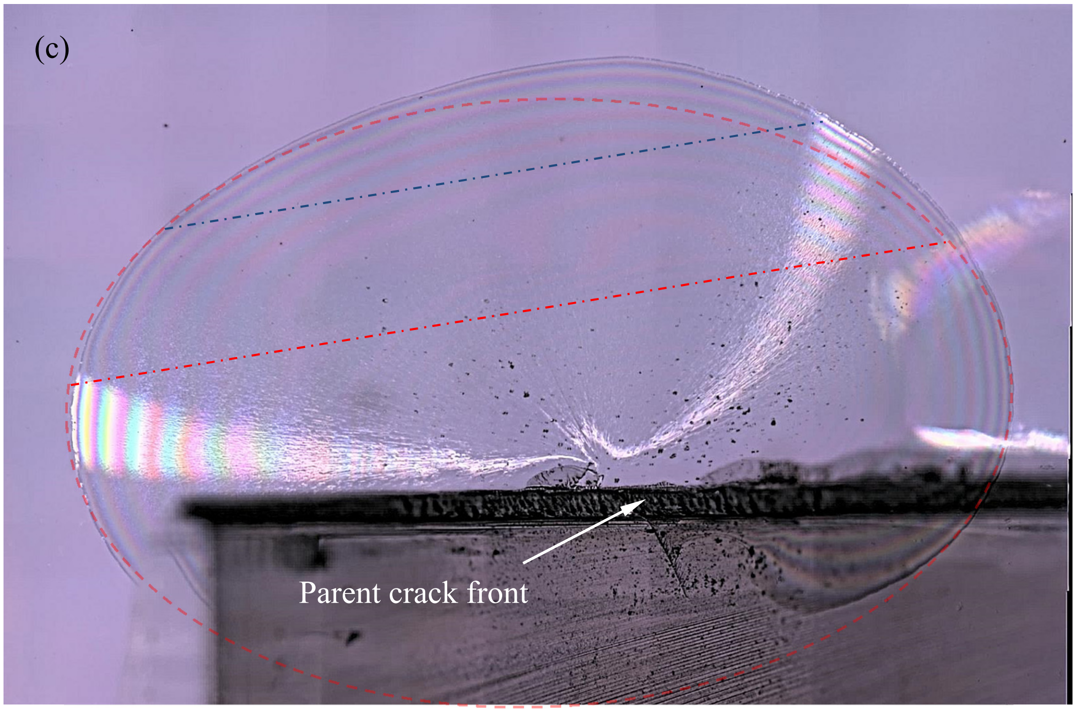

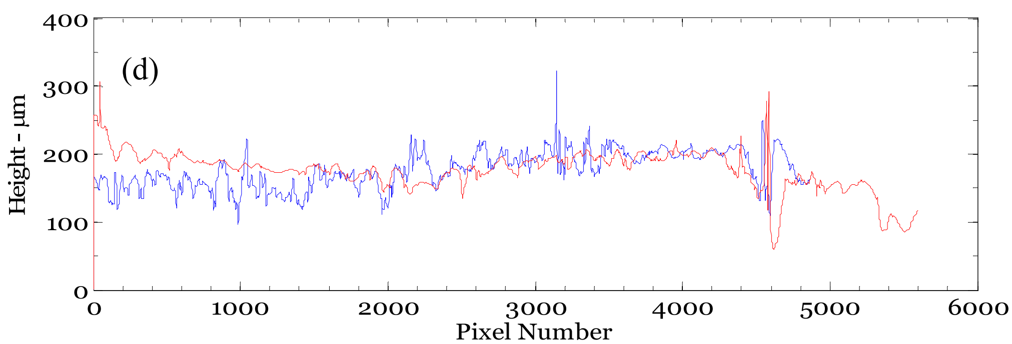

Figure 2.14. (continued). (c) Optical microscope image of daughter crack #4, viewed perpendicular to the surface of the daughter crack. The width of the field of view is ~6.75 mm. The color fringes are formed by reflection from the two crack surfaces, and indicate the crack opening profile. (d) Height variation from a nominal datum along the blue and red lines marked in (c); note that the height variation is within $\pm 100\mu m$ over a span of about 6 mm.

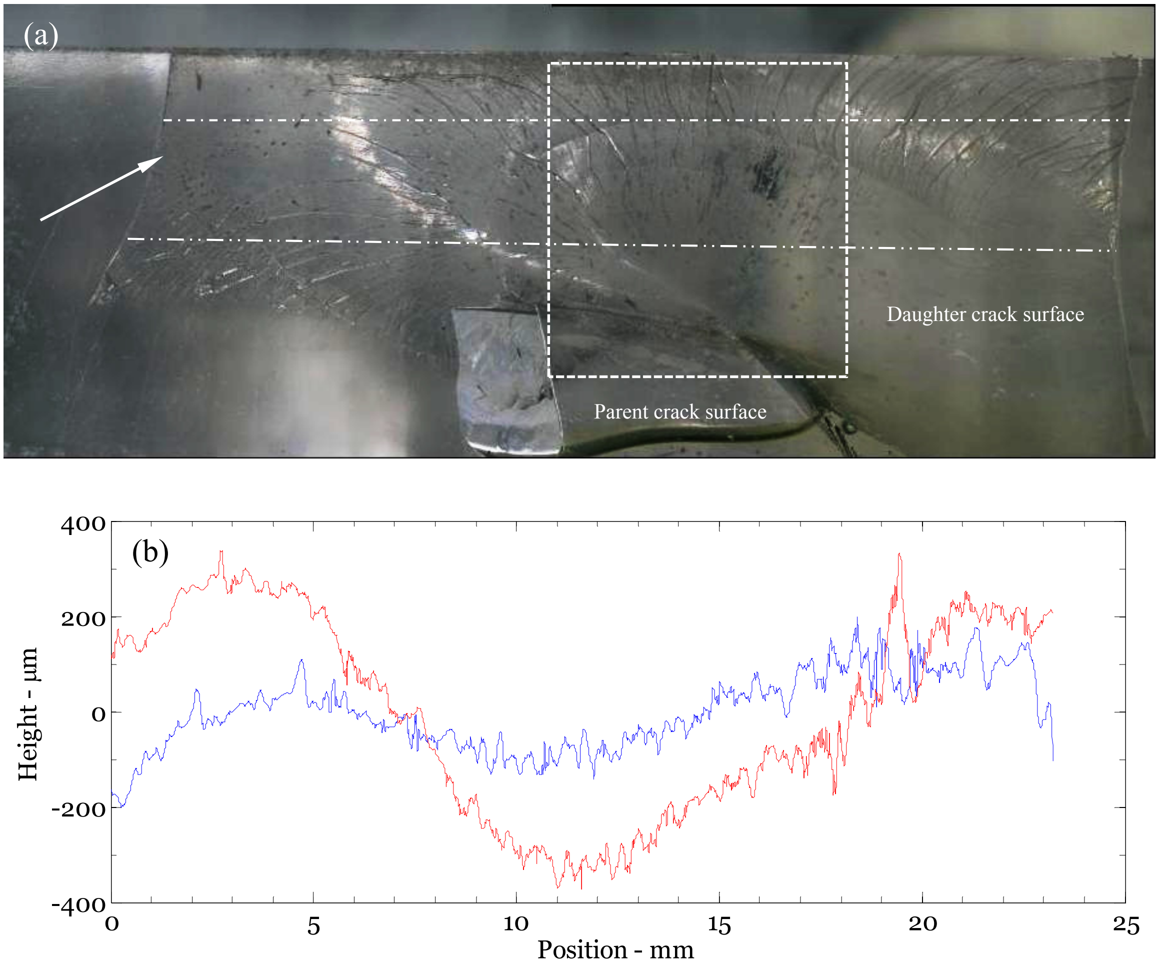

Figure 2.15. (a) Optical microscope image of daughter crack that has grown beyond the initiation to reach the far boundary of the specimen. The white dash-dotted and dash-double-dotted lines are ~23 mm long. (b) Height variation from the mean surface of the daughter crack along the white dashed and double-dashed lines of (a); note that the height variation is within $\pm 300\mu m$ over a span of about 23 mm.

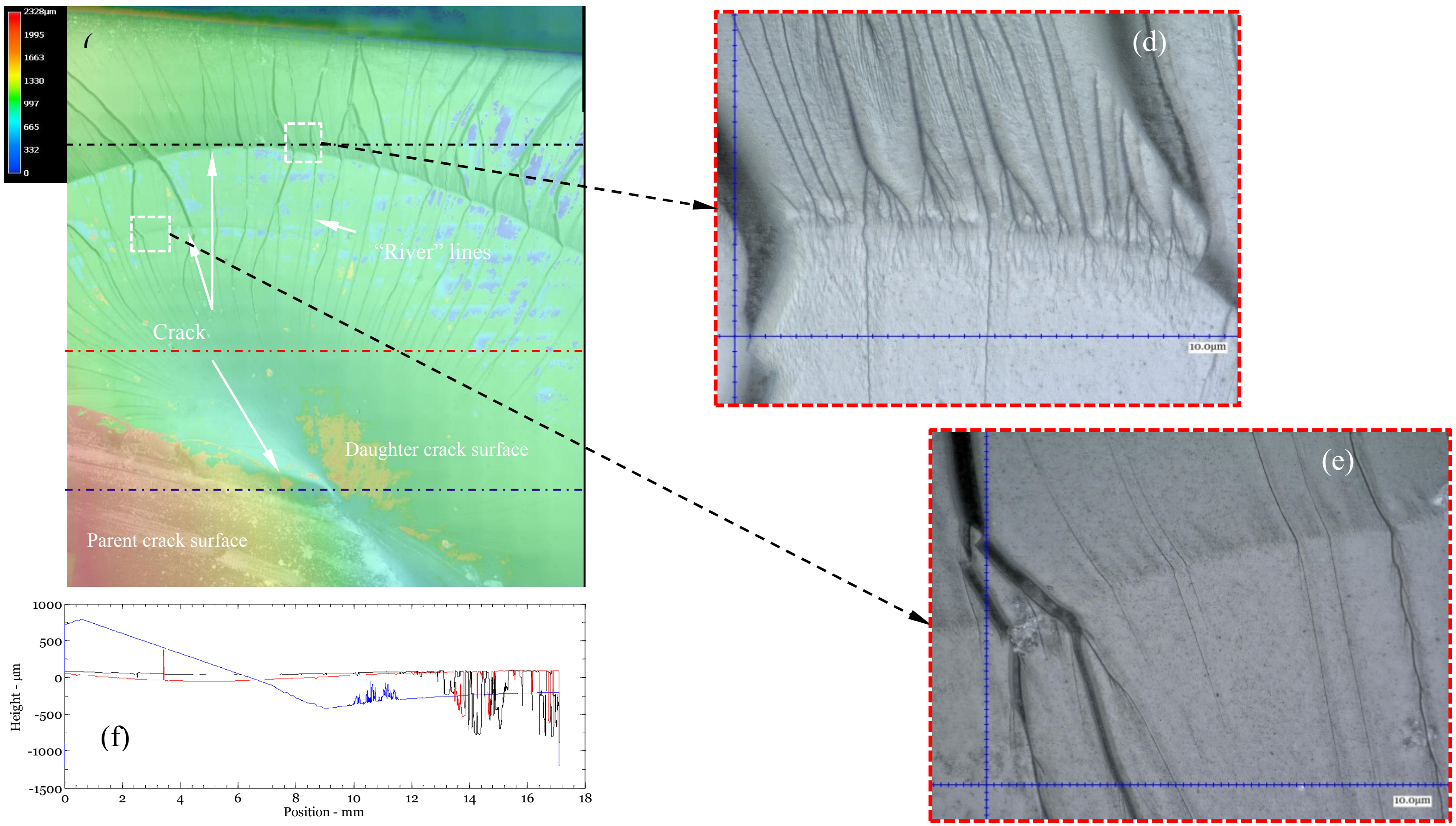

Figure 2.15. (continued). (c) High magnification topographic image of region marked by the white dashes square in (a). Arrest lines and river lines are identified in this figure. (d) and (e) High magnification views of the regions marked in (c) showing arrest and reinitiation. (f) Height variation along daughter crack surfaces along the blue, red and black lines marked in (c).

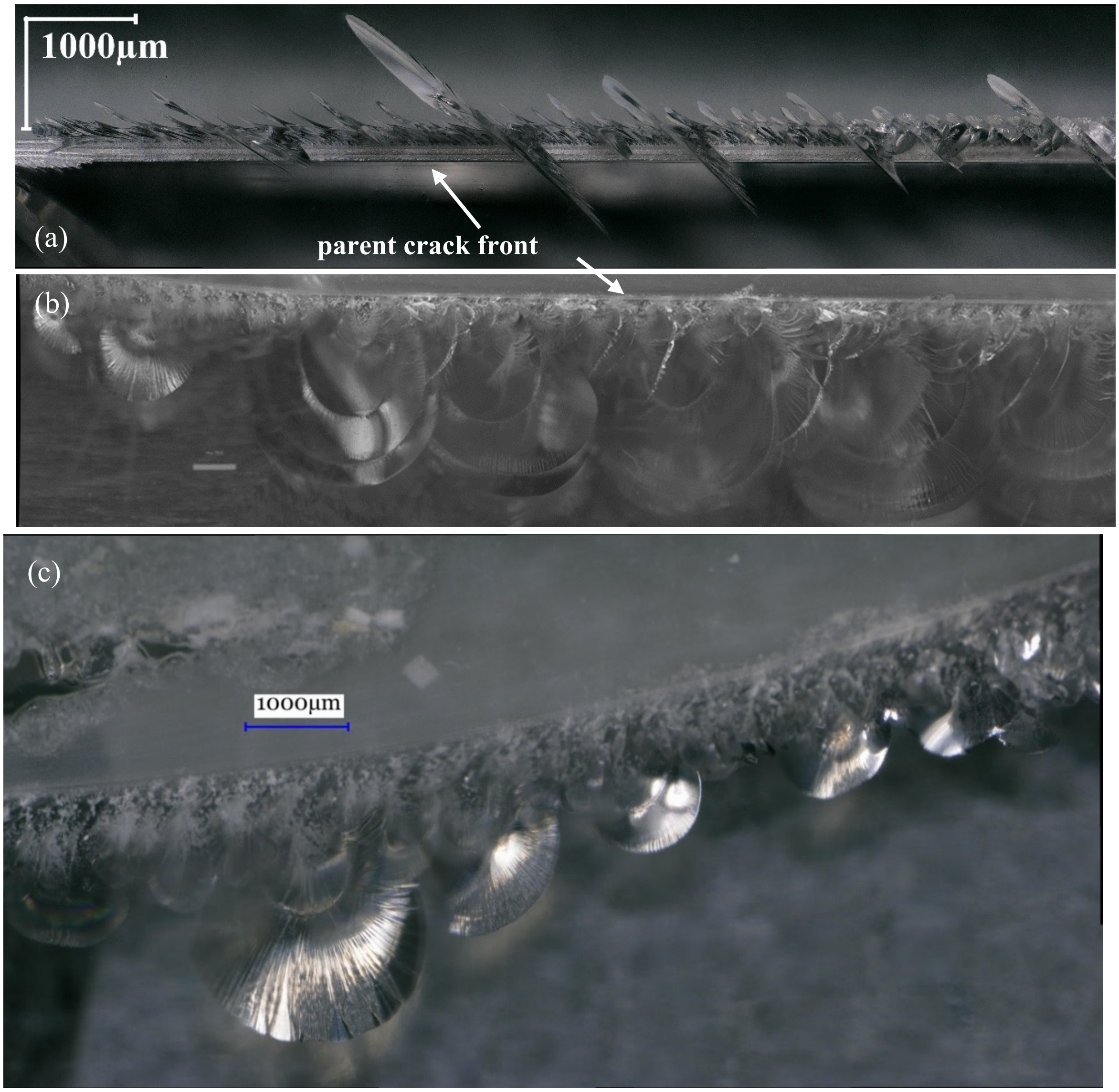

Figure 2.16. (a) Image of nucleated daughter cracks viewed in the –***b*** direction. This image shows very clearly that there are no type B cracks at this stage of growth of the type A cracks from the parent crack. (b) Image of the daughter cracks, viewed in the –***n*** direction. (c) Image of the daughter cracks in an oblique view, clearly illustrating multiple levels of daughter cracks, with different lengths and spacing.

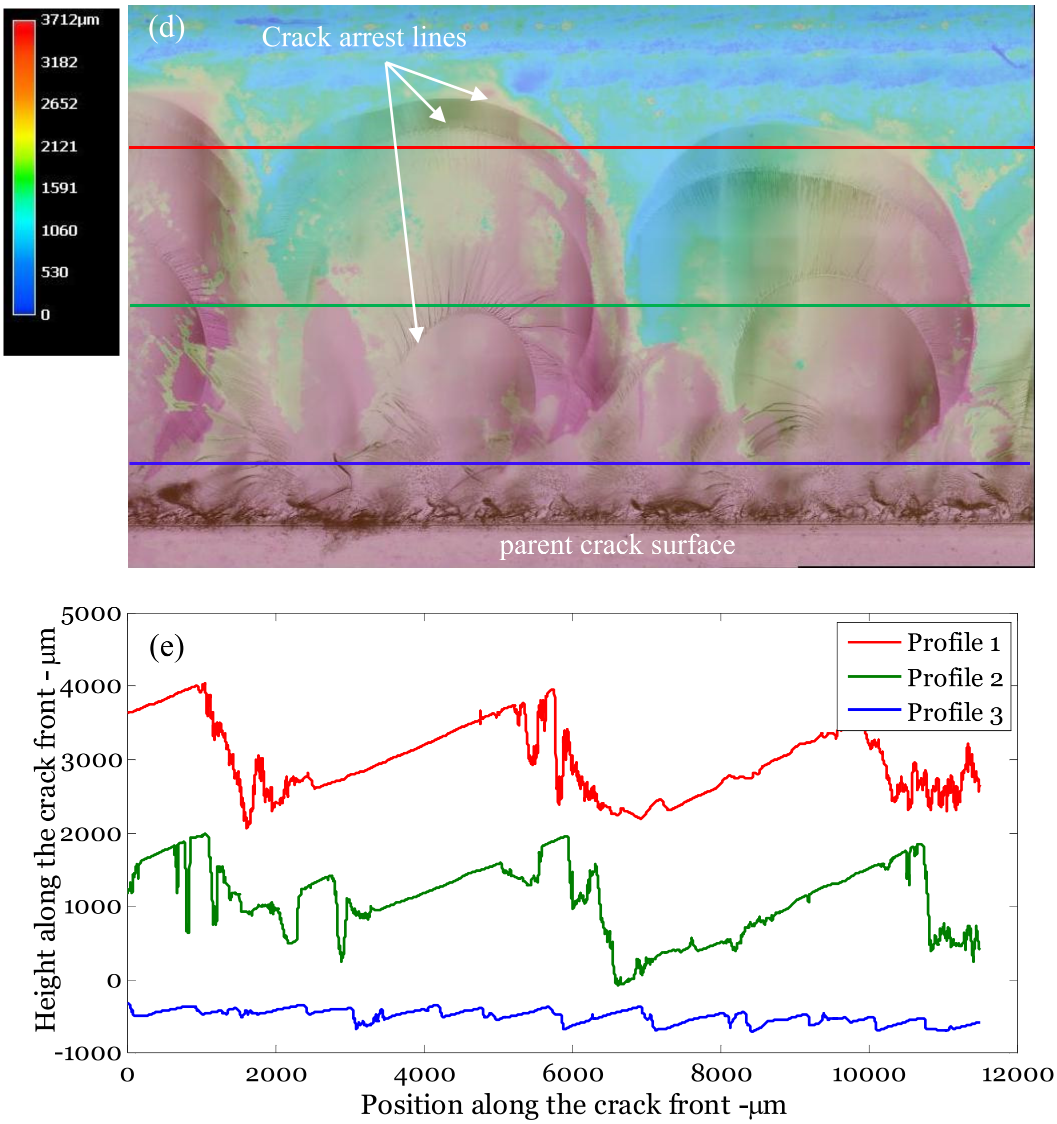

Figure 2.16. (continued). (d) Micrograph from the $-\boldsymbol{n}$ direction, with color coding indicating height above the mean initial crack plane. (e) Height variation along three lines selected in (d), indicating that the nucleated cracks are slanted at an angle of 26^o with respect to the initial crack plane. While a large number of fragments are nucleated from the many defects along the crack front, they are shielded by the faster fragments and only a few crack fronts survive as can be seen from the spacing. Note that the angle at which these daughter cracks grow does not change.

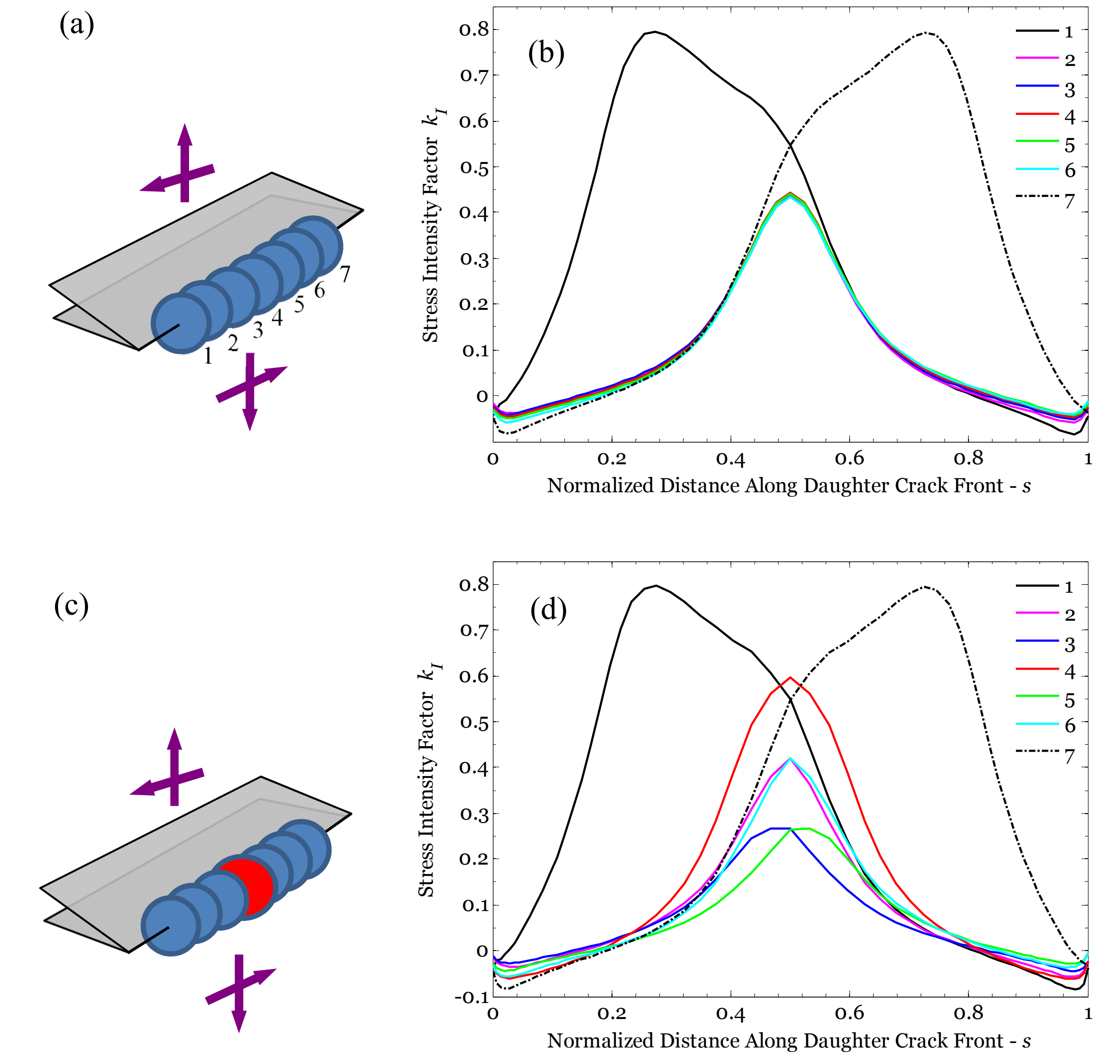

Figure 2.17. (a) The parent crack is perturbed by seven equal size daughter cracks. (b) The SIFs k_I along the daughter crack fronts for all seven cracks are shown; note that the interior cracks experience nearly the same SIFs. (c) The same geometry as in (a), except that the central daughter crack (crack #4) is increased in size by 10%. (d) The SIFs k_I along the daughter crack fronts for all seven cracks are shown; it is seen that the SIFs k_I for the perturbed crack increases, while the SIFs k_I for the immediate neighbor cracks (#3 and #5) drop significantly, and the farther cracks (#2 and #6) remain unchanged. This is the reason for the elastic shielding – any crack that gets to advance through fluctuations will inhibit the growth of its neighbor.

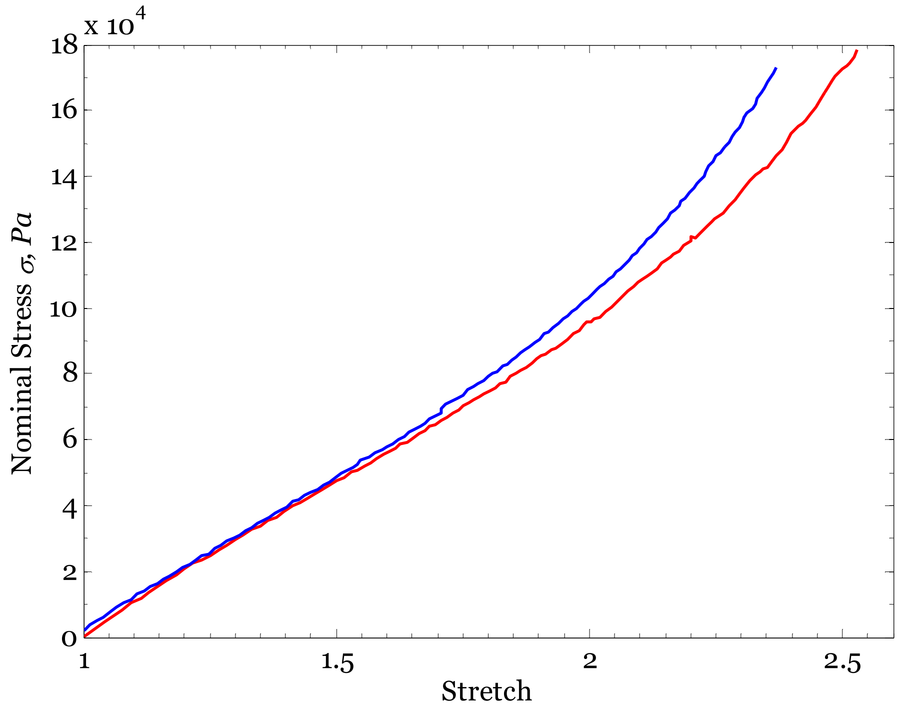

Figure 2.18. Nominal stress-stretch curve for two different gel strip specimens of the same dimensions under tension test. The material indicates an elastic behavior up to stretch of about 2 and stiffens up after this stretch level.

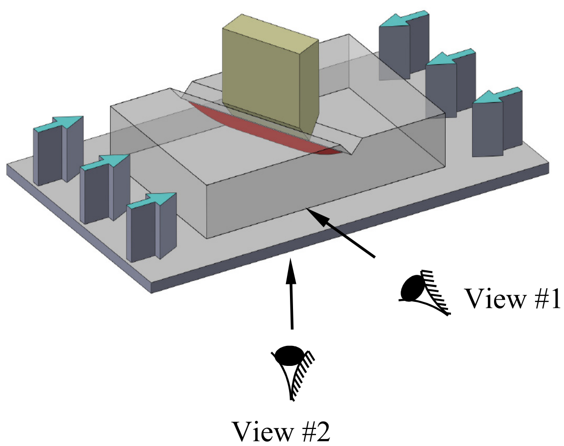

Figure 2.19. Schematic diagram of the mixed mode I + III experiment in hydrogel. Two video microscopic cameras were used to observe the crack surface and front from two perspectives.

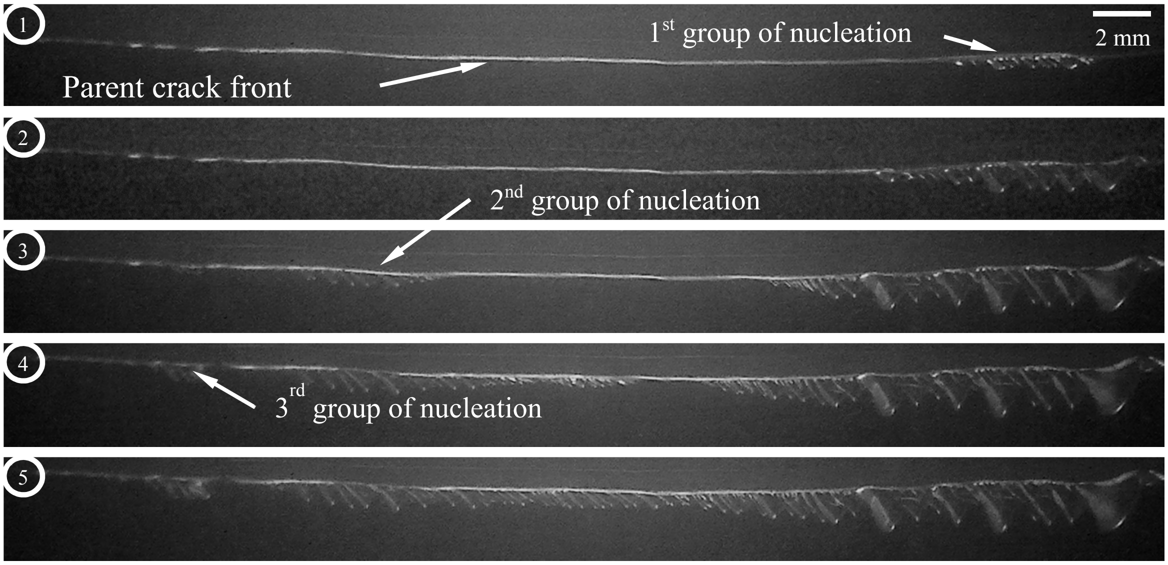

Figure 2.20a. Stochastic nucleation and shielding processes for the hydrogel specimen. The sequence of images (1 – 5) shows an oblique view (view #1) of the parent crack surface, providing a visualization of the parent crack front and the nucleation of daughter cracks.

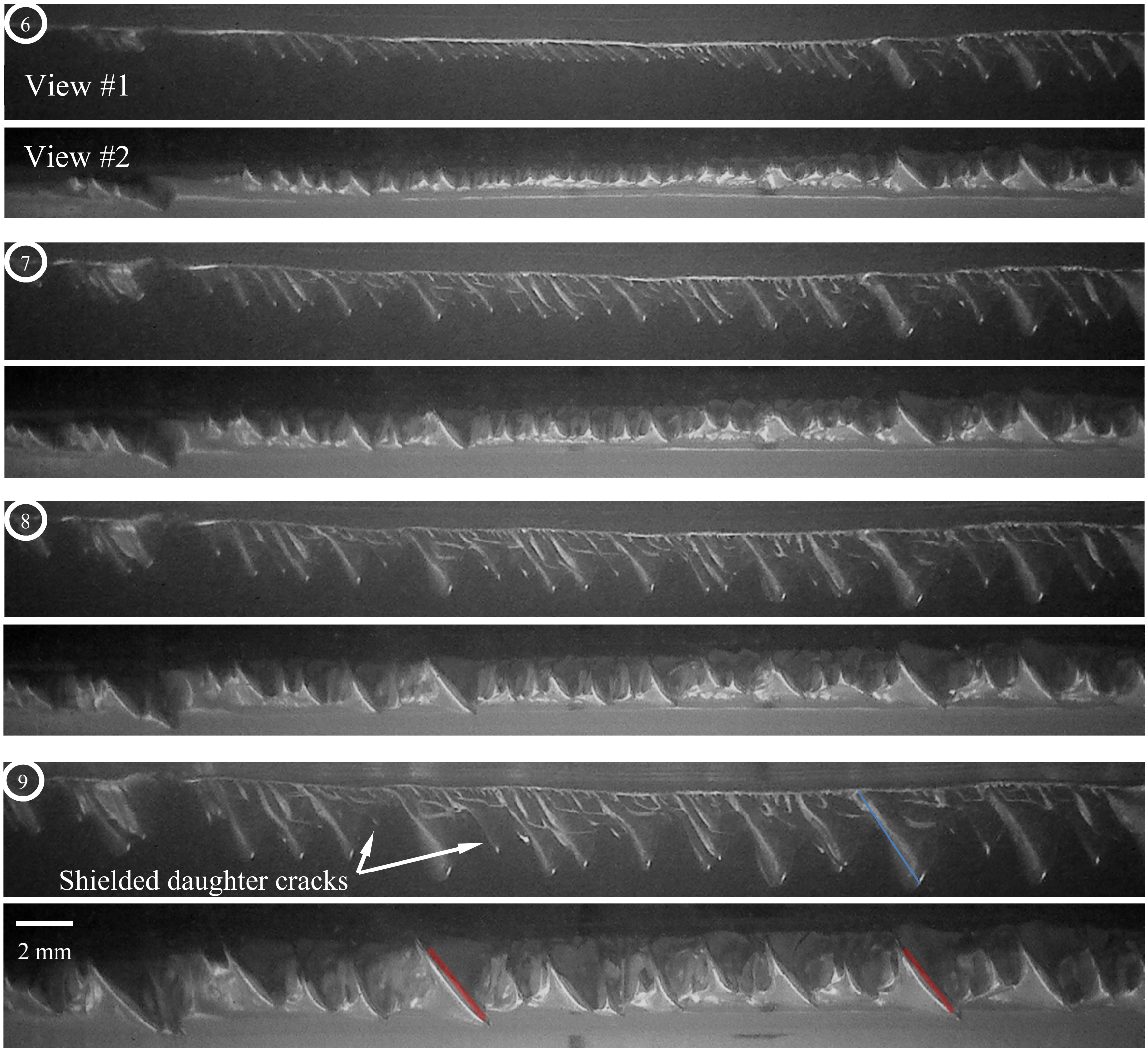

Figure 2.20b. This sequence of image pairs (6 – 9) shows an oblique view (view #1) of the parent crack surface, providing a visualization of the parent crack front and a view of the crack front (view #2) to visualize the type A daughter cracks, and their arrest by shielding. Two type A daughter cracks are identified by the two red lines placed parallel to two daughter cracks in image 9. Some shielded daughter cracks are indicated by the arrows in image 9.

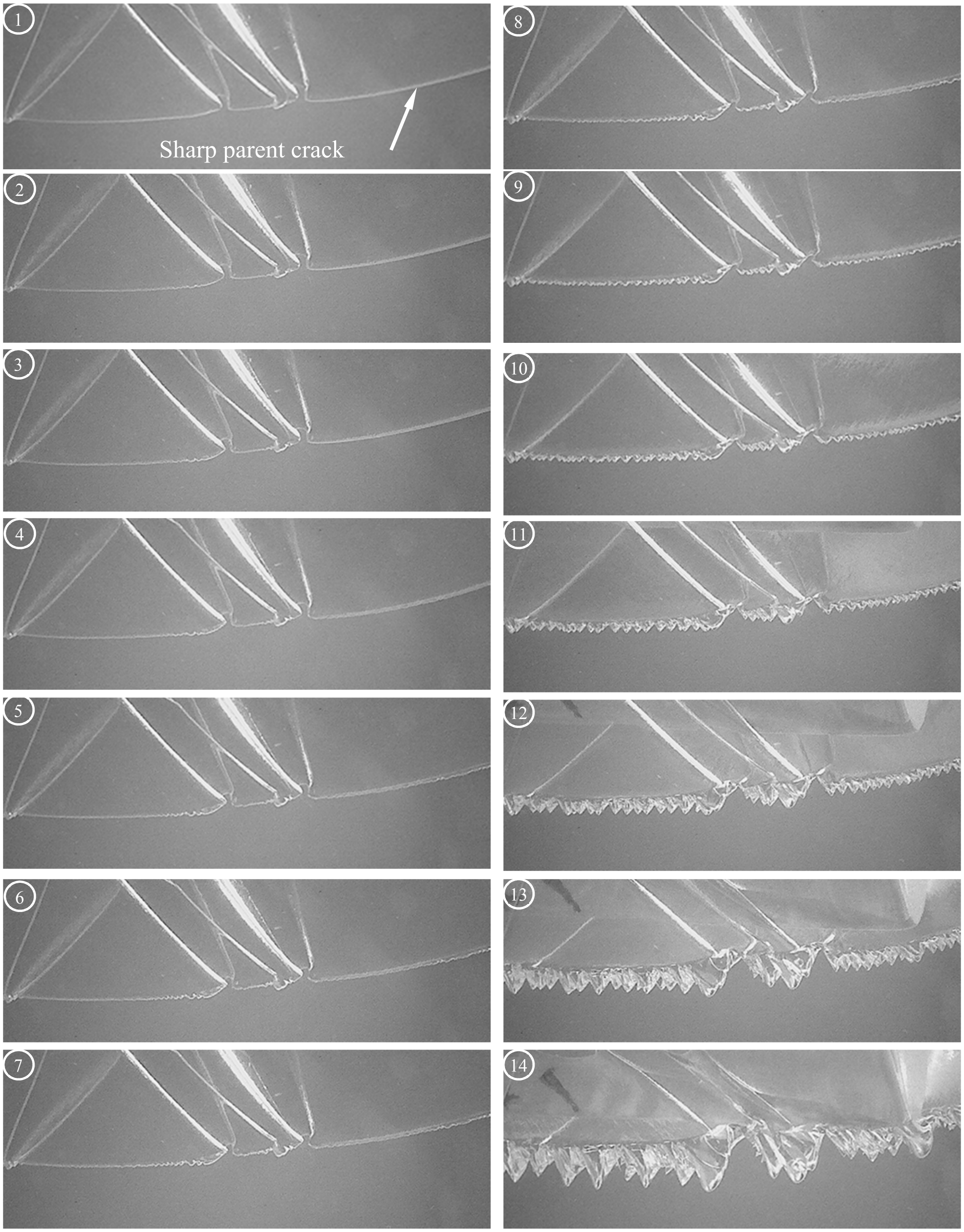

Figure 2.21. Nucleation of daughter cracks from a naturally grown, sharp parent crack front. View #1, showing a projection of the parent crack surface

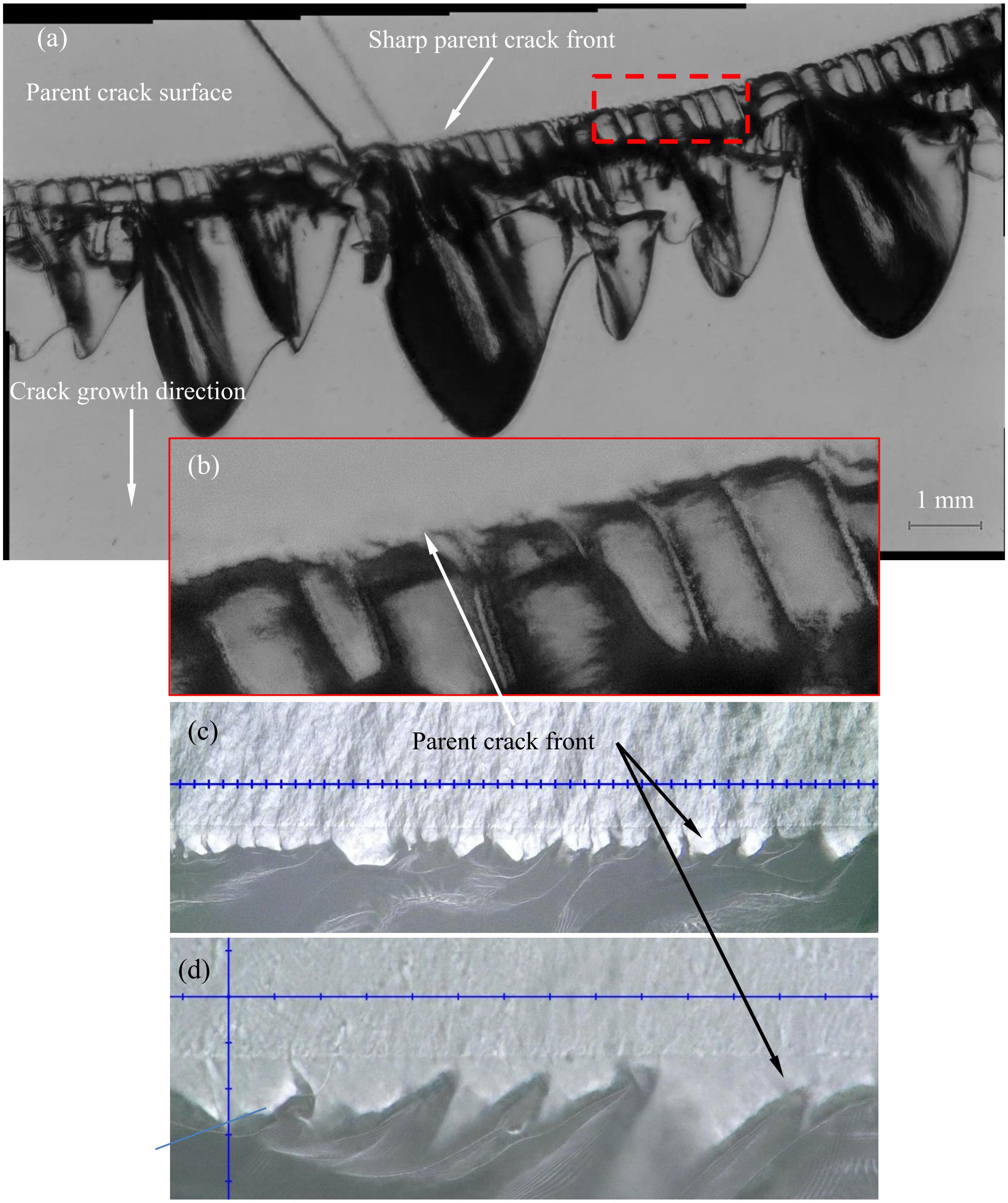

Figure 2.22. (a) Nucleation and growth of daughter cracks from a natural, sharp crack; (b) – (d) show progressively higher magnification images; the blue masks in (c) and (d) lines indicate a 20 μm scale bar.

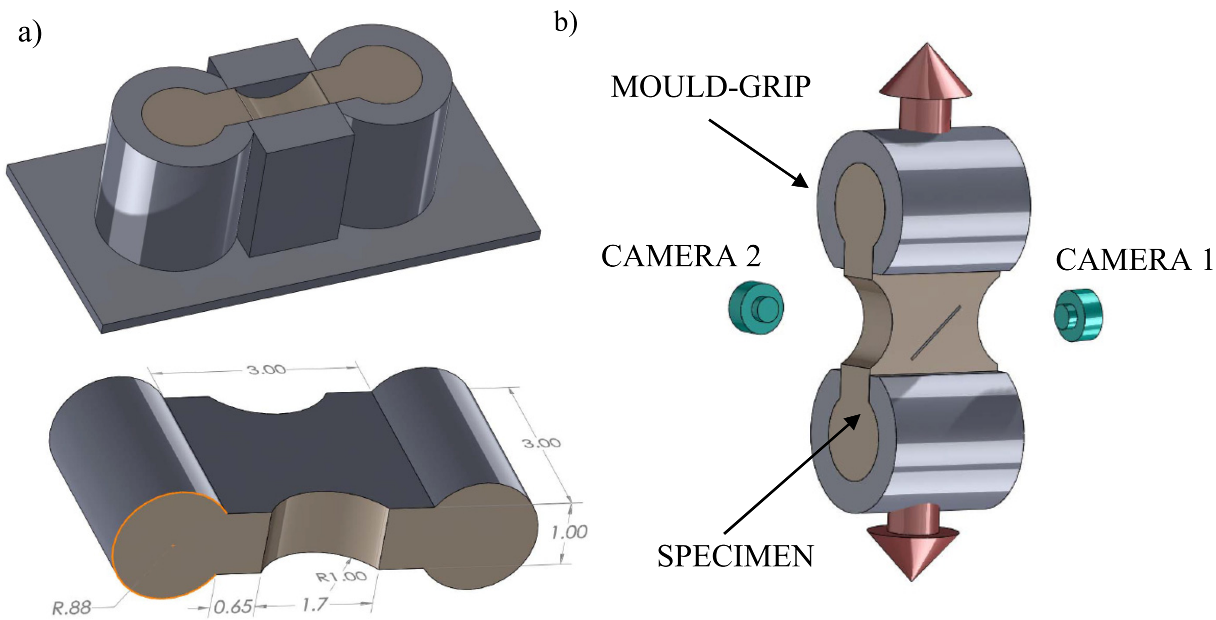

Figure 2.23. Setup for tension experiments on hydrogel. The mould and specimen dimensions are shown in (a). (b) Shows the loading feature and cameras arrangement.

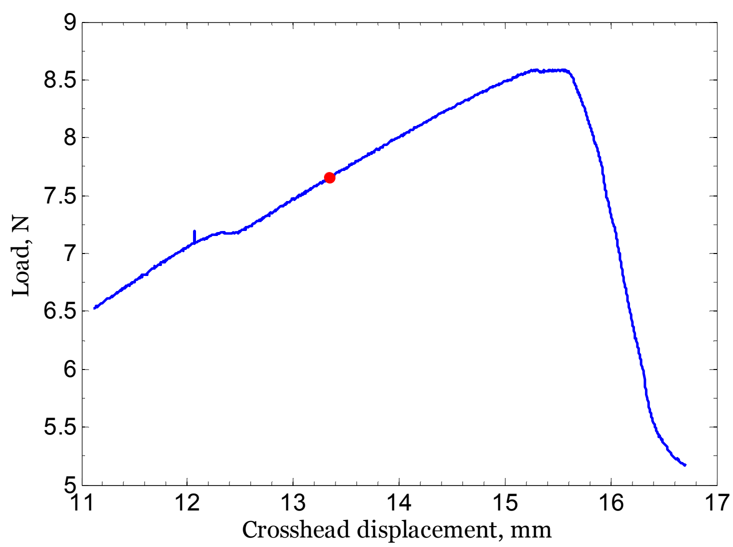

Figure 2.24. Load vs crosshead displacement. The crack started fragmenting at the load of 7.7 N

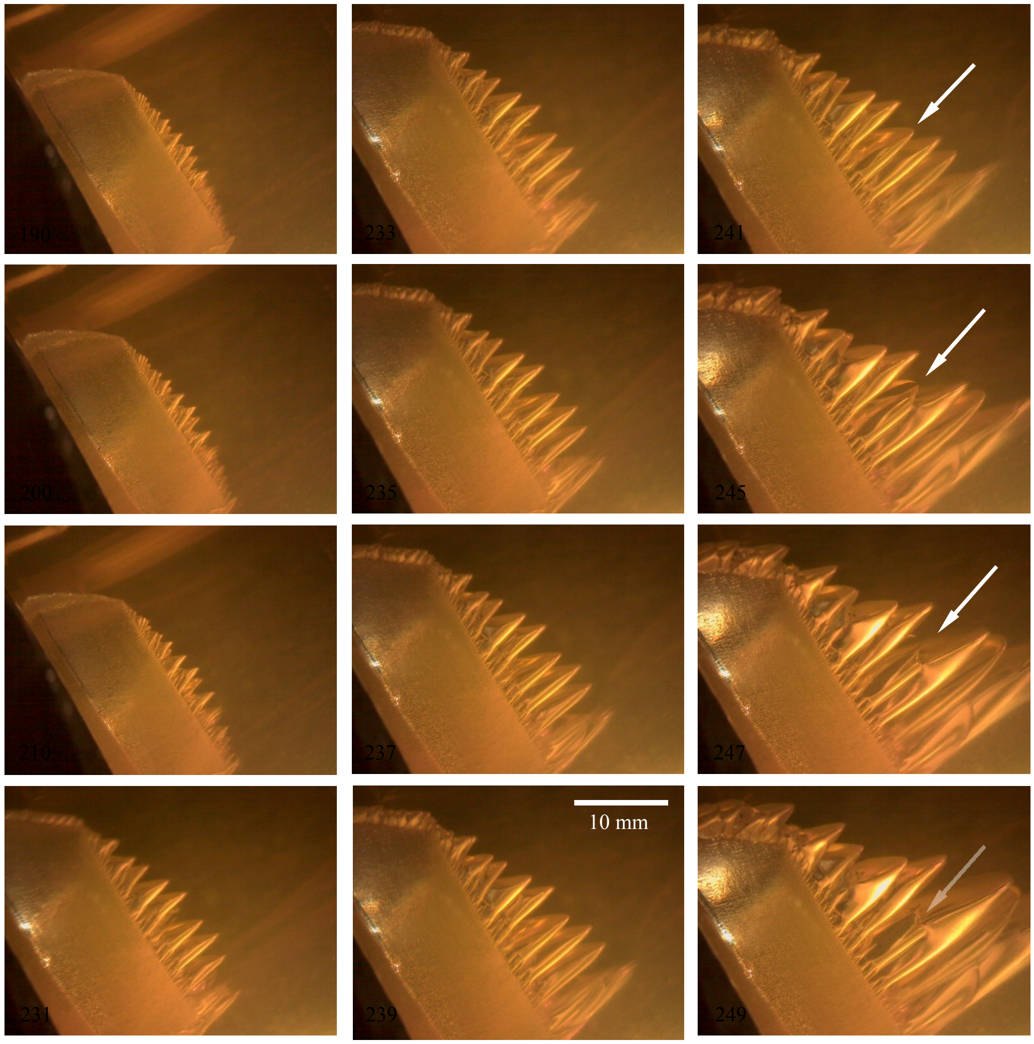

Figure 2.25. Nucleation of daughter cracks in the edge-cracked tension loading for gel. Oblique view (view #1). These images clearly show the absence of type B cracks and that all daughter crack grow straight in the same plane. The halting of coarsening is also observed as the parent crack begins to grow, by tracking individual daughter cracks as identified by the white arrows in images in the right column.

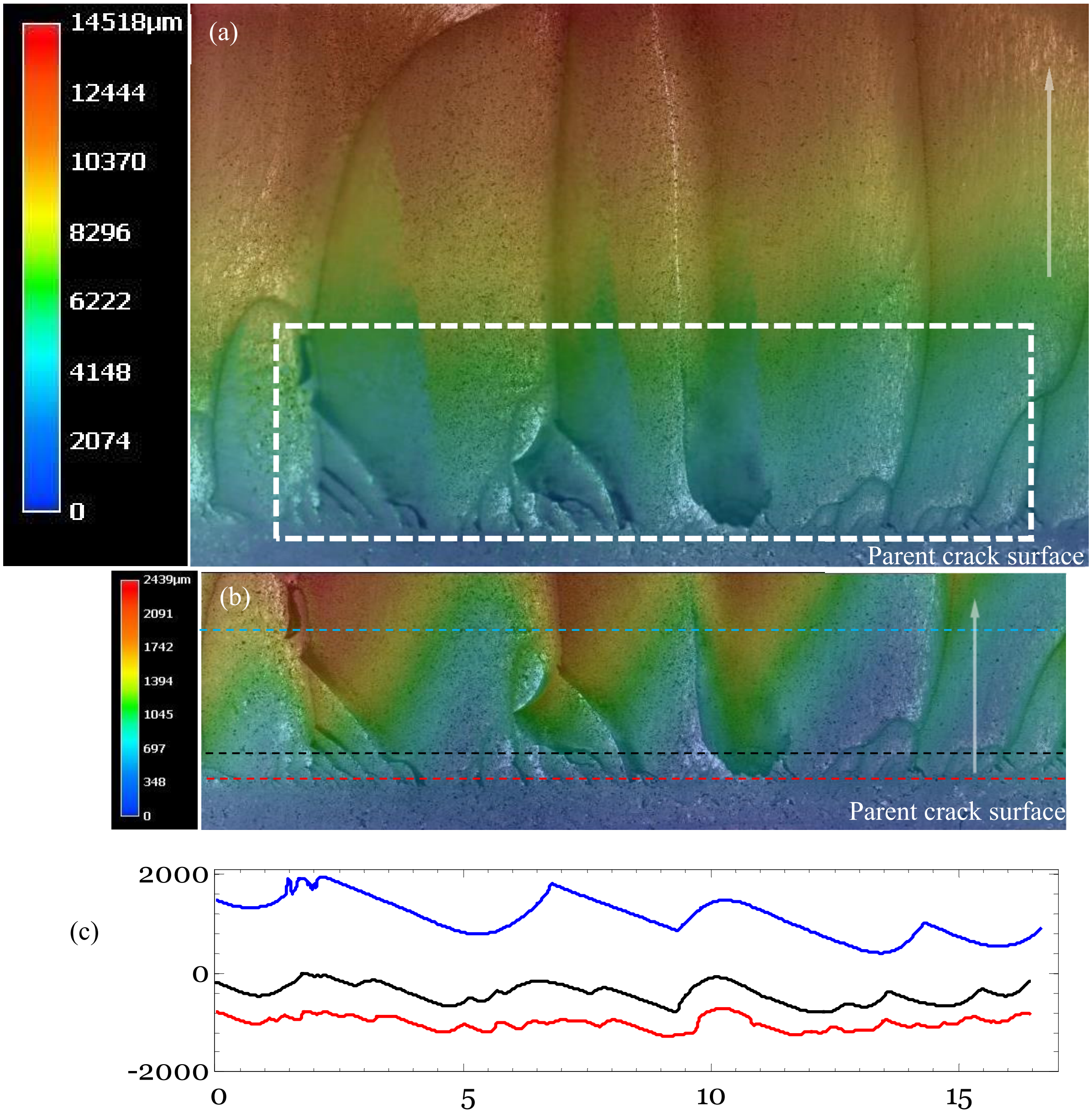

Figure 2.26. (a) Topographic map on the fracture surface of specimen with crack angle $\theta = 20^{\circ}$. The white arrow indicated direction of crack growth. (b) Higher magnification view of the dashed rectangular region in (a). The horizontal axis represents for the position in mm and provides a scale for the images; the vertical axis is the height in µm. (c) Profile of the crack surface along lines marked in (b). For better visibility, the profile at the black and red lines were shifted by (-1000,-1500).

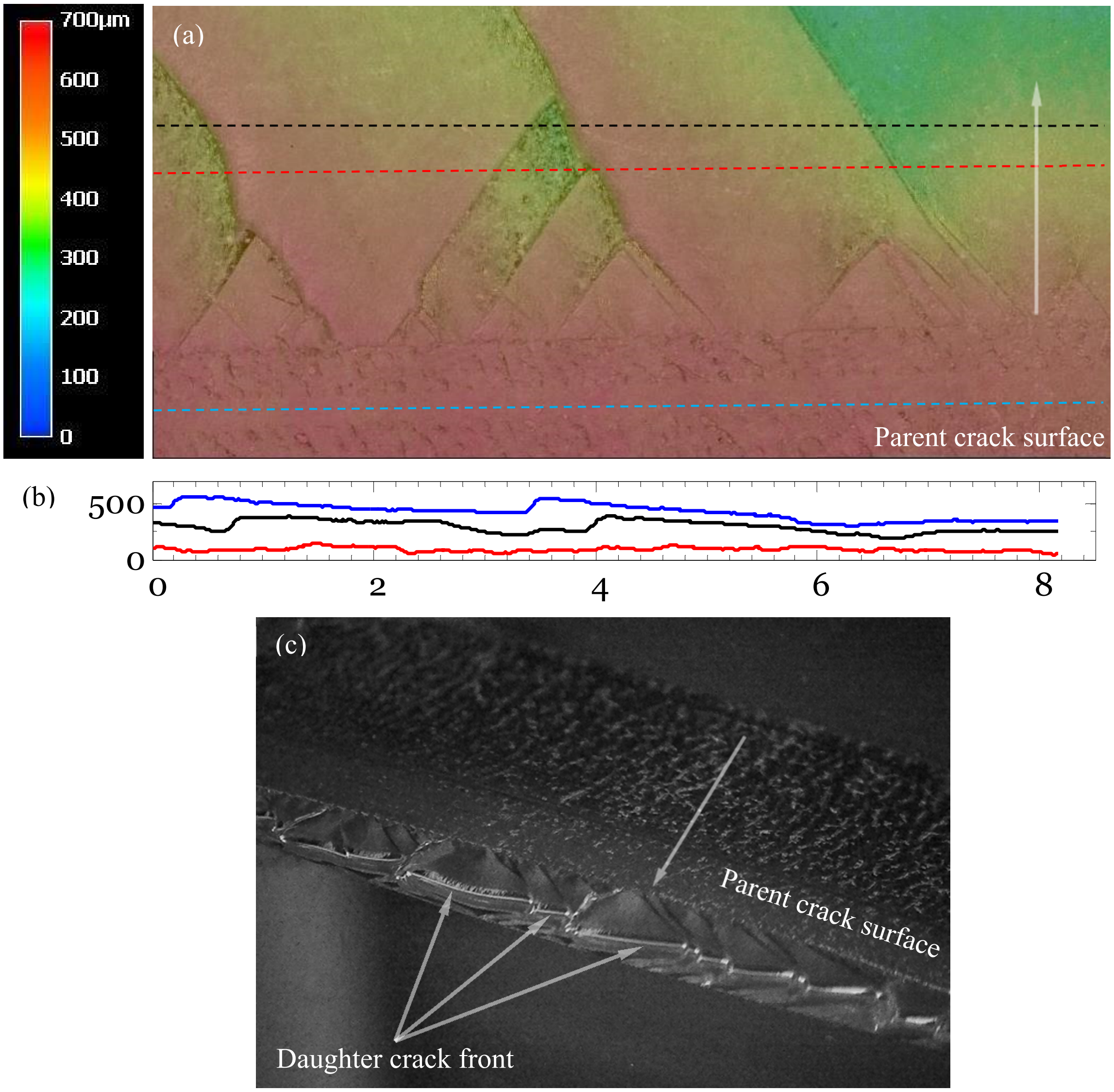

Figure 2.27 (a) Topographic map on the fracture surface of specimen with crack angle $\theta = 3^{\circ}$. The white arrow indicated direction of crack growth. (b) Profile of the crack surface along lines marked in (a). The horizontal axis represents for the position in mm and provides a scale for the images; the vertical axis is the height in µm. For better visibility, the profile at the black and red lines were shifted by (-200,-500). (c) Oblique view (view #1) of the crack front and surface.

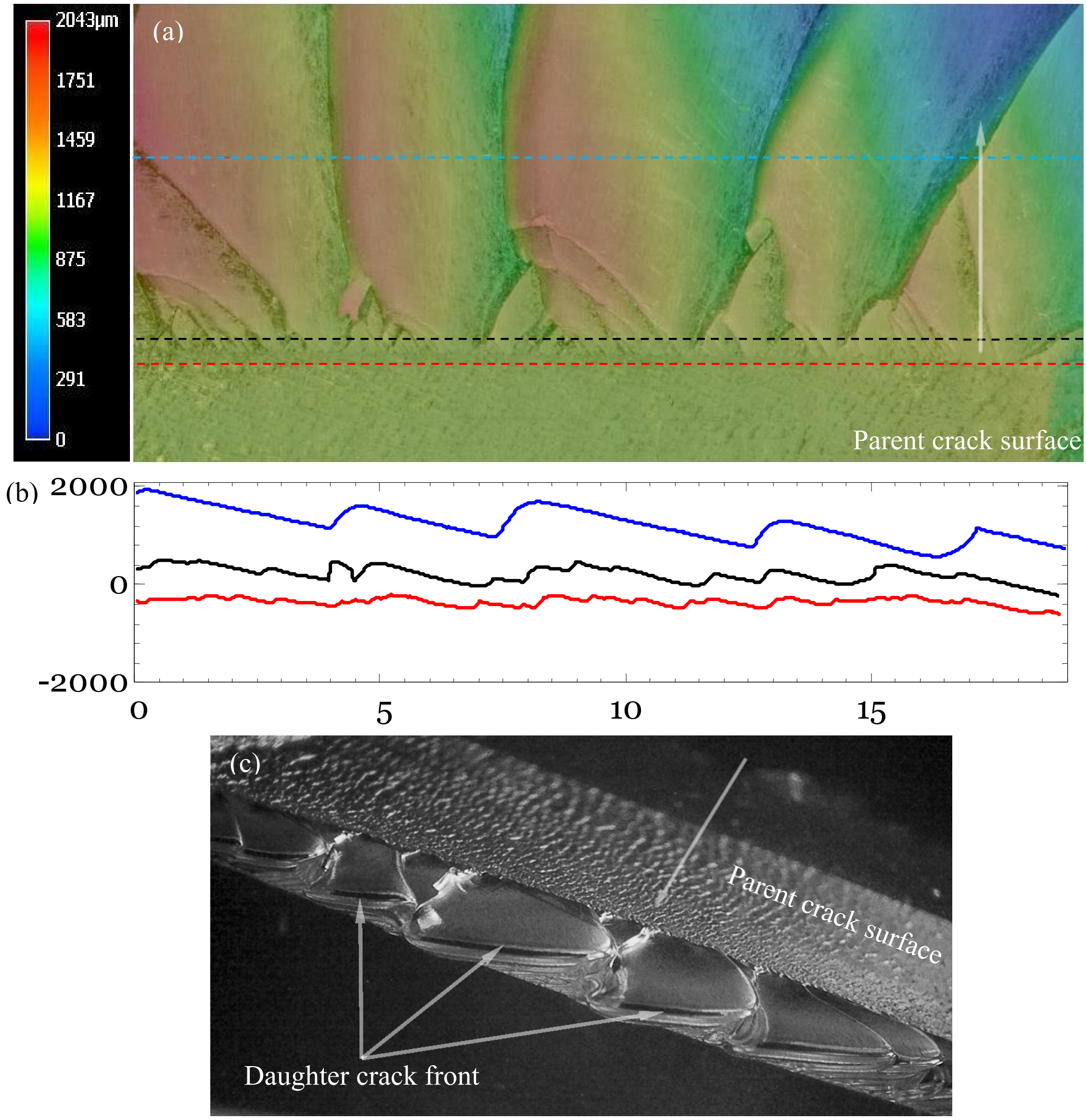

Figure 2.28. (a) Topographic map on the fracture surface of specimen with crack angle $\theta = 10^{\circ}$. The white arrow indicated direction of crack growth. (b) Profile of the crack surface along lines marked in (a). The horizontal axis represents for the position in mm and provides a scale for the images; the vertical axis is the height in µm. For better visibility, the profile at the black and red lines were shifted by (-1000,-1500) (c) Oblique view (view #1) of the crack front and surface.

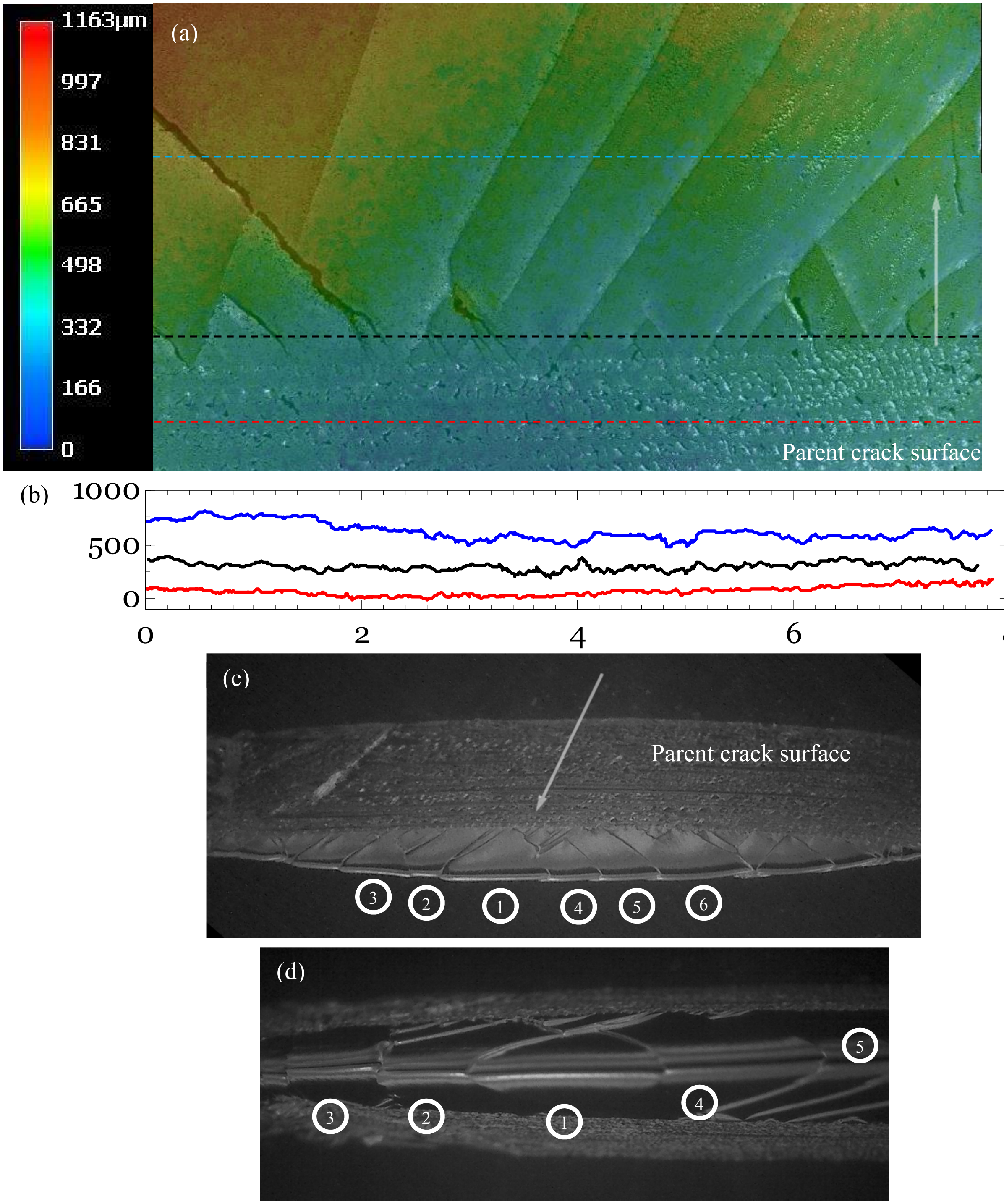
1163µm
997
831
665
498
332
166
0
(a)
Parent crack surface
(b)
1000
500
0
0
2
4
6
8
(c)
Parent crack surface
3
2
1
4
5
6
(d)
5
3
2
1
4

Figure 2.29. (a) Topographic map on the fracture surface of specimen with crack angle $\theta = 0^{\circ}$. The white arrow indicated direction of crack growth. (b) Profile of the crack surface along lines marked in (a). For better visibility, the profile at the black and red lines were shifted by (-100,-500). The horizontal axis represents for the position in mm and provides a scale for the images; the vertical axis is the height in μm. (c) and (d) Oblique views (view #1 and view #2, respectively) of the crack front and surface. The fragmented crack fronts are marked with labels 1 through 6 and identified in both views. Crack #1 leads all cracks; and hence it attempts to pull along cracks #2 and #4 on either side; this leads to cross-hatching marks on the fracture surface, with the left boundary moving further left and the right boundary to the right.

Chapter 3: Phase-Field Simulations

3.1 Formulation and Verification of the Phase-Field Model

3.1.1 A Review of the Phase-Field Model of Griffith Theory of Fracture

The phase-field method is a versatile technique for problems of moving interfaces such as the formation of microstructures in solidification, multiphase flow, image segmentation, etc. In recent years, it has been applied to fracture mechanics in order to provide a remedy for the discontinuity of the displacement field along the crack surface which poses difficulty for numerical solution techniques. There exist two kinds of phase-field formulations: the formulation based on Griffith's fracture theory (Bourdin et al, 2008) and the formulation based on Ginzburg-Landau theory (Karma et al, 2001). Ambati et al. (2015) provide a detailed comparative review of different formulations of phase-field models. The phase-field formulation based on Griffith's fracture theory will be reviewed briefly in this section to provide the context for the simulations in the following sections; our aim is to use the phase-field formulation to investigate the onset and growth of crack front fragmentation under mixed-mode I+III.

Consider a solid body enclosed in the domain Ω with the boundary $\partial\Omega$ and a crack Γ (shown in Figure 3.1). The domain boundary $\partial\Omega$ is divided into two non-overlapping subsets $\partial\Omega_h$,where the tractions are prescribed, and $\partial\Omega_g$, where the displacements are prescribed. According to the Griffith theory of fracture, the solution to a static crack growth problem is governed by the minimization of the energy functional:

$$E = \int_{\Omega} \psi_e d\Omega + \int_{\Gamma} G_c d\Gamma \tag{3.1}$$

where ψ_e and G_c are strain energy density and fracture energy, respectively. In the phase-field formulation, the fracture surface is approximated by a phase-field $c(\mathbf{x})$, $c \in [0,1]$, which represents the material state: $c = 0$ indicates that the material is fully damaged, while the material is intact for $c = 1$. Bourdin et al. (2008) and Miehe et al. (2010) used the following approximation for the energy associated with the fracture:

$$\int_{\Gamma} G_c d\Gamma = \int_{\Omega} G_c \left[\frac{(c-1)^2}{4l_0} + l_0 \frac{\partial c}{\partial x_i} \frac{\partial c}{\partial x_i} \right] d\Omega \tag{3.2}$$

where l_0 is an intrinsic length scale. The above phase-field approximation allows the surface integral term to be approximated through a volume integral and, the energy functional becomes:

$$\mathrm{E} = \int_{\Omega} \psi_e d\Omega + \int_{\Omega} G_c \left[\frac{(c-1)^2}{4l_0} + l_0 \frac{\partial c}{\partial x_i} \frac{\partial c}{\partial x_i} \right] d\Omega \tag{3.3}$$

The governing Euler-Lagrange equations are derived as:

$$\begin{cases} \dfrac{\partial \sigma_{ij}}{\partial x_j} = 0 \quad \text{in } \Omega \\ \dfrac{l_0}{2G_c} \dfrac{\partial \psi_\mathrm{e}}{\partial c} + \dfrac{c-1}{4} - l_0^2 \dfrac{\partial^2 c}{\partial x_j \partial x_j} = 0 \quad \text{in } \Omega \end{cases} \quad \text{where } \sigma_{ij} = \frac{\partial \psi_\mathrm{e}}{\partial \varepsilon_{ij}} \tag{3.4}$$

These equations are subjected to the boundary conditions:

$$\begin{cases} \boldsymbol{u} = \boldsymbol{g} \quad \text{on } \partial\Omega_g \\ \boldsymbol{\sigma}.\boldsymbol{n} = \boldsymbol{h} \quad \text{on } \partial\Omega_h \\ \nabla c.\boldsymbol{n} = 0 \quad \text{on } \partial\Omega \end{cases} \tag{3.5}$$

The material softening due to the presence of a crack is enforced by quadratic degradation function (Bourdin et al., 2008):

$$\psi_e := c^2 \psi_e \tag{3.6}$$

A significant limitation of this model (Bourdin's model) is that it allows a crack to grow under compressive loading condition. In order to suppress this nonphysical behavior, Amor et al. (2009) presented a model in which material softening based on the decomposition of the strain energy density into "positive" ψ_e^+ and "negative" ψ_e^- parts was considered corresponding to the dilatational and deviatoric parts of the strain tensor; Miehe et al. (2010) proposed an alternative model (Miehe's model) where the strain tensor is decomposed into positive and negative parts:

$$\begin{aligned} &\boldsymbol{\varepsilon} = \frac{1}{2}\left(\nabla \boldsymbol{u} + \nabla^T \boldsymbol{u}\right) = \boldsymbol{\varepsilon}_+ + \boldsymbol{\varepsilon}_- \\ &\boldsymbol{\varepsilon}_+ := \sum_{i=1}^{nsd} \langle \varepsilon_i \rangle_+ \boldsymbol{n}_i \otimes \boldsymbol{n}_i \ \ and \ \ \boldsymbol{\varepsilon}_- := \sum_{i=1}^{nsd} \langle \varepsilon_i \rangle_- \boldsymbol{n}_i \otimes \boldsymbol{n}_i \end{aligned} \tag{3.7}$$

where ε_i are the principal strains and $\boldsymbol{n}_i$ ($i = 1 - nsd$, nsd is the number of space dimensions) are the principal strain directions; the operators $\langle . \rangle_+, \langle . \rangle_-$ are defined as $\langle x \rangle_+ = \frac{1}{2}\left(x + |x|\right)$, $\langle x \rangle_- = \frac{1}{2}\left(x - |x|\right)$. Miehe et al. (2010) defined strain energies ψ_e^+, ψ_e^- computed from the positive and negative components, respectively, of the strain energy as follows:

$$\psi_e^+(\boldsymbol{\varepsilon}) = \frac{\lambda}{2}\left\langle tr(\boldsymbol{\varepsilon})\right\rangle_+^2 + \mu tr\left(\boldsymbol{\varepsilon}_+^2\right)$$
$$\psi_e^-(\boldsymbol{\varepsilon}) = \frac{\lambda}{2}\left\langle tr(\boldsymbol{\varepsilon})\right\rangle_-^2 + \mu tr\left(\boldsymbol{\varepsilon}_-^2\right) \tag{3.8}$$

In Miehe's model, the quadratic degradation function is applied only to the "positive" part of the strain energy density to prohibit the crack to evolve under compressive loading:

$$\psi_\mathrm{e} := c^2\psi_e^+ + \psi_e^- \tag{3.9}$$

In order to prevent the crack from healing, Miehe et al. (2010) enforced the irreversibility condition, through a strain-history field: $\mathcal{H}_0 = \mathcal{H}(\boldsymbol{x}, t_0) = 0$ at the initial step $t = t_0$, $\mathcal{H} = \mathcal{H}(\boldsymbol{x}, t_n)$ at the loading step $t = t_n$. Borden et al. (2012) also used the initial strain-history field $\mathcal{H}_0$ to model the initial crack. More recently, Wheeler et al. (2015) and Heister et al. (2015) used augmented Lagrangian and primal-dual active set strategies to impose the irreversibility condition. These strategies are computationally expensive, and we will follow the Miehe's strategy. The strain-history field for the Bourdin's model can be written as:

$$\mathcal{H}(\boldsymbol{x}, t_n) = \begin{cases} \psi_\mathrm{e}, \text{ for } \psi_\mathrm{e} > \mathcal{H}(\boldsymbol{x}, t_{n-1}) \\ \mathcal{H}(\boldsymbol{x}, t_{n-1}), \text{ otherwise} \end{cases} \tag{3.10}$$

And for the Miehe's model:

$$\mathcal{H}(\boldsymbol{x}, t_n) = \begin{cases} \psi_e^+, \text{ for } \psi_e^+ > \mathcal{H}(\boldsymbol{x}, t_{n-1}) \\ \mathcal{H}(\boldsymbol{x}, t_{n-1}), \text{ otherwise} \end{cases} \tag{3.11}$$

Substituting the strain-history field and material degradation model into the system of Eqs. (3.4) yields:

$$\begin{cases} \dfrac{\partial \sigma_{ij}}{\partial x_j} = 0 \quad in\,\Omega \\ Q(c) - l_0^2 \dfrac{\partial^2 c}{\partial x_j \partial x_j} = 0 \quad in\,\Omega \end{cases} \tag{3.12}$$

where $Q(c) = \left(\dfrac{l_0 \mathcal{H}}{G_c} + \dfrac{1}{4} \right) c - \dfrac{1}{4}$, $\sigma_{ij} = \begin{cases} c^2 \dfrac{\partial}{\partial \varepsilon_{ij}} (\psi_\mathrm{e}), \text{ for Bourdin's model} \\ c^2 \dfrac{\partial \psi_e^+}{\partial \varepsilon_{ij}} + \dfrac{\partial \psi_e^-}{\partial \varepsilon_{ij}}, \text{ for Miehe's model} \end{cases}$

The governing equations Eqs. (3.12) are coupled between the displacement field and phase-field which can be solved with a coupled formulation or operator splitting schemes. Heister et al. (2015) pointed out that the energy functional is non-convex simultaneously in both displacement field and phase-field which will influence the robustness of the coupled solution scheme. They proposed a linearization technique using a linear extrapolation and time-lagging for the phase-field variable in the equation for the displacement to obtain a convex energy functional. But, there is no proof for the theoretical validity of the proposed extrapolation; and if the load step is too coarse, this scheme may give a wrong solution. Miehe et al. (2010) using the staggered scheme to decouple these two equations. The solutions obtained by this scheme may not be the solutions to the equilibrium state since there is no iteration between the displacement field and phase-field solvers within each loading step. In the work of Wheeler et al. (2014), the solvers for the two fields were iterated as illustrated in Figure 3.2. The convergence measures they used are not based on physical measures. Ambati et al. (2015) discussed some other convergence measures based on the convergence of the energy functional which have more physical meaning.

Phase-field model offers an attractive tool for modeling the crack propagation. The choice of the intrinsic length scale l_0, and the validation for the phase field model needs to be done carefully. Most of the works on phase-field model have compared their results on mode I loading for single edge notch geometry or mode II loading for pure shear geometry. All of the comparisons were done qualitatively with the crack path geometry and no quantitative comparison was done with the experimental data. In this work we carefully designed the experiments to provide good data for the validation of the phase-field as well as other numerical methods for brittle fracture

3.1.2 Numerical Implementation of the Phase-Field Model

We developed a fully three-dimensional finite element code for the phase-field formulation discussed in Section 3.1.1. The following ingredients of the phase-field model were considered in our implementation: both Bourdin's and Miehe's models for material softening were implemented (the Miehe's model is assumed for all the simulation reported in the following sections, unless stated otherwise); the strain history field (Miehe et al., 2010) was used to enforce the irreversibility condition for phase-field parameter. This code was written on a parallel framework using Message Passing Interface library (MPI), Metis library (Karpis and Kumar, 1999) for mesh partition and Petsc (Balay et al. 2014) for nonlinear/linear solvers. The displacement field and phase-field equations are solved based on a staggered scheme with iteration within each load step. For the convergence measure of this iteration, we adopted the energy functional convergence measure as discussed in Ambati et al. (2015):

$$\alpha = \frac{E_{n-1} - E_n}{E_n} < tol \tag{3.13}$$

where E_n, E_{n-1} are the energy functional for the current and previous load steps. For the simulations reported in this section, the tolerance was set to $tol = 10^{-7}$; and it took about 500 iterations between the phase-field and displacement field equations to attain convergence. Post-processing was accomplished with ParaView and special MATLAB codes. All simulations were performed at the Texas Advanced Computing Center's Stampede Supercomputer; depending on problem size, 16 to 256 cores were used. Typical run times were on the order of 1 - 10 hours, depending on the problem size.

The elastic material properties, (E, ν), the modulus of elasticity and Poisson's ratio, respectively, are taken from experimental calibration data as appropriate. For the fracture energy, Bourdin et al. (2008) showed that the fracture energy is amplified in the simulation based on finite element discretization and that this has to be taken into account in formulating the simulation. Therefore, we scaled the fracture energy used in the simulation by the approximation proposed by Bourdin et al. (2008):

$$G_c^{sim} = \frac{G_c}{\left(1 + {h}/{4l_0}\right)} \tag{3.14}$$

where G_c is the actual material fracture energy, h is the minimum size of the mesh; this leaves the intrinsic scale in the phase-field model l_0 yet to be chosen. One option is to let this be unspecified and all lengths are then scaled by the value of l_0. Another option is to obtain an estimate of l_0 by considering the response of the phase-field model to homogenous uniaxial deformation (see Borden et al. 2012); this solution indicates that the stress attains a peak value of

$$\sigma_c = \frac{9}{16}\sqrt{\frac{EG_c}{6l_0}} \tag{3.15}$$

when the phase-field parameter reaches $c_c = 3/4$; corresponding to this, the strain level is $\varepsilon_c = \sqrt{G_c/(6l_0E)}$. Rearranging, one can obtain the following estimate

$$\sigma_c^2 l_0 = \frac{27EG_c}{512} \tag{3.16}$$

This implies that corresponding to any chosen value of l_0, there is an appropriate peak stress σ_c. Assuming that the peak stress is equivalent to the tensile strength of the material ($\sigma_c \sim 50$ MPa) yields $l_0 \sim 18\times10^{-6}$ m. Since this will result in a large number of degrees of freedom, particularly when we wish to simulate physical experiments with dimensions of many centimeters, we will take $l_0 \sim 100\times10^{-6}$, and compensate accordingly on σ_c. Therefore, E, ν, G_c, l_0 are the primary parameters used in the phase-field simulations. In the following, we will use normalized values in some simulations, and physical values when simulations are to be compared to specific experiments.

3.1.3 Verification by Comparison to Analytical Solutions

It is recognized that the phase-field model allows for damaging the elastic response of the material, and hence will develop a damage zone near the crack tip; this zone resembles a Dugdale-Barenblatt (DB) type cohesive zone in the vicinity of the crack tip. Therefore, it should be possible to develop a comparison between the analytical solution of the DB model and the phase field model for a crack in equilibrium. This is considered in Section A for a semi-infinite crack with a square-root singular field imposed at a distance R from the crack tip. This is followed in Section B by a comparison of the crack opening profile for a problem with a microcrack interacting with a macrocrack, a problem for which an exact two-dimensional elasticity solution was presented by Rubinstein (1985). Growth of cracks under mixed-mode loading is discussed in Section C.

A. Semi-Infinite Crack with a Dugdale-Barenblatt Cohesive Zone

Consider a semi-infinite crack in an infinite plate, loaded in the far-field to generate a stress field dictated by K_I^∞; let a Dugdale-Barenblatt type cohesive zone form near the crack tip. Considering a constant cohesive stress σ_c, we get an estimate of the size of the cohesive zone as

$$\alpha = \frac{\pi}{8}\left(\frac{K_I^\infty}{\sigma_c}\right)^2 = 7.5l_0 \tag{3.17}$$

where σ_c is the peak stress generated in the phase-field model. The phase-field simulation set-up is shown in Figure 3.3. The domain of simulation is a square of size $4000l_0 \times 4000l_0$; such a large domain is chosen in order to ensure that the displacement field associated with the asymptotic K-field of a crack whose tip is at the origin $(x=0, y=0)$ may be prescribed on the boundary of the domain:

$$\begin{Bmatrix} u_x(r,\theta) \\ u_y(r,\theta) \end{Bmatrix} = \frac{(1+\nu)K_I^\infty}{2E}\left(\frac{r}{2\pi}\right)^{\frac{1}{2}} \begin{bmatrix} (2\kappa-1)\cos\left(\dfrac{\theta}{2}\right) - \cos\left(\dfrac{3\theta}{2}\right) \\ (2\kappa+1)\sin\left(\dfrac{\theta}{2}\right) - \sin\left(\dfrac{3\theta}{2}\right) \end{bmatrix} \tag{3.18}$$

where $\kappa = 3-4\nu$ for plane strain. The computational mesh contains 50,000 hexahedral elements and it was generated in such a way that there is one line of elements with size $h = l_0/2$ along the x-axis from $x=-2000l_0$ to $x=10l_0$. Two solution strategies were used: "growth solution" and "healing solution". In the "growth solution" approach, the phase-field parameters of those elements which lie between $x=-2000l_0$ to $x=-1000l_0$ were prescribed to be zero. Then, we let this initial short crack to grow to its final length in the equilibrium state. In the "healing solution" approach, none of the nodes was prescribed in the phase-field solver, but we instead provided the initial guesses for the solutions to both phase-field and elasticity solvers. These initial solution guesses are associated with the displacement field and phase-field of the semi-infinite crack domain with the crack tip located at the origin. No irreversibility condition was imposed on the phase-field parameter in the "healing solution" approach. The two solution strategies provided the same crack opening profile after the staggered scheme was completed.

The equilibrium solution is obtained in the phase field simulations after about 500 iterations of the staggered scheme; the displacement in the y direction (the crack opening displacement or COD) of the upper and lower nodes of the central line elements were analyzed. Figure 3.4a shows the comparison of the phase-field solution (red line) with the analytical solution from the DB cohesive zone model (blue dashed line) and the linear elastic K-field solution (black line). The solution from phase-field model indicates a cohesive zone of the length $\alpha \sim 8l_0$. The COD profile from the phase-field solution is quite close to the DB solution. The discrepancy is most likely due to the fact that the DB model considers constant tractions along the cohesive zone, whereas the phase-field model will experience varying tractions. However, the phase-field model is expected to be a solution to the elastic problem – meaning that the solution should match the elastic field. How far away from the crack tip does the phase-field solution match the elastic solution? Clearly, at a distance of about $50l_0$, there is still a significant difference between the phase-field solution and linear elastic solution. Figure 3.4b shows the error in the COD as a function of the distance from the crack tip; from this we see that the elastic field is approached to within 0.1% as long as one is $500l_0$ away from the crack tip. Therefore, it appears that the disturbance in the stress field caused by introducing damage over a characteristic distance

l_0 perturbs the elastic field over $500l_0$. This is particularly important when interactions between cracks are to be considered, as illustrated in the next section.

B. Macrocrack Interaction with a Microcrack

The second problem of verification that we consider relates to the interaction between cracks. Rubinstein (1985) considered a problem of the interaction of a collinear periodic array of microcracks ahead of a semi-infinite macrocrack and determined the SIFs both at the macrocrack and microcrack tips. For the special case of a single microcrack ahead of a macrocrack (see geometry in Figure 3.5), the stress intensity factors are given below[10]:

$$
\begin{aligned}
K_I(0) &= K_I^{\infty}\sqrt{\frac{b}{a}}\,\frac{E\left(1-a/b\right)}{K\left(1-a/b\right)} \\
K_I(a) &= K_I^{\infty}\left(\frac{b}{a}\,\frac{E\left(1-a/b\right)}{K\left(1-a/b\right)}-1\right)\left(b/a-1\right)^{-1/2} \\
K_I(b) &= K_I^{\infty}\left(1-\frac{E\left(1-a/b\right)}{K\left(1-a/b\right)}\right)\left(1-a/b\right)^{-1/2}
\end{aligned}
\tag{3.19}
$$

where $K_I(0)$, $K_I(a)$ and $K_I(b)$ are the stress intensity factors at the macrocrack tip, left microcrack tip and right microcrack tip, respectively, and K_I^{∞} is the stress intensity factor applied far-field from the macro-, micro- crack system. In addition, the displacement along the line $y=0$ were also calculated:

[10] There was a minor typographical error in the formula for $K_I(a)$ in Rubinstein (1985)

$$u_y\left(y=0\right)=\frac{\kappa+1}{2\mu}\frac{K_I^\infty}{2\sqrt{2\pi}}\operatorname{Im}\left[\int\frac{c-z}{\sqrt{z(a-z)(b-z)}}dz\right] \tag{3.20}$$

where $z=x+iy$ and μ is the shear modulus. Other elements of the stress field could also be determined with some additional effort, but this is not needed for the purposes of the comparison sought here. These SIFs at all crack tips are plotted in Figure 3.6, normalized by the applied K_I^∞. It is clear that the microcrack amplifies the SIF of the macrocrack. This amplification increases as the distance between the microcrack and macrocrack decreases. For example, the SIF at the macrocrack is enhanced 20% when the ratio $a/\left(b-a\right)=0.2$. This means if one applies the far-field displacement associated with SIF which is 20% less than the material critical SIF on the boundary, the SIF at the macrocrack tip will reach K_{IC}; and the macrocrack will grow with any further increase of the far-field displacement. We explore this problem using the phase-field simulation. The problem set-up is shown in Figure 3.5. Next, we look into the different lengths associated with the problem in order to determine the appropriate discretization. Let l_0 represent the intrinsic size scale for the gradient damage model in the phase-field simulation. Then, from the results in Section 3.1.3A concerning the semi-infinite crack problem, $\alpha\sim 10l_0$ represents the cohesive zone size scale and sets the intrinsic scale for the fracture problem. From the geometry of the crack interaction problem, a, the separation distance between the macro and micro crack tips, sets the smallest geometric length scale and this should be large in comparison to α, in order to recover the appropriate elastic solution. Based on the discussion in Section3.1.3A, we choose $a\sim 50\alpha\sim 500l_0$. Next, in order to enhance the SIF at the main crack tip by about 20%, we must select $a/\left(b-a\right)\sim 0.2$ (based on Rubinstein, 1985); this implies $b=6a=300\alpha=3000l_0$. The macro-crack K-field boundary condition must be applied at a distance R from the crack tip; this must be far enough that the displacement field corresponding to the K-field may be applied (and the applied K_I^∞ must be at least 20% below K_{IC}). We shall require $R >> b$; it is not clear how large R should be in order to have the displacement field at the boundary correspond to the K-field of the overall K_I^∞, centered at the macrocrack tip. We shall assume $R \sim 10b = 30000 l_0$ would be sufficient; any error associated with this could be removed by applying the exact displacements to the outer boundary from the analytical solution supplied in Rubinstein (1985) since the far-field displacements will be mildly enhanced by the existence of the micro-crack. It is easy to see that even for simple problems, the discretization would yield large numbers of degrees of freedom. This problem will get exacerbated if the distance between the cracks decreases further: decreasing a will demand a commensurate reduction in l_0.

The microcrack is modeled by prescribing zero phase-field parameter for all the nodes located within the microcrack line as discussed in Section 3.1.3A. Similarly, all the nodes located within the macrocrack line are provided with zero initial guesses (the "healing" solution approach was used in these simulations). The mesh contains 150,000 hexahedral elements. The displacements on the far boundary are prescribed with fixed values associated with $K_I^\infty = K_{IC} / \gamma$, centered at the macrocrack tip. With this loading setup, we determine where the crack will end up. For the case of $\gamma = 1.2$ the macrocrack ends up at location $x \sim 20 l_0$ which is about 3 times larger than the cohesive zone size. If we increase the far-field displacement by setting $\gamma = 1.19$, the macrocrack exhibits a cohesive zone of length in the order of $8 l_0$. This means the phase-field solution only gives the SIF amplification of the macrocrack 1% less than the closed-form solution of Rubinstein (1985). Figures 3.7 and 3.8 show a comparison of the phase-field solution for the crack opening displacement along the crack line associated with $\gamma = 1.19$ and $\gamma = 1.20$, respectively, against the close form solution of Rubinstein (1985). At distances from the crack tip that are greater than $500 l_0$, the differences in the COD are less than 2%, indicating that the phase-field can provide acceptable solutions that are close to exact analytical solutions based on linear elasticity.

C. Crack Growth under Mixed-mode I + II

In the two problems considered in Sections3.1.3A and 3.3.3B, the cracks were stationary at the Griffith threshold. We now turn to verification of the code for crack growth under continued loading. Four problems are considered, one each for pure mode I and pure mode II and two for mixed modes I + II; in each case, a parallepipedic region similar to the one shown in Figure 3.3 is considered, with full three-dimensional discretization and K-field boundary conditions are imposed. A view of the discretization used near the crack tip is shown in Figure 3.9a; as in the previous examples, we set $h = l_0 / 2$ in the region near the crack tip. The outer boundary at which the K-field displacements corresponding to modes I and II displacements were applied was set at $R = 1000 l_0$; as discussed earlier, this is adequate to recover the elastic solution at large distances from the local perturbations near the crack tip arising from the damage model. The mode I simulation was performed in a number of steps; Step 0 corresponds to applying a displacement field corresponding to $K_I^\infty = K_{IC}$ and arriving at a converged solution from the staggered iteration scheme analogous to that in Section 3.1.3A. For continued mode I loading, with increasing far-field K_I^∞ the phase-field model "grows" the opening mode crack straight ahead. We note that the phase-field solution obtained in Step 0 can be taken to correspond to a "natural" crack and used in further simulations of different modes of loading. Therefore for mode II and mixed-mode simulations, the phase-field solution from Step 0 of the mode I simulation is taken as the initial value for the phase-field; mode II or mixed mode loading is applied by prescribing the elastic K-field at the outer boundary; in Steps 1 through N, the far-field $\left(K_I^\infty, K_{II}^\infty\right)$ was increased in small steps to grow the kinked opening mode crack. Note that no criterion for determination of the crack path is explicitly imposed in the phase field formulation, and that the crack must seek the direction along which the system attains a minimum potential energy. Figures 3.9b through 3.9e show the observed crack path under different mixed-mode loading conditions.

What is the expected response under mixed-mode I+II loading? There are different criteria that have been used in the last half-century. The three most commonly used criteria – the maximum tangential (or hoop) stress criterion (MTS), the principle of local symmetry (PLS) and the maximum energy release rate criterion (ERR) – are compared with the phase field simulations. These three criteria are summarized briefly. The MTS criterion (Erdogan and Sih, 1963) postulates that a mixed-mode I + II crack would extend in the direction γ_c along which $\partial\sigma_{\theta\theta} / \partial\theta = 0$. This yields

$$\gamma_c = 2\tan^{-1}\left[\frac{1-\sqrt{1+8\left(K_{II}^c / K_I^c\right)^2}}{4K_{II}^c / K_I^c}\right], \text{ when } \cos^3\frac{\gamma_c}{2}\left[1-\frac{3K_{II}^c}{K_I^c}\tan\frac{\gamma_c}{2}\right] = K_{IC} \tag{3.21}$$

The evaluation of the other two criteria is quite difficult in general; both the PLS (Goldstein and Salganik, 1974) and the ERR require the calculation of the stress intensity factor along kinked cracks; this has been calculated by Leblond (1999) using first order perturbation calculations: for a crack kinked at an angle γ, the stress intensity factors at the kinked crack tip in terms of the applied stress intensity factors are given as

$$\begin{aligned} k_I(\gamma) &= F_{I,I}(\gamma)K_I + F_{I,II}(\gamma)K_{II} \\ k_{II}(\gamma) &= F_{II,I}(\gamma)K_I + F_{II,II}(\gamma)K_{II} \end{aligned} \tag{3.22}$$

The functions $F_{I,I}(\gamma), F_{I,II}(\gamma), F_{II,I}(\gamma), F_{II,I}(\gamma)$ are given in Leblond (1999). The PLS criterion asserts that the crack will grow in the direction in which the local mode II stress intensity factor is zero, establishing a locally opening mode crack:

$$k_I(\gamma_c) = K_{IC},\ k_{II}(\gamma_c) = 0 \tag{3.23}$$

The maximum ERR criterion is the natural extension of Griffith's criterion that requires that the crack extend in the direction that minimizes the potential energy of the system (or maximizes the strain energy release rate for a material with constant fracture energy). Writing the energy release rate in terms of the stress intensity factors at the kinked crack, a mixed-mode I + II crack would extend in the direction γ_c along which

$$\frac{\partial G}{\partial \theta} = \frac{\partial}{\partial \theta}\left[k_I^2(\theta) + k_{II}^2(\theta)\right]\Big|_{\theta=\gamma_c} = 0, \text{ and } \frac{1-\nu^2}{E}\left[k_I^2(\gamma_c) + k_{II}^2(\gamma_c)\right] = G_c \tag{3.24}$$

The variation of the crack kink angle with mode mix and the critical combination of the mode I and mode II stress intensity factors at failure are shown in Figures 3.10 and 3.11 respectively for all three models. The critical conditions at which the phase field simulations indicate extension of the mixed-mode crack are also marked in these figures. Crack initiation is identified using a very simple criterion: since l_0 sets the scale of the fracture, crack initiation is taken to occur when $c < c_c$ is attained at an element at a distance $2l_0$ from the initial crack tip; the critical conditions at initiation and the corresponding crack kinking angle are also shown in Figures 3.10 and 3.11. Clearly, there is a very good agreement.

3.2 VALIDATION BY COMPARISON TO EXPERIMENTS FOR MIXED-MODE I + II

Experimental validation of the phase-field model is explored using the compact tension geometry and its modification. The experiments on mode I and mixed mode I+II are preformed to provide data for quantitative comparison with simulations of the global response of the specimen as well as the exact evolution of the crack tip with loading.

3.2.1 Specimen Geometry, Material Properties and Experimental Procedure

All the specimens were machined from the same sheet of polymethylmethacrylate (PMMA). The elastic modulus and Poisson's ratio were determined directly from a tensile test; this test was performed on a "dog-bone" type specimen in an Instron Model 5582 universal testing machine, at a nominal strain rate of 10^{-5} s^{-1}. In addition to monitoring the global load with a load cell, the method of digital image correlation (DIC) was used to monitor the development of major and minor strains as a function of the global deformation, while still within the linear elastic regime; the specimen was not tested to failure. The resulting data was processed to determine the modulus of elasticity and the Poisson's ratio: $E = 2.98$ GPa and $\nu = 0.35$; this specimen used for calibration was extracted from a specimen on which a fracture test had been performed previously, ensuring that these values are appropriate for the same material.

The fracture energy was determined using a standard compact tension specimen geometry shown in Figure 3.12a. The specimens tested have the dimensions $W = 50.8$ mm and $t = 3.0$ mm. Special attention was devoted to making a very sharp natural crack in front of the machined V-notch. A sharp, thin razor blade was mounted on an aluminum rod that was guided to move only in the vertical direction. The razor blade was then brought to contact with the tip of the V-notch; the aluminum rod was impacted with a hammer in order to wedge the razor blade into the V-notch and generate a natural crack. This technique produces a natural sharp crack ahead of the razor blade; this process produces a more reliable sharp crack in polymers than a fatigue cracking process. Still, the crack front exhibits some curvature, and the crack surface exhibits roughness that were then characterized quantitatively after the crack growth test. The experimental setup used for the fracture toughness test is shown in Figure 3.12b. The experiments were performed under the displacement control in an Instron Model 5582 testing machine at a cross-head rate of 4×10^{-4} mm/s. The load vs load-point displacement was monitored. In addition, the DIC technique was used to determine accurately the crack opening displacement COD at the load line, and to track the position of the crack front. Two cameras facing the specimen plane were used to capture the images of the areas used for calculating COD and tracking crack front location. These images were analyzed using the ARAMIS^{TM} software. The crack front location at each time step was identified based on the highly localized strain values in the vicinity of the crack tip. The COD was also computed from the result of image analysis. Then time correlation between image time sequence and loading time sequence was used to find the COD for each load step.

3.2.2 Experimental Results – Mode I

Two sets of experiments were performed under mode I loading conditions: in the first set of experiments (specimens CT_21, CT_22 and CT_24), the cracks were allowed to grow until they almost broke though the free surface, while in the second set of experiments (specimens CT_31, CT_32 and CT_33), they were allowed to grow only a short distance from the initial location. The plots of the load and crack length vs. COD for test CT_24 is shown in Figure 3.13; a micrograph of the fracture surface is also shown to the right of the plots, scaled appropriately. The load-COD response is linear almost up to the point of the peak load while the crack remains stationary. Measurable crack extension begins as the COD reaches a value of 0.163 mm; under the steady motion of the cross-head, the crack continues to grow, and the load begins to drop as the specimen compliance increases. At several points along the crack path, the crack stopped growing for brief periods, while both the COD and the load increased until the crack restarted its growth. Corresponding to each one of these arrest-reinitiation events, a residual mark was left on the fracture surface at the locations identified in Figure 3.13 by the arrows. A higher magnification image of the region near the initial crack front for specimen CT_24 is shown in Figure 3.14. It should be noted that the crack front is curved along the thickness direction and further that the fracture surface is quite rough on one side and grows with a smoother surface on the other side. The upshot of these observations is that the response observed will exhibit some scatter. Similar observations/measurements were obtained from the two sets of experiments indicated above; the collection of these results will provide the basis for identifying the "nominal" behavior of this material. The load vs COD variation and the crack length vs COD variation from the collection of these experiments are shown in Figure 3.15. The initial compliances are different for each specimen since the specimens have different initial crack lengths a. There was also some scatter of the critical load at which crack initiation occurred. For example, even though two pairs of specimens CT_21 and CT_31, CT_22 and CT_24 had approximately the same initial crack, their critical loads differ from each other by about 20%; this can be attributed to differences in the initial crack bluntness, curvature of the crack front in the thickness direction, and other "qualities" of the crack tip that influence the fracture process as pointed out for specimen CT_24. These results point out that one should not rely on the critical load for an accurate calibration of the fracture toughness. On the other hand as the crack grows further, the surface appears to be more uniform, and establishes self-similar crack growth from the perspective of the fracture process; the load vs. COD curves for most of the specimens seem to converge in this range, with only minor fluctuations.

Taking the above observations into account, the fracture toughness of the tested specimens was calibrated by fitting the part of the load-COD from the experimental data that corresponds to self-similar growth. Both the handbook solution (Murakami et al. 1987) and a J-integral calculation from the commercial software ABAQUS were used to determine the stress intensity factor as a function of crack length; the fracture toughness was then estimated to be $K_{IC} = 0.98$ MPa.m$^{1/2}$. The load-COD curve determined based on this value of fracture toughness is shown in Figure 3.15 as a thick black line; it can be seen to pass through the scattered data quite well; rigorous statistical measures have not been used in estimating the fracture toughness, although this poses no difficulties in principle. The corresponding fracture energy was calculated to be $\Gamma = \left(1-\nu^2\right)K_{IC}^2 / E = 0.285$ kJ/m^2. The values of the fracture toughness and fracture energy are within the range commonly reported for this material.

3.2.3 Experimental Results – Mixed-mode I+II Loading

Mixed-mode I+II loading was produced in the same CT specimen geometry used in the "mode I loading" by introducing a circular hole ahead of the crack line as indicated in Figure 3.16. First, a sharp crack was created by impacting a thin razor blade as in "mode I loading" case. Next, these specimens were loaded to grow the short initial mode I natural cracks. Then, an end mill was used to drill a circular hole at the desired location ahead of the crack path. The mixed-mode I+II state was varied by changing the location of the circular hole relative to the crack. The initial crack lengths of the specimens used in these experiments are in the order of $a \sim 12-14$ mm (these specimens were marked as CT_31 CT_32 and CT_33; and they were also used for mode I calibration experiments in the previous section). The load-COD curves for the initial mode I stage of the loading are shown in Figure 3.17b, identified as Step 1, while the load-COD responses of the same specimens after the hole was introduced and reloaded again in mixed modes I + II are identified as Step 2. The crack paths are shown in Figures 3.17a. Due to the effect of the hole, the cracks started growing at a lower load level compared to their earlier state in the specimens without the hole; due to the asymmetry introduced by the hole, the crack path deviates from the line of symmetry and approaches the hole by gradually turning towards the hole. The specimens CT_31 and CT_32 show similar load-COD responses and crack paths. Linear elastic solution of this problem could be approached through finite element or boundary element techniques, but this is not pursued; instead, we will use these as experimental results for validation of the phase-field simulations.

3.2.4 Comparison between Experimental and Phase-Field Simulation Results

The mode I and mixed-mode I+II validation problems considered in Sections 3.2.2 and 3.2.3 are 2D problems. The effect of the free surface on the crack front shape is small. Thus we adopted a plane strain calculation strategy for these problems. To this end, we generated the computational meshes with only one element through the thickness direction and applied periodic boundary conditions in this direction. The displacement boundary conditions were applied at two points in the pin-hole: the vertical and horizontal nodal displacement components were prescribed.

A. Comparison between Simulations and Experiments for Mode I Loading

The FE computational mesh was created based on the geometry of specimen CT_24 (see Figure 3.18) with the initial crack length measured from the fracture surface. This mesh contains approximately 52000 hexahedral elements with only one element in the thickness direction with periodic boundary conditions imposed in this direction. The region that contains the expected path of the growth crack was meshed with very small element size of $h = l_0/4$, where $l_0 = 100\mu m$; both structured and unstructured mesh geometries were used in order to evaluate potential mesh effects on the crack path. The initial natural crack which was generated by the razor blade impact in the experiment is modeled by prescribing the phase-field nodal value to zero for nodes on the central line element within the initial crack length. The simulation was performed by incrementing the displacements at the nodes corresponding to the loading pins in the experiment (identified as points A and B in Figure 3.18). This simulation was run on 80 processors; and it took about 2 hours to complete (each staggered iteration took about 500 iterations to converge). The simulation results and comparison with experimental data for specimen CT_24 are shown in Figure 3.19, where the load-COD variation as well as the crack length vs COD variation are shown. The crack "tip" in the phase-field simulation was identified as the farthest location from the notch, along the initial crack line at which the phase field parameter reached its critical value c_c. The load-COD curve from the simulation matches the experimental result very well, elastic with an initial response of a stationary crack up to a COD of about 0.16 mm and then followed by a drop of the load as the crack begins to grow. Crack growth followed the line of symmetry for this mode I loading condition; the load-COD curves from both simulation and experiment agree well with each other during this stage. Considering the fact that repeated experiments on nominally the same geometry resulted in crack initiation at different critical levels, (mainly as a result of possible bluntness and other irregularities of the crack tip) both load-COD and crack length-COD plots from simulation result fall inside the experimental data variation area. This indicates that the chosen length for the phase-field model – $l_0 = 100\mu m$ is appropriate for the characterization of mode I fracture in this material.

B. Comparison between Simulations and Experiments for Mixed-mode I+II Loading

Simulations associated with the specimens reported in the experimental section for mixed-mode I+II loading are explored. The initial crack geometry of specimen CT_31 was used in these simulations. The initial straight crack of length a is modeled as follows: the double nodes are used within the length of $(a-2l_0)$; the length $2l_0$ ahead of these double nodes are meshed with a line of elements whose phase-field nodal values are prescribed to be zero. The mesh effect was also explored in these simulations: we used a structured mesh (with $h = l_0/4$) and two unstructured meshes (with both $h = l_0/4$ and $h = l_0/16$) in the area around the expected path of the crack.

The results for the simulation associated with specimen CT_31 are presented in Figure 3.20 and 3.21. Figure 3.20b shows the crack path comparison for the simulations using structured and unstructured meshes. The mesh effect manifests itself in the deviation in crack paths as well as load-COD curves (see Figure 3.21). The crack path from structured mesh exhibits a stair step curve, while it is smoother in the case of unstructured mesh. This implies that the unstructured mesh is preferable since it can represent the curvature of the crack path under mixed-mode I+II better. The crack paths for the unstructured meshes size of $h = l_0/16$ and $h = l_0/4$ are not different, but the load-COD curves are not the same and have a small deviation. This can be explained by the fact that the fracture energy release rate amplification formula proposed by Bourdin et al. (2008) is not an exact formula but an approximation. The smaller mesh size simulation gives a closer load-COD behavior for the elastic portion where the crack has not growth. For both meshes, the critical loads are higher in comparison to the experimental data. The simulations using unstructured meshes can predict the crack path very close to the experimental data, but the load-COD curves still exhibit discrepancy. The discrepancy may be caused by the difference in the boundary conditions enforced in the simulation and the actual boundary conditions used in the experiments: the pin supports for the two pin-holes must be modeled as contact boundary condition in the simulations, but the current version of our code is not able to handle this kind of boundary conditions. For the case of mode I loading discussed in previous section, the crack grows along the surface of symmetry, thus the specimen rotation is small. In the case of mixed-mode I+II the crack goes off the plane of symmetry which causes the rotation of specimens. The boundary conditions used in our code prevent this rotation; and this causes some discrepancy to occur. We suspect that if the boundary conditions are modeled exactly as those used in the experiments, the phase-field simulation may predict the crack path and structure response under mixed-mode I+II loading more accurately.

Based on the comparisons explored in these sections, it can be stated that the phase-field model provides an acceptable simulation for the global response of the structure, as well as the growth of the crack for the in-plane mixed-mode I+II problems. Some details of the local field, in the vicinity of $8l_0$ are likely to be incorrect as a result of the approximation of the fracture process; this could be important in problems where the local fields are needed accurately.

3.3 Mixed-mode I+III Fracture: Simulation of Echelon Crack Formation

It is clear from Chapter 2 that the parent crack will fragment into daughter cracks under mixed-mode I+III loading. The continued growth of daughter cracks shown a coarsening pattern through shielding mechanism. At some stage the coarsening stops and the system of daughter cracks and unbroken segments of parent crack front grow together under a steady state regime. In this section, we will explore the capability of the phase-field model in the predicting these complex fracture patterns under mixed-mode I+III loading conditions.

3.3.1 Mode I + III Loading Simulation

The geometry used in this simulation is a slab of dimensions $20\alpha \times 10\alpha \times 30\alpha$, where $\alpha \sim 10 l_0$ is the cohesive zone size (see Figure 3.22a). The domain was meshed uniformly with the element size of l_0; the mesh contained of 6 million hexahedral elements. The initial crack was modeled with the length of α in the ***x*** direction; periodic boundary conditions are imposed at $z = \pm 15\alpha$. The elastic K-field displacements corresponding to mixed mode I + III loading are prescribed on the other outer surfaces of the simulation box, at $x = -\alpha, 19\alpha$ and $y = \pm 5\alpha$:

$$\begin{Bmatrix} u_x(r,\theta) \\ u_y(r,\theta) \end{Bmatrix} = \frac{(1+\nu)K_I^\infty}{2E}\left(\frac{r}{2\pi}\right)^{\frac{1}{2}} \begin{bmatrix} (2\kappa-1)\cos\left(\frac{\theta}{2}\right) - \cos\left(\frac{3\theta}{2}\right) \\ (2\kappa+1)\sin\left(\frac{\theta}{2}\right) - \sin\left(\frac{3\theta}{2}\right) \end{bmatrix}$$
$$u_z(r,\theta) = \frac{4(1+\nu)K_{III}^\infty}{E}\sqrt{\frac{r}{2\pi}}\sin\frac{\theta}{2} \tag{3.25}$$

where (r,θ) are the polar coordinates in the ***x-y*** plane with the origin at the crack tip. Load increment was prescribed by increasing K_I^∞ and K_{III}^∞ in small steps, maintaining the ratio $\beta = K_{III}^\infty / K_I^\infty$ constant; growth of the crack was captured in the simulations for three cases: $\beta = 0, 0.3, \infty$. In all three cases, the crack extended along the initial crack plane; the predicted crack extension for pure mode III loading case is shown in Figure 3.22b. Visualization is enhanced by showing only those elements with $c < 0.1$. Noting again that initiation of the crack is identified corresponding to the load step when the crack had extended by $2l_0$ from the initial crack, the pure mode III crack started growing at $K_{III}^\infty = 0.87 K_{IC}$; for the case of $\beta = 0.3$, the critical value of stress intensity factors was found to be $(K_{Ic}^\infty, K_{IIIc}^\infty) = (0.96, 0.29) K_{IC}$. These critical values are plotted in Figure 3.22c as red dots, where the corresponding prediction from the energy criterion in Eq.(1.2) is also shown as the blue line. Clearly, the simulations agree with the energy criterion; this agreement also confirms that the crack path that minimizes the potential energy is planar extension of the crack! However, the experimental observations for pure mode III loading (Knauss, 1970) in which the crack front fragmented into numerous daughter cracks oriented in the direction perpendicular to the principal stress direction, and a whole host of other results at different levels of mixed-mode I + III, and in a number of different materials ranging from soft materials such as hydrogels (Ronsin et al. 2014, results from Section 2.3 of Chapter 2) and cheese (Goldstein and Osipenko, 2012) to hard materials such as rock (Pollard et al. 1982) and glass (Sommer, 1969) contradict this picture – instead of extension of the crack along the original plane, the crack front fragments immediately. While it might be argued that this is probably due to the bluntness of the parent crack in some experiments, the most recent work of Ronsin et al. (2014) and the results reported in Section 2.3 of Chapter 2, demonstrate that even naturally grown, sharp crack fronts fragment upon the application of even a very small amount of mode III.

We believe that this points to a fundamental limitation in the energetic formulation of the fracture problem as posed: the energy criterion is a necessary condition, but not sufficient; while the minimum energy configuration of planar extension under mode III is energetically admissible, it is not achievable because there exists a barrier to this mode. It is quite simple to identify the nature of this barrier: if the material cannot provide deformation and failure mechanisms that can exploit this plane ahead of the crack then it can be loaded beyond the state indicated by the failure criterion, until the energetic condition corresponding to the next mechanism of failure is attained; such a barrier must, of course, depend on the material. Under pure mode III, the plane ahead of the crack has zero normal stresses; hence no damage mechanism can be activated for very brittle materials; on the other hand, planes inclined at 45° provide the largest tension and hence any damage that develops will be biased in this orientation and can fundamentally inhibit extension of the crack on its original plane. On the other hand, in very ductile materials, such as clay, failure can develop under shear and preliminary experiments show that crack extension does occur along the extension of the initial crack plane. However, the phase field formulation based on the maximum tensile stress (or strain) does not account for these differences. Hence the phase-field formulation must be augmented to account for this effect; one possible augmentation is to provide for a distribution of initial damage that can grow in the enhanced stress field in the vicinity of the parent crack and provide a "damage structure" that accounts for the stress state. This is a possible way to nucleate daughter cracks from the parent crack and is explored further in this work.

3.3.2 Mixed-mode I+III Simulations with the Perturbation of a Parent Crack Front

In view of the discussion above, we explore the role of defects and perturbations of a parent crack front by imposing distributed defects or discrete nucleation of daughter cracks. The domain used in the simulations in the following sections is a rectangular block of size $200l_0 \times 50l_0 \times 200l_0$, except for the simulation for the discrete nucleation of six daughter cracks under pure mode III loading in Section 3.3.2E in which case a domain of $200l_0 \times 100l_0 \times 200l_0$ was used. The initial crack was modeled as a circular notch with a radius $r_p = 0.5l_0$; and the crack length was set to $60l_0$. The computational domain contained about 2.5 million (5 million for the mesh used in Section 3.3.2E) linear 8-node hexahedral elements with the smallest element size on the order of l_0. The elastic K-field displacement associated with pure mode III or mixed-mode I+III loading (Eq.(3.25)) was prescribed on the boundary surfaces of the simulation domain $x = -60l_0, 140l_0$ and $y = \pm 25l_0$ ($y = \pm 50l_0$ for the simulation domain used in Section 3.3.2E) and periodic boundary conditions were prescribed on $z = \pm 100l_0$.

A. Pure Mode III Loading: Parent Crack with a Single Inclined Daughter Crack

The first simulation provides a repetition of the BEM calculation in Section 2.1.3 of Chapter 2 to explore the shielding effect of the daughter crack on the parent crack front which undergoes mixed-mode I+III loading. It was shown that the nucleation of a daughter crack alters the stress state of the portion of parent crack front surrounding the location of the daughter crack: the stress intensity factors for modes I and III on the parent crack drop in the immediate vicinity of the daughter crack; with distance away from the site of the daughter crack, the stress intensity factors along the parent crack gradually return to the far-field values that correspond to the imposed uniform values, with a small peak at about one radius from the daughter crack. In this section, we revisit this shielding effect through a simulation based on the phase-field model. The parent crack font was perturbed by prescribing an initial strain history field for a daughter crack located at the central portion of the parent crack front with the radius of $r_d = 15 l_0$; the daughter crack was oriented with an angle 45° with respect to the parent crack surface (daughter crack plane is perpendicular to the principal stress direction under pure mode III far-field loading). Snap-shots of the crack evolution are shown in Figure 3.23; the single daughter crack shielded the parent crack front in its neighborhood by perturbing the stress state of the parent crack front. As a result of this shielding the growth of the parent crack front is inhibited near the daughter crack and the initially straight parent crack acquires curvature in the *x-z* plane. The development of the curved portion of the parent crack front also converts the applied mode III loading to produce a large mode II loading within this portion of the parent crack front; the existence of significant amount of mode II causes the parent crack front near the daughter crack surface to turn continuously, as indicated in Figure 3.23. But in reality, there are always many daughter cracks that are nucleated simultaneously; also they are close to each other to prevent the generation of mode II on the parent crack, thus preventing the rotation of the parent crack front.

B. Pure Mode III Loading with Defects

In order to prevent the phase-field simulation of the mode III from growing straight ahead, a barrier needs to be erected in the simulation. In view of the fact that damage should occur preferentially in one orientation relative to the crack plane, one strategy is to establish, in addition to the stress field dictated by the crack tip loading, an initial field of damage that would evolve along specific directions dictated by the stress field. In principle, this requires the distribution of damage in a region that is large in comparison to l_0. This distribution could account for the experimental observation that fragmentation of a parent crack front may be the result of nucleation of daughter cracks from imperfections along the parent crack front. In order to explore this aspect further in the phase-field simulation, defects were introduced along the parent crack front by prescribing the strain history field using the following procedure. First, a set of nodes that are inside a tube along the parent crack front is selected (the tube axis is parallel to the parent crack front line and its cross-section has the shape of a rectangular box of dimensions $30l_0 \times 20l_0$ centered at the location $x = 5l_0, y = 0$). Then, from this set of nodes 0.06% of nodes are selected randomly with the constraint that no pair of nodes lies within a distance less than $5l_0$ in order to prevent clustering of defects. The phase field parameters for these nodes are set to zero, indicating completely failed material. One could, in fact, provide a distribution of c values to account for variability in the nature of the defect. The nodes which were assigned defects are shown as dots in the image 0 of Figure 3.24. In each image of this figure, the full 3D view of the phase-field is shown in the left side, two projected views of the 3D view in the $+\mathbf{n}$ or $+y$ (top right image corresponding to a projection on the original crack plane) and $-\mathbf{b}$ or $-x$

(bottom right image corresponding to a view along the original crack front) directions of the parent crack. The image sequence follows different stages of loading increment; a fully interactive 3D image of this result corresponding to loading stage associated with image 5 is included in Supplementary Material M1; a video of this simulation is available as Supplementary Material V1. The load level associated with image 0 corresponds to the critical load at which the parent crack started to grow in the absence of defects (see Section 3.3.1). It is important to note that significant crack front damage has not developed at this stage yet. Clearly, the distributed defects begin to accumulate damage in the enhanced stress field near the crack tip at loading stage 1; but this must also alter the stress state everywhere along the parent crack front. The daughter cracks did not orient themselves perpendicular to the principal stress direction (the twist angles at the nucleation stage were not 45°, see images 1, 2). The structure of the daughter cracks emerges as they grow through the region of the defect distribution. By the time the daughter cracks grow by about $20l_0 - 50l_0$, somewhere between images 4 and 5, the daughter cracks are fully developed, with an angle of 45° with respect to the parent crack. This can be taken as the nucleation stage of the daughter crack structure. The continued growth of the daughter cracks occurs without change in the orientation. The bridge regions between the daughter cracks do not develop cracks or damage; this can be visualized most easily in the 3D view in the Supplementary Material M1. Furthermore, coarsening of the spacing between the daughter cracks is clearly observed: the number of daughter cracks decreases from six partially developed daughter cracks (with significant disorder) in image 2 to three daughter cracks in image 5. The shielded cracks are identified in images 4 and 5. This simulation could not be continued further since the daughter cracks begin to interact with the boundary of the simulation box. Identification of crack extension beyond this requires expansion of the simulation domain, but limitations in computational resources make this a difficult task to undertake.

The effect of the defect density was also explored. In the next simulation all parameters of the previous simulation were maintained unchanged, except for the defects density which was increased by 10 times to 0.6% and the minimum distance between the defects which was decreased from $5l_0$ to $4l_0$. The results of this simulation are shown in Figure 3.25. Increasing the defects density magnifies the roughness of the fracture surface for the daughter cracks and forces the daughter crack fronts to rotate earlier compared to the low defect density case. But as the daughter cracks grow to a large size, there is not much distinction between the two cases with a ten-fold difference in the defect density. But this is not true as the defect density becomes very large; in this case, the defects interact with each other and smear out the damage to form a "blunt" parent crack front. Thus, for the case of excessive defect density the parent crack grows along the planar extension of the initial crack and produces a planar mode I crack surface with some roughness. In all the simulations discussed in the following sections, a defect density of 0.06% is assumed, unless stated otherwise.

C. Mixed-mode I+III loading with defects

The simulations presented in the previous section considered pure mode III loading. Now simulations for mixed-mode I+III loading also results in daughter crack nucleation; the specific case of $\beta < \beta_c$ below the critical ratio for fragmentation as predicted by linear stability analyses corresponding to a helicoidal perturbation of the parent crack front (Leblond et al., 2011) is considered in this section. The far-field elastic K-field loading applied was associated with mixed-mode I+III $\beta = 0.3$ which is half of threshold of fragmentation for the material with Poisson's ratio $\nu = 0.26$. The simulation set-up was as for the case of pure mode III loading with 0.06% of defects in the vicinity of the parent crack, with the exception that the loading was associated with mixed-mode I+III. The resulting initiation and growth of daughter cracks are shown in Figure 3.26; the projections shown are the same as in the case of Figure 3.23. The image sequence follows different stages of loading increment; a fully interactive 3D image of this result corresponding to image 6 is included as Supplementary Material M2; a video of this simulation is available as Supplementary Material V2. The parent crack fragmented immediately, even though the loading was well below the predicted instability threshold. This clearly adds further evidence that the formation of daughter cracks does not follow the linear instability mechanism, but is more directly a nucleation problem. The daughter cracks initiated and grew out of the field of defects, and emerge as fully developed cracks with an orientation of about $26°$ (as predicted by Eq. (1.4)). As with the pure mode III case, continued growth of the daughter cracks occurs without a change in the orientation. Also, the bridge regions between the daughter cracks do not develop cracks or damage as can be visualized most easily in the 3D view in the Supplementary Material M2. The simulations were continued to larger loads in order to follow tendencies for coarsening; it was found that as the daughter crack grew farther away from the parent crack, cracks developed close to the parent crack front, but normal to the parent crack, resembling fins of a fish; following Adams and Sines (1978), we call them “fish fin” or “fin” cracks. It appears that the formation of such “fish fin” cracks is the result of applying loads based on the crack tip located at the initial tip, and not accounting for the progression of an “effective” crack with the development of the system of daughter cracks; also, the small domain of the simulation box would play a role in this. Once again, to fully capture the evolution of the daughter crack a larger simulation region is required.

D. Critical Conditions for Initiation of Mixed-mode I + III Cracks

The set of phase-field simulations of the growth illustrated here permits an exploration of the critical loading conditions at the onset of daughter crack nucleation, and helps provide a comparison between the linear instability based formation and the nucleation based formation of the daughter crack structure. Towards this end, the critical conditions at crack initiation $\left(K_{Ic}^{\infty}/K_{IC}, K_{IIIc}^{\infty}/K_{IC}\right)$ corresponding to pure mode III loading and mixed-mode I + III loading with $\beta = K_{III}^{\infty}/K_{I}^{\infty} = 0.3$ were identified using the procedures used for the corresponding simulations without defects (see Section 3.3.1); these values are shown in Figure 3.22c. For the case of pure mode III, the introduction of defects increases the effective fracture energy by 3.05, while for $\beta = 0.3$, the effective fracture energy increases by 2.5. This provides clear evidence that the distribution of damage over a region much larger than l_0 has two consequences: first, the growth of distributed damage prevents the lower-energy mode of crack extension on the prolongation of the original crack plane. Second, it provides a mechanism for the nucleation of the daughter cracks directly by growth of damage and formation of cracks. The energy dissipated in this process is greater than the Griffith threshold. The mechanism of coarsening by elastic shielding through fluctuations is also seen. The remaining ingredient of the mixed-mode cracking process is the termination of coarsening due to growth of the remnants of the parent crack (or growth in the bridging region). This requires a larger simulation box or a strategy where the simulation is begun past the nucleation stage; the latter is considered in the next section.

E. Mixed-mode I + III Loading with Discrete Representation of Daughter Cracks

The case of discrete daughter cracks emanating from a parent crack under mixed-mode loading is considered in this section; the reasons for this are two-fold. First, potentially this permits the examination of termination of coarsening as indicated above.

Secondly, in the experiments reported in Section 2.2.2B of Chapter 2 on H-100, for a certain bluntness of parent cracks, it was noted that nucleation of daughter crack required a very high load level, which in turn, produced a large amount of energy storage in the specimen. Thus, as a daughter crack initiated, it grew dynamically to a large size. Larger daughter crack will shield a longer parent crack front segment and the neighbor daughter cracks will be at a large spacing. As a result a small number of discrete daughter cracks are nucleated (see Figure 2.14 of Section 2.2.2B for an example).

The simulation domain and boundary conditions (mode III or mixed mode I + III loading) are exactly the same as in previous simulations, except for the box dimension the y direction is increased by a factor of two. The case of nucleation of six daughter cracks is considered first; these daughter cracks have the same size and orientation as in the previous simulation for the case of one daughter crack for the pure mode III loading, but the interior daughter cracks were positioned $33.3l_0$ apart while the first and last daughter cracks were at the distance $16.65l_0$ from the free surfaces to generate a perfectly periodic pattern. The results of the simulation corresponding to pure mode III loading are shown in Figure 3.27. Image 0 corresponds to the initial condition where nodes with $c < 0.2$ are shown. In image 1, the unbroken segment of the parent crack front started growing before anything happened to the daughter cracks. This can be understood by the following argument: as a daughter crack grows at fixed far-field loading, the stress state along its front will drop; in order for this daughter crack to continue growing, the far-field loading needs to be increased. This, however, will result in a further increase of the stress along the unbroken parent crack segment as well and the unbroken segments of the parent crack front may reach a critical state before the daughter crack fronts. This occurs when the introduced daughter cracks are at a significant distance from the parent crack front. Image 2 shows that all the daughter crack fronts as well as the unbroken segments of parent crack front grow simultaneously: the daughter cracks grow nearly in their own plane while the parent crack fronts exhibited some undulation in the shape. This undulation was caused by the fact that at the two ends of each parent crack front segment, the crack front grows in the direction perpendicular to the daughter crack surfaces; this undulation will have an effect in the interaction between the parent crack and the daughter cracks. With the progression of the far-field loading, both parent and daughter cracks continued growing together, but the parent crack front rotated and connected with the back-end of the daughter crack fronts; this should, once again be an effect of the small size of the simulation domain. The growth of daughter cracks also shows the coarsening scenario; at the last loading step there were only two surviving daughter cracks; this can be visualized most easily in the 3D view in the Supplementary Material M3. These simulations were performed in small cell sizes and hence interactions between the daughter cracks themselves and with the cell boundary place significant limitations on the information extracted from the coarsening. For example, it is difficult to establish a precise limit on the spacing between the daughter cracks as a function of the mode mix, but the key ingredients observed in the experiments reported in Sections 2.2 and 2.3 of Chapter 2 are reproduced in the simulations as well.

We also considered the discrete perturbation of parent crack front subjected to mixed mode I + III, with $\beta = 0.3$; in this case three initial daughter cracks of the same size $r_d = 15 l_0$ oriented with an angle $26°$ relative to the parent crack surface were prescribed through the initial strain history field. The resulting initiation and growth of daughter cracks are shown in Figure 3.28. The continued growth of the daughter cracks occurs without change in the orientation. The bridge regions between the daughter cracks do not develop cracks or damage; this can be visualized most easily in the 3D view in the Supplementary Material M4. The parent crack grows first (see images 1 and 2) for the same reasons discussed above; with increased far-field loading, both parent and daughter cracks grow together (see images 3 and 4) and form a crack front with six connected segments. As the system of cracks grows further (image 5-8) the growth segments of parent crack front merged with the daughter crack surfaces and eventually form three facets at the final loading step. The "fish fin" cracks were also observed in the last stage of this simulation whose formation makes the approach to steady state growth of the system of parent and daughter cracks more difficult.

3.4 Structural Prediction – Growth of an Interior Center-Crack under Tensile Loading

As a last illustration of mixed-mode crack growth, we consider phase-field simulation for the growth of an interior center-crack under uniaxial load. The mixture of modes I, II and III arise in this problem, and this mixture varies continuously along the crack front. The simulation domain is a rectangular box of dimensions $L_x \times L_y \times L_z = 200 l_0 \times 200 l_0 \times 100 l_0$; it is discretized with a mesh containing five million 4-node linear tetrahedral elements. The smallest elements are of the size l_0 in the region around the initial center-crack. The center-crack has the radius of $20 l_0$ and its normal is oriented at an angle of 45° with respect to the tensile loading direction. The center-crack itself was modeled by a double node surfaces. Displacements corresponding to the uniaxial tensile load were prescribed on all the outer surfaces of the simulation box; the prescribed displacements were increased monotonically during each loading step. Snap-shots of the center crack growth are shown in Figure 3.29: each image shows a full 3D view, a view perpendicular to the loading direction (top right of the image) and a view parallel to the initial crack plane (bottom right of the image); a fully interactive 3D image of this result corresponding to image 4 is included as Supplementary Material M5; a video of this simulation is available as Supplementary Material V3. The center-crack started growing first at the two lowest and highest portions of the initial crack front where the amount of mode II loading on the crack tip is high, and mode III is negligible (image 1). Except for those two locations, the mode III loading along the initial crack front is significant and highest at the location of the middle of the crack high (on the plane $z = L_z / 2$). Thus, we expect the initial crack front to fragment under the mode III loading. But the images 2, 3 and 4 show no indication of crack front fragmentation, but the crack turns continuously to a flat crack oriented perpendicular to the loading direction. This is analogous to the response seen under pure mode III simulations of Section 3.3.1, and provides a continuous extension of the center crack; however, the regions of the crack front that experience dominant mode III should exhibit crack front fragmentation (see Adam and Sines, 1975; Germanovich et al., 1994). In order to explore this, the role of defects was explored. All nodes inside a torus centered at the center of the initial crack with major radius equal to the radius of the crack and minor radius of $30l_0$, (but with their normal projections onto the initial crack plane outside the initial crack front circle) were identified; from this node set, 0.2% of nodes were assigned the initial strain history field which enforces $c = 0$. The crack evolution for this simulation with imposed defects is shown in Figure 3.30; a fully interactive 3D image of this result corresponding to image 6 is included as Supplementary Material M6; a video of this simulation is available as Supplementary Material V1. The defects introduce some roughness in fracture surface; and the initial crack front shows possible fragmentation at one location as can be identified in image 3. But, this did not persist for a long distance and the two segments of the parent crack front coalesced and merged into one continuous front. There are two drivers for the continuous evolution of the crack; first, the simulations scale is not fine enough. Since the crack radius is only about $20l_0$, the scale at which fragments of the crack front appear would be only a fraction of this; however, at such small distances, the interactions of both the damage and elastic fields cannot be captured correctly. It appears that a much larger simulation domain is required.

Secondly, the existence of mode II loading everywhere along the initial parent crack front would force the fragmented cracks to turn and merge to each other. Limitations in computational resources made it difficult to explore this problem further. It can be concluded that the phase-field model can predict quite well the overall pattern of the center-crack growth under uniaxial tensile load, but not the local features that include fragmentation and coalescence unless the fine scale is resolved by using length scale l_0 that is significantly smaller than the fragmentation features.

3.5 CONCLUSIONS

The phase-field model of fracture has been implemented in a parallel simulation framework for simulation of three-dimensional linear-elastic fracture problems. The numerical code has been verified for stationary crack problems by comparison of the crack opening displacement with the analytical linear elastic singular solution and the Dugdale-Barenblatt cohesive model solution. Based on these exercises, it was determined that the scale of the fracture process zone is on the order of $8l_0$, and hence the phase-field solutions will deviate from the elastic solutions for a length on the order of $\sim \xi l_0$. Next, the crack opening displacement calculations from the phase-field model were compared for a problem of a microcrack interacting with a macrocrack. Finally, mixed-mode I+II crack growth was simulated using the phase-field model and the results for the crack kink angle and the stress-intensity levels at initiation were compared with models based on the maximum tangential stress, maximum energy release rate criterion, and the principle of local symmetry. All the verification exercises generated excellent agreement with the theoretical/analytical solutions.

Validation of the model was sought through comparison to experiments. Experiments were performed under mode I and mixed-mode loading conditions on compact tension specimens in a theromoplastic polymer, polymethylmethacrylate (PMMA). The materials properties were obtained through direct calibration on the same stock of material. While the elastic response was quite repeatable, noticeable scatter was observed in the case of the fracture tests. Calibration of the fracture energy (or fracture toughness) was obtained by fitting the mean trend over multiple experiments, when considering a steadily growing crack. The mode I and mixed-mode experiments were then simulated using the phase-field code. Very good agreement was obtained when comparing the load vs crack opening displacement response as well as the crack position vs the crack opening displacement response; crack paths were also well-predicted by the phase field model.

The phase-field model was explored further in the simulation for mixed-mode I+III problems. It was shown that the phase-field model will predict the flat mode I crack path for mixed-mode I+III loading, since along this path the energy release is maximum. But the failure mechanism for specific materials places an energy barrier which does not allow for such crack path. Thus, we explored the introduction of defects and discrete nucleation in these problems. This allows the echelon cracks to form, continues growing and exhibits shielding effects, coarsening as we observed in the experimental works of Chapter 2. The issue of length scale l_0 in the crack surface representation was also emphasized in these exercises. This appears that unless l_0 is chosen to be extremely small in comparison to the smallest dimension in the problem, the fragmentation of parent crack will not be captured correctly.

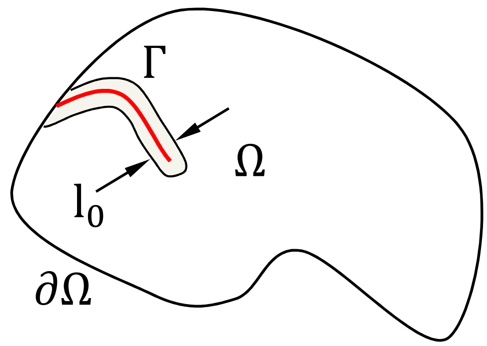

Figure 3.1. A sketch of a solid body with a crack and its phase-field representation

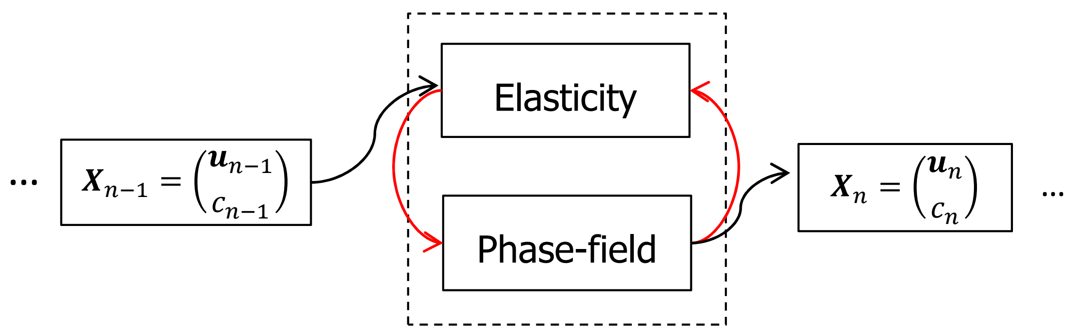

For-loop of load increment n

Do

Solve the linear elasticity problem with $c = c_l$ and update $\boldsymbol{u}_l$

Solve the phase-field problem with $\boldsymbol{u} = \boldsymbol{u}_l$ and update c_l

Increment $l \leftarrow l + 1$

While ($max\left(\frac{\|\boldsymbol{u}_{l-1} - \boldsymbol{u}_l\|}{\|\boldsymbol{u}_{l-1}\|}, \frac{\|c_{l-1} - c_l\|}{\|c_{l-1}\|}\right) > TOL$)

Set $\left(\boldsymbol{u}^n, c^n\right) = \left(\boldsymbol{u}_l, c_l\right)$

Increment of load step n $\leftarrow n + 1$

End of for-loop of load

Figure 3.2. Quasi-static splitting scheme for decoupling the system of elasticity and phase-field PDEs.

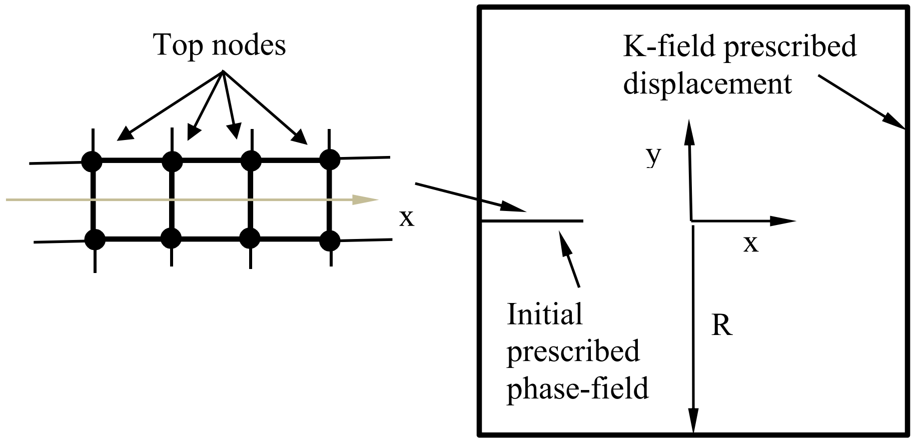

Figure 3.3. Geometry of the crack for the simulations with K-field displacement boundary conditions.

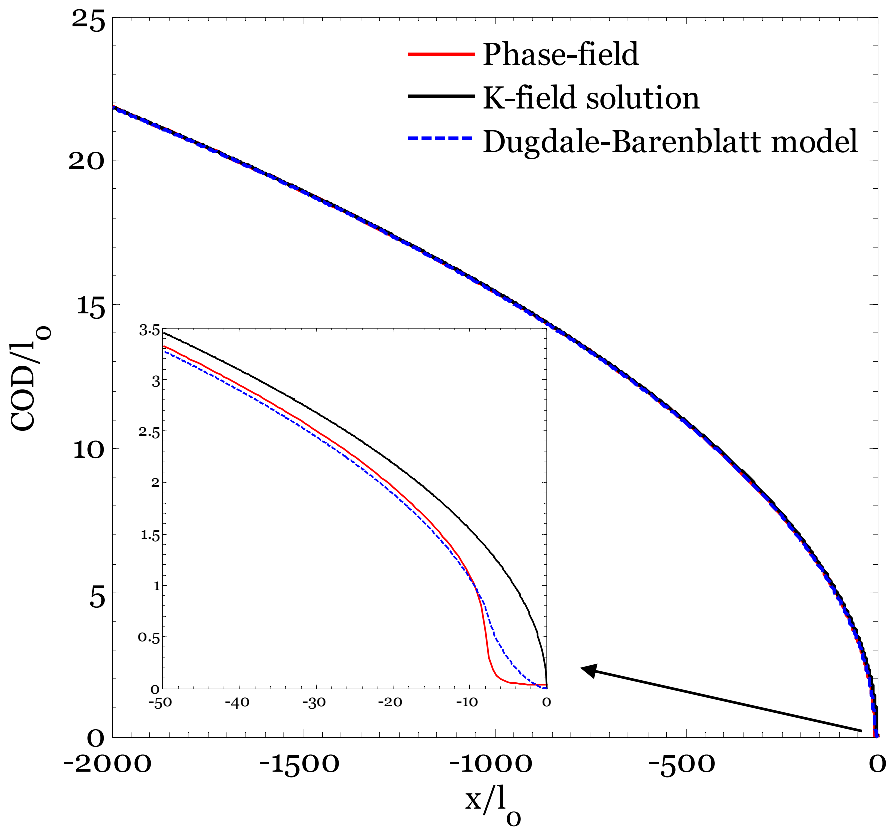

Figure 3.4a. Comparison of the crack opening profile behind the crack tip between phase-field solution, the linear elastic K-field solution and the Dugdale-Barenblatt model. The inserted plot shows an expanded view at the crack tip location.

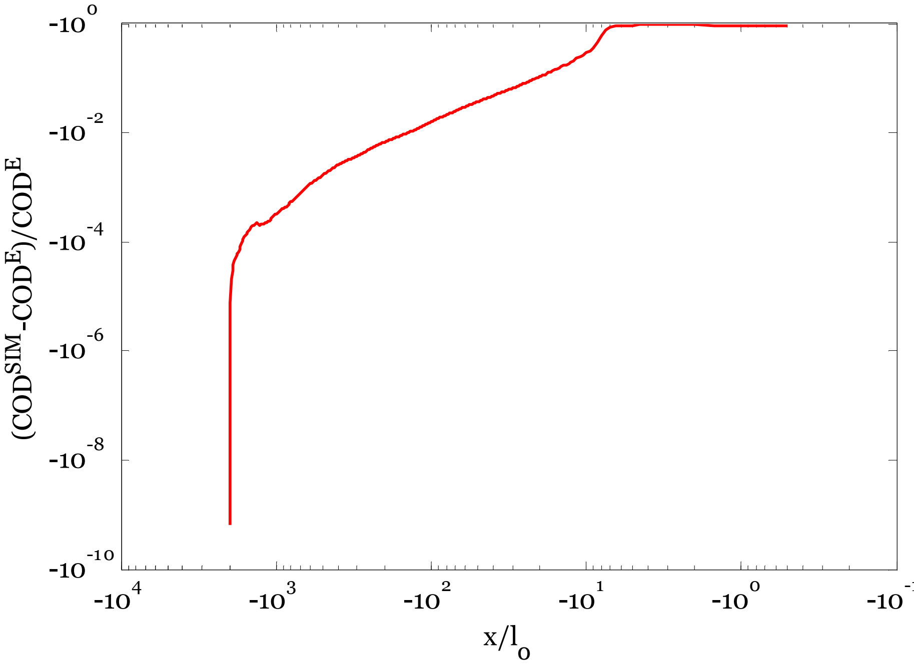

Figure 3.4b. Difference in the COD between the phase-field solution and the elastic K-field solution; to drop this error below 0.1%, one needs to be $\sim 500 l_0$ away from the crack tip.

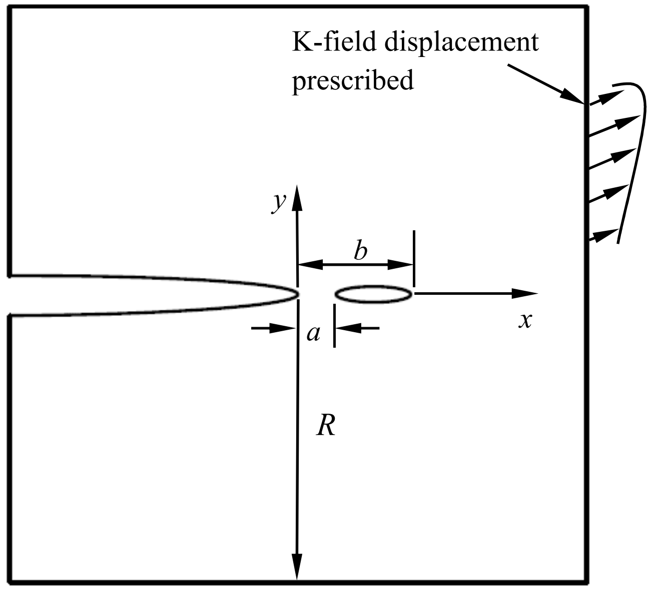

Figure 3.5. Rubinstein's problem set up: $a = 500l_0, b = 6a, R = 10b$, where l_0 is the characteristic length used in the phase-field formulation. The displacement applied on the boundary is the mode I K-field displacement associated with the crack tip at $(x = 0, y = 0)$ location with the mode I stress intensity factor $K_I^\infty = K_{IC} / \gamma$.

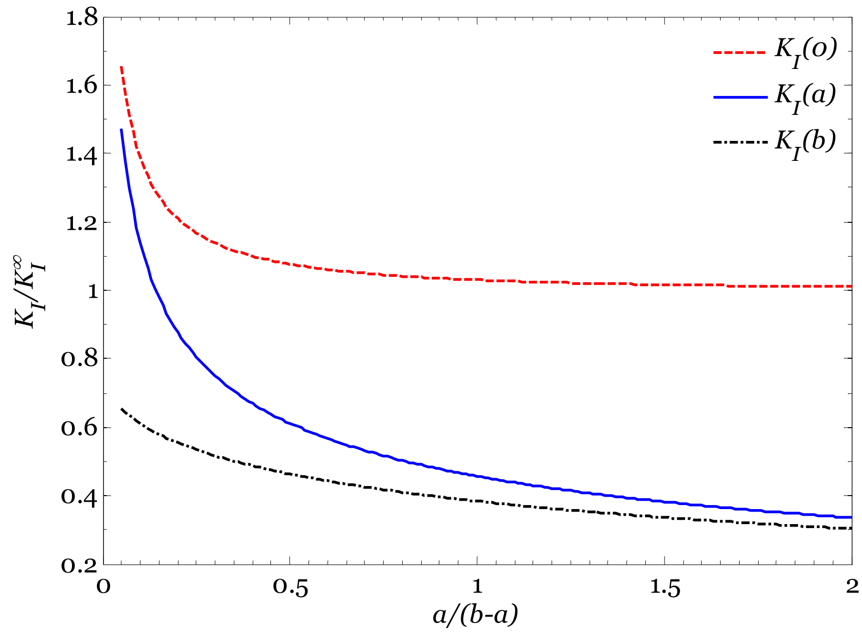

Figure 3.6. SIFs for Rubinstein's problem of interaction of a semi-infinite macrocrack with a single microcrack.

a)

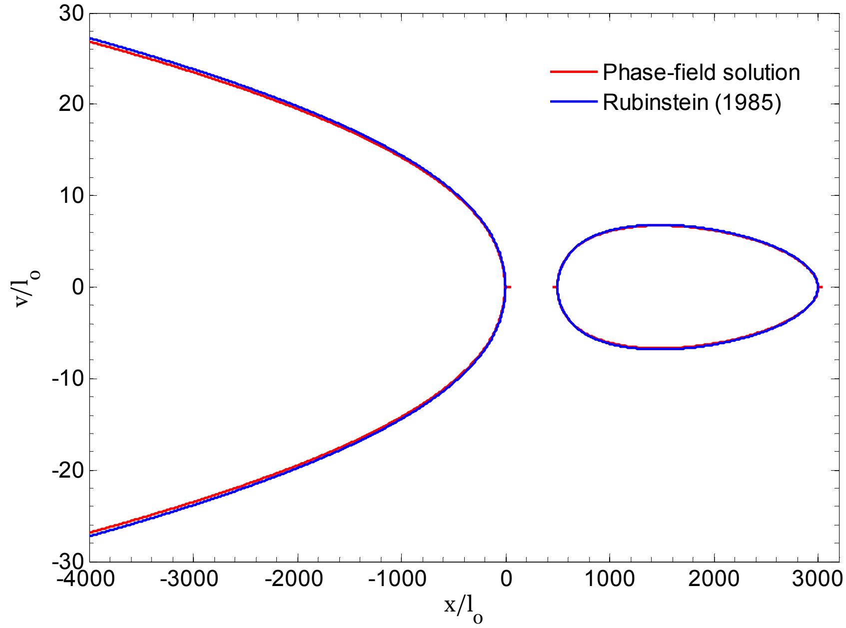

b)

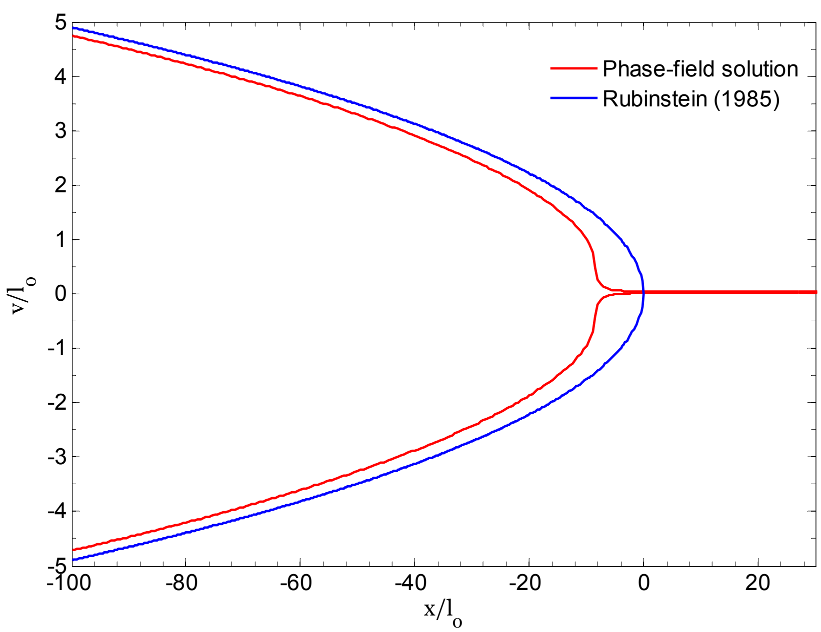

Figure 3.7. Comparison between the phase-field solution and Rubinstein's solution for the case of $\gamma = 1.19$: (a) COD of macrocrack and microcrack, (b) COD near the macrocrack tip.

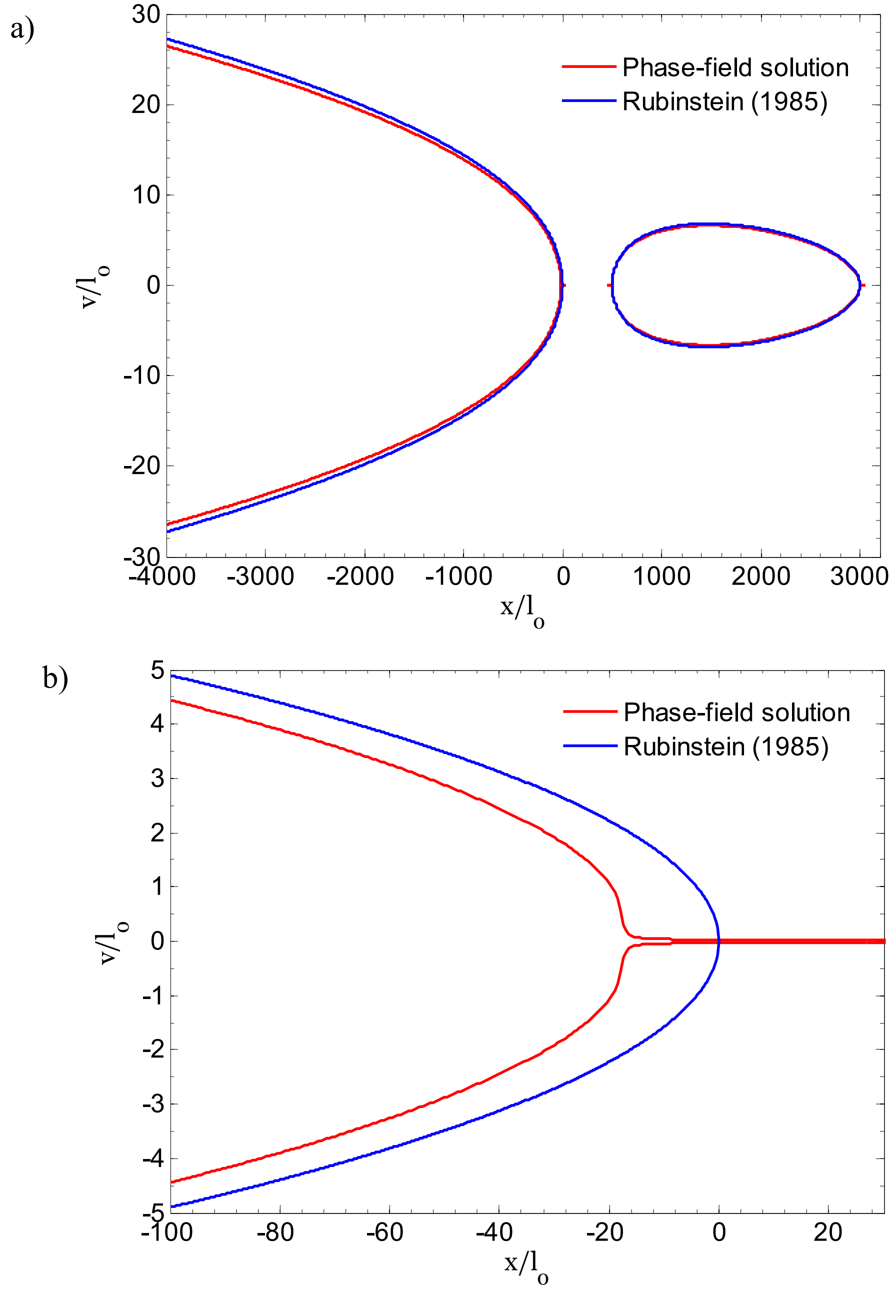

Figure 3.8. Comparison between the phase-field solution and Rubinstein's solution for the case of $\gamma = 1.2$: (a) COD of macrocrack and microcrack, (b) COD near the macrocrack tip.

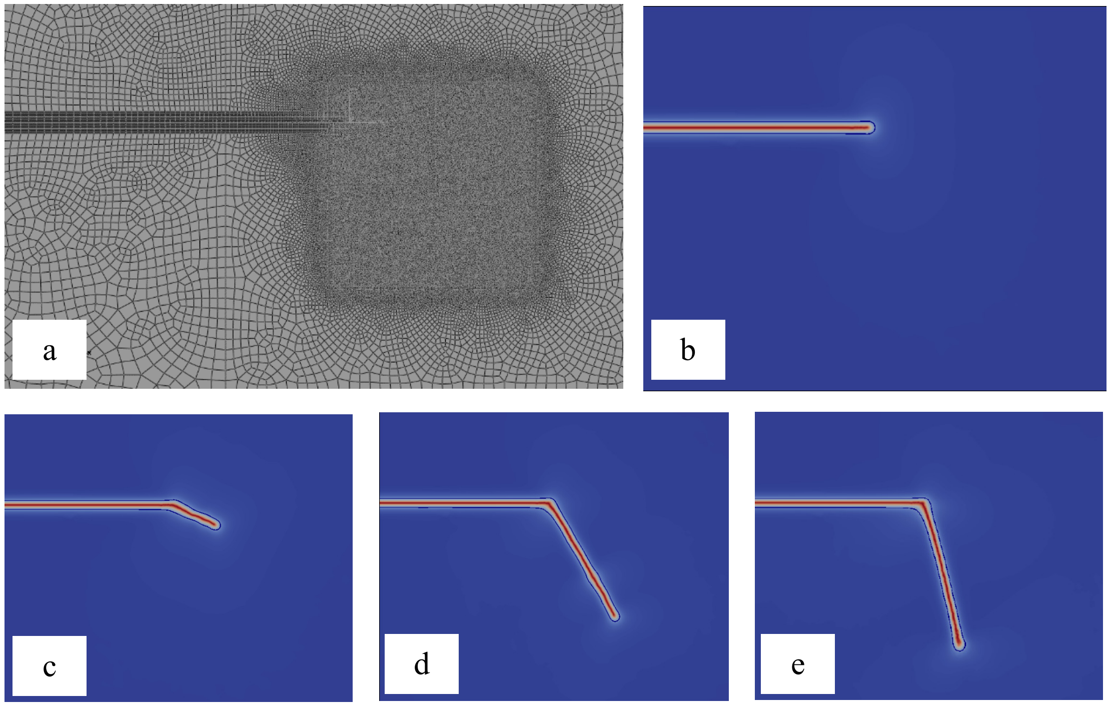

Figure 3.9. Mixed-mode I+II K-field loading simulations. The mesh has very fine regions along the initial crack line and a box area ahead of the crack front as indicated in (a). (b) Shows a crack path under pure mode I loading to form a natural crack; this crack was used as the initial crack in subsequent simulations for mixed mode I+II. (c-e) The crack paths under mixed-mode I+II and pure mode II loading with the ratio $K_{II}^{\infty}/K_{I}^{\infty}=0.28,1.12,\infty$.

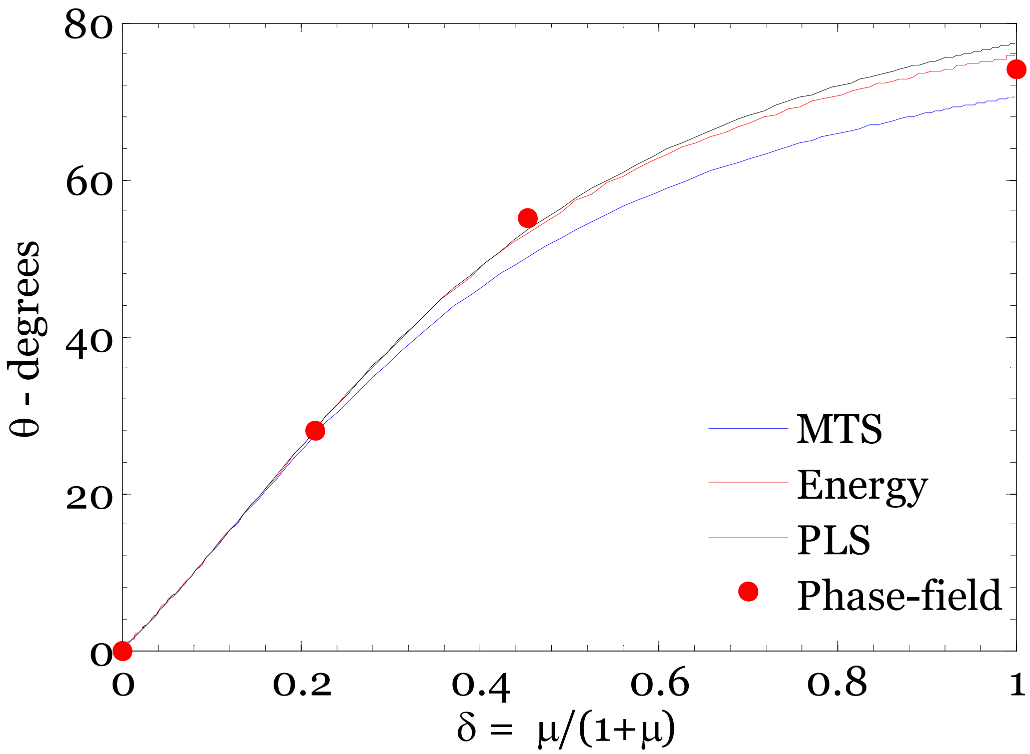

Figure 3.10. Comparison of the crack kink angle prediction from the phase-field model simulation results with the analytical solution for different crack initiation criteria for mixed-mode I+II loading (Note: $\mu = \dfrac{K_{II}^{\infty}}{K_{I}^{\infty}}$).

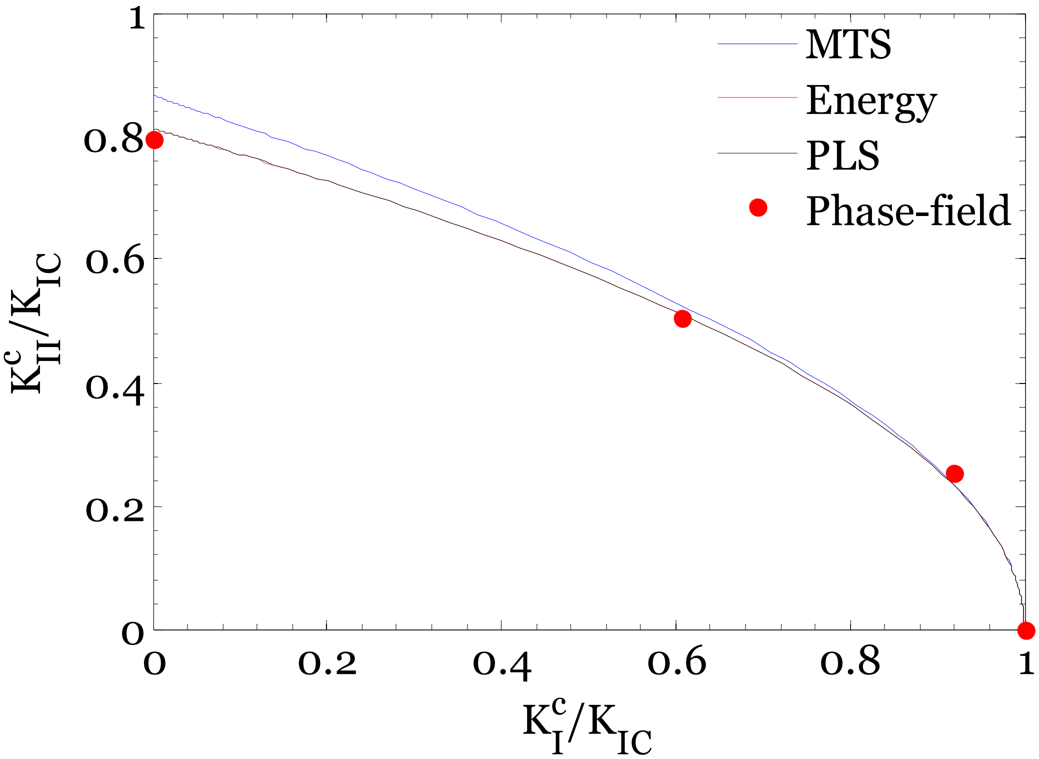

Figure 3.11. Comparison of critical combination of mode I and II SIFs between phase-field model simulation results and the analytical results for different crack initiation criteria for mixed-mode I+II loading.

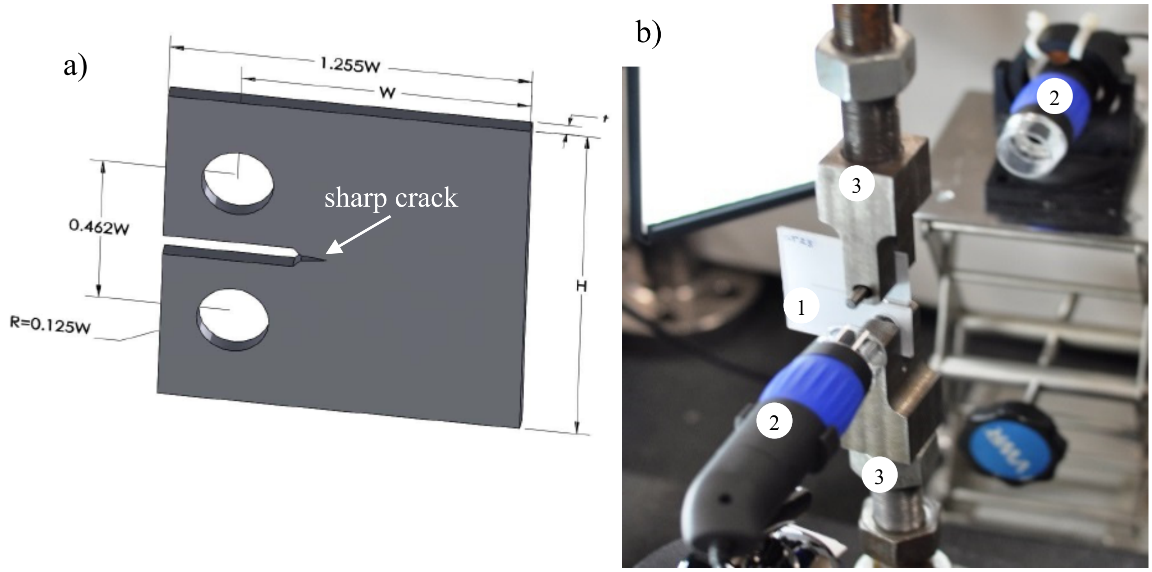

Figure 3.12. (a) Shows a sketch a compact tension specimen. The V-notch tip is located at $0.45W$; and the wedge impact generated a sharp crack which has the length of a from the V-notch tip. (b) Shows the experimental setup: 1 – specimen, 2 – cameras, 3 – loading grips.

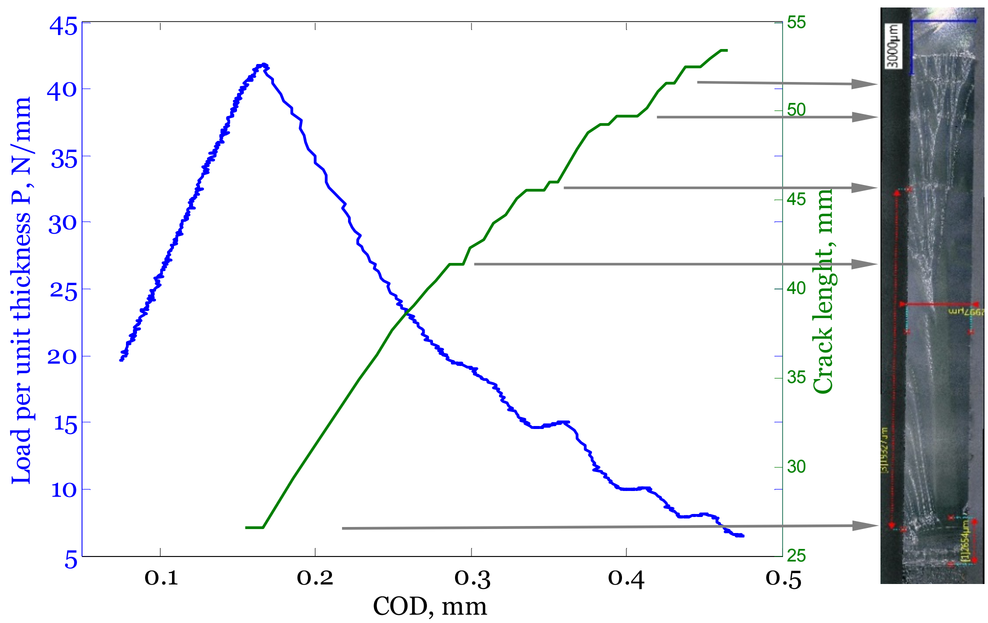

Figure 3.13. Load and crack length vs. crack opening displacement (COD) for specimen CT_24. The micrograph of the fracture surface indicates that the crack stopped many times along the path due to the local variation in fracture toughness; these arrest points are identified by the arrows.

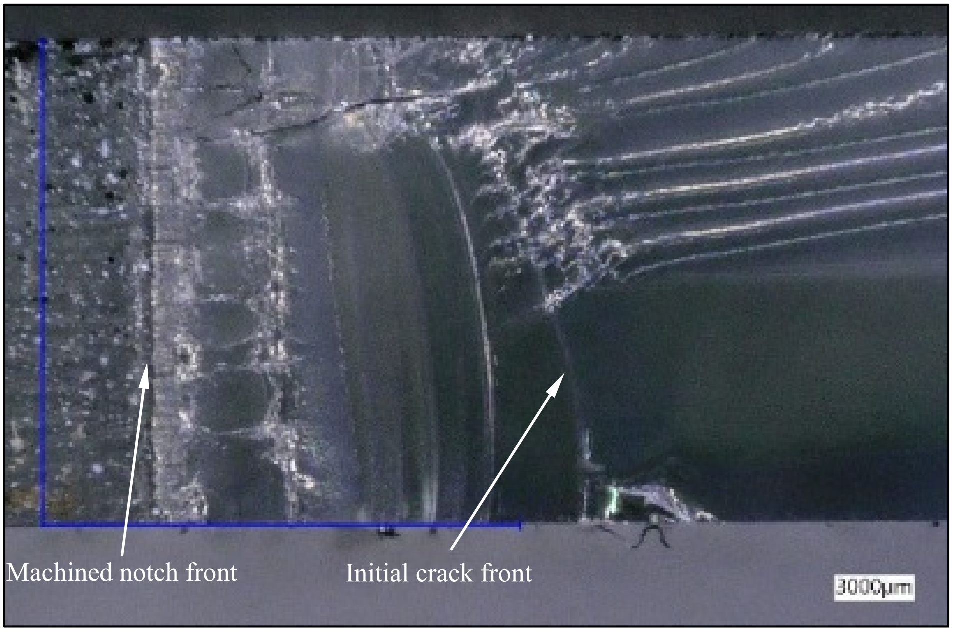

Figure 3.14. Micrograph of the fracture surface of specimen CT_24. The initial crack front generated by razor blade impact was not straight. The fracture surface manifests many striations as the crack propagated; these are due to the fracture surface roughness generated by heterogeneity of the material and the details of the fracture process. The roughness, on the order of $40\mu m$, is evidence of differences in the fracture process at different locations along the crack front.

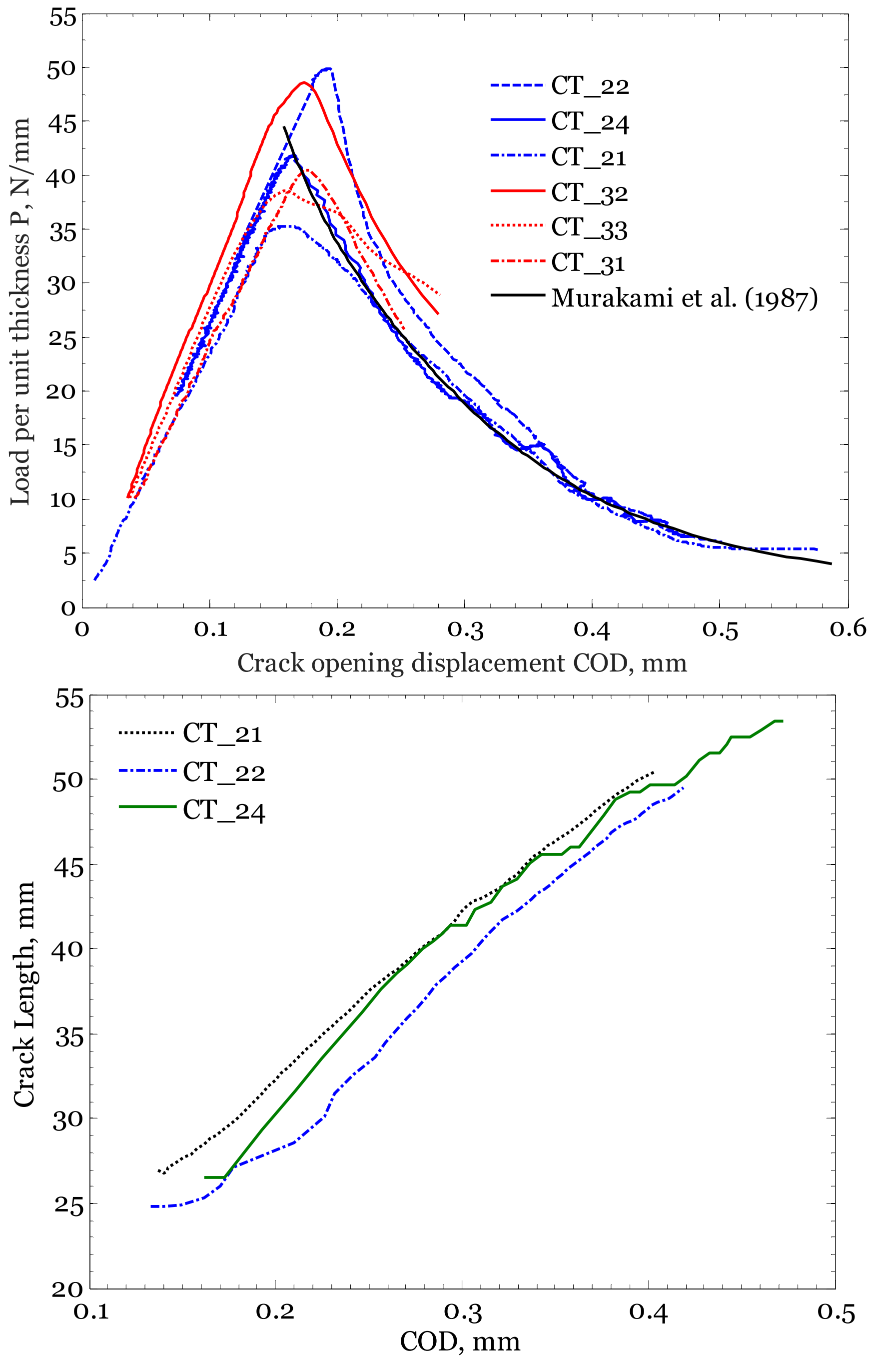

Figure 3.15. Load vs COD and crack position vs COD for the mode I tests using the compact tension geometry.

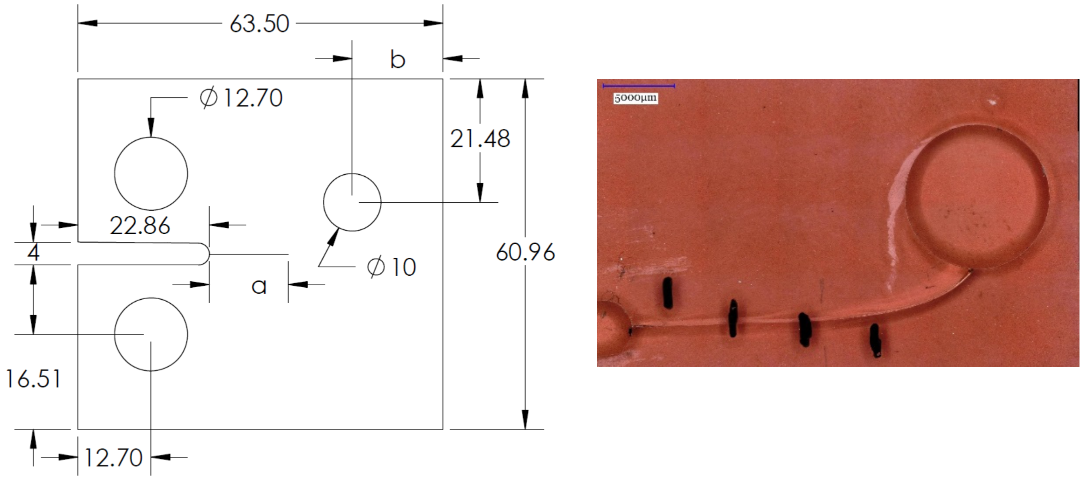

Figure 3.16. Geometry for a modified compact tension specimen with a crack under mixed-mode I+II loading (left), and the final crack path for specimen CT_31 (right).

a)

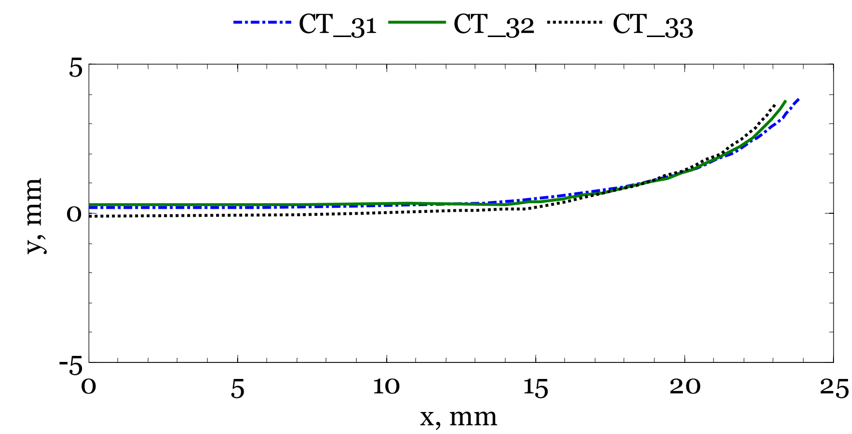

b)

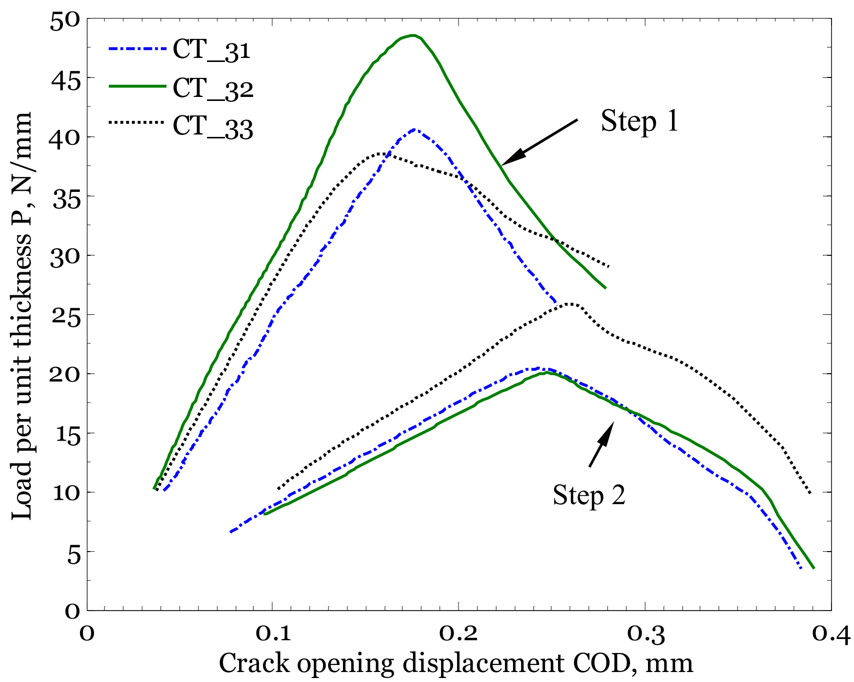

Figure 3.17. Experimental results for mixed-mode I+II loading of specimens CT_31, CT_32 and CT_33 with the initial straight cracks of length $a = 13.47, 14.01, 12.98$ mm, respectively (the hole is located at $b = 15.80$ mm). (a) The crack paths are plotted (the reference is taken to be the tip of the notch). (b) Load vs COD. First, the CT specimens were loaded to grow the straight mode I cracks of initial length a (family of curves labeled Step 1). Then, a hole was introduced into these specimens and they were reloaded (family of curves labeled Step 2).

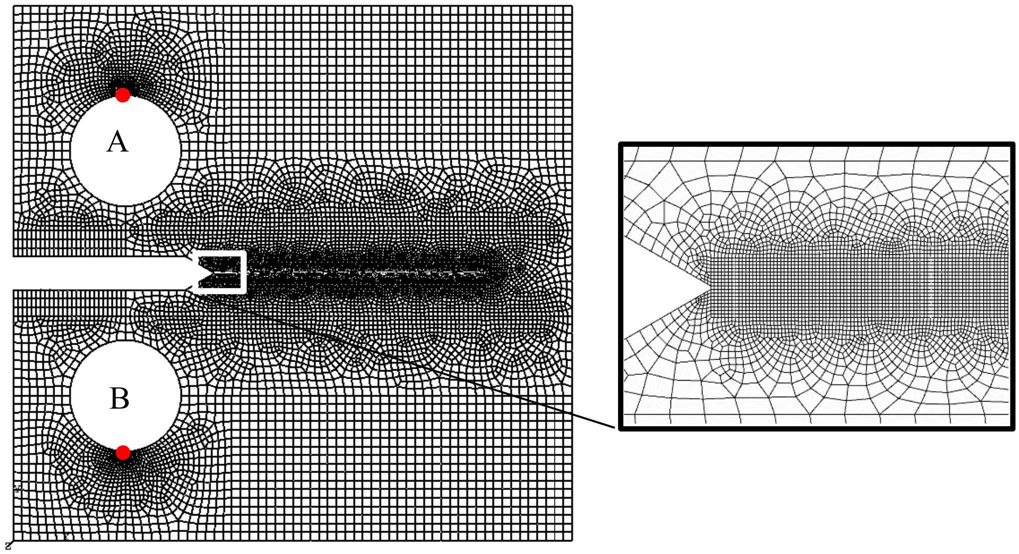

Figure 3.18. Mesh discretization for specimen CT_24. The smallest elements along the crack path have a size of 25 μm. A magnified view of the fine mesh region is shown to the right.

a)

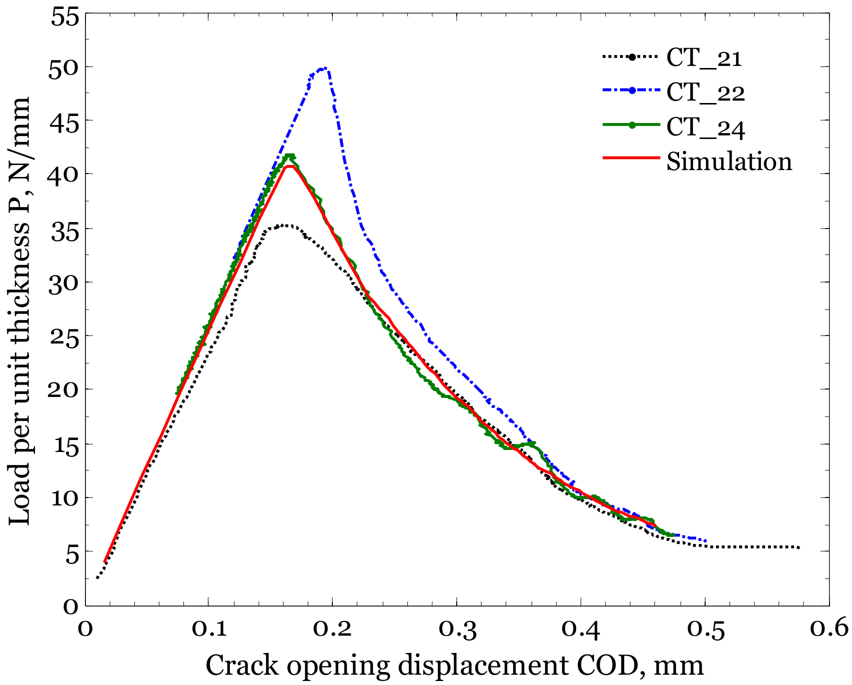

b)

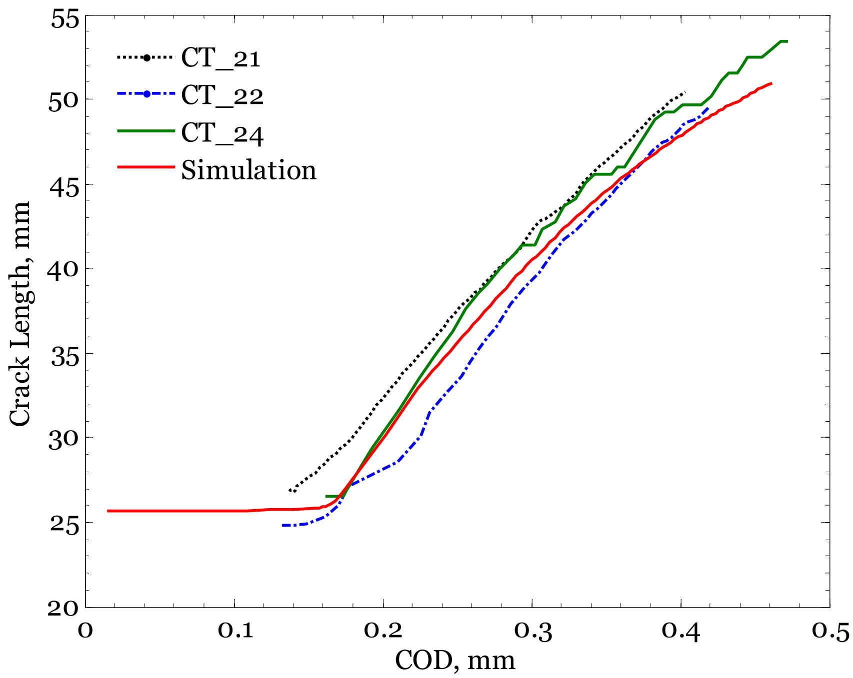

Figure 3.19. Comparison between experimental results and simulations specimen CT_24. The average initial crack length for specimen CT_24 was measured accurately from the fracture surface information and used in these simulations. (a) Load vs COD. (b) Crack length vs COD.

a)

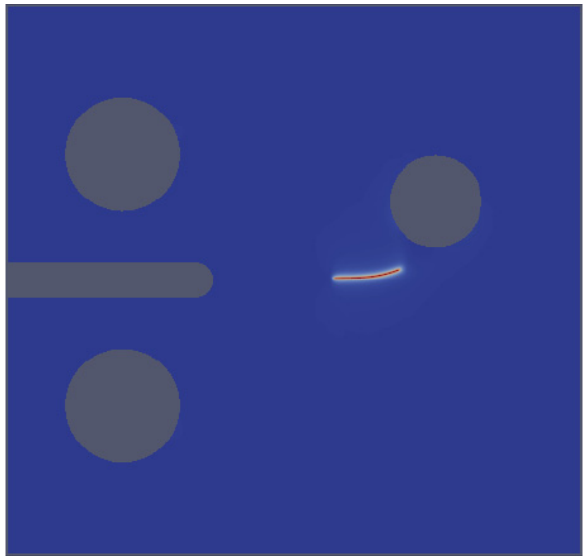

b)

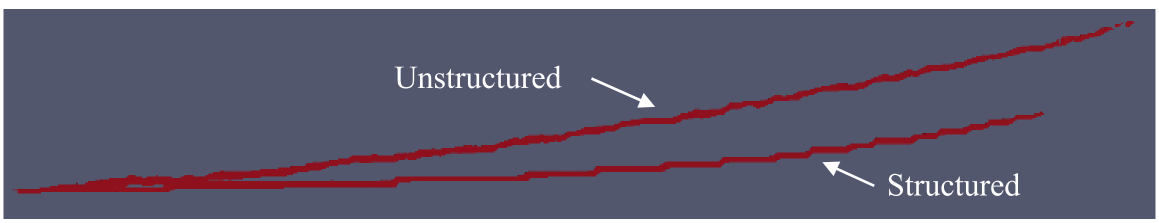

Figure 3.20. The crack path for the simulation based on the geometry of specimen CT_31 using a uniform mesh is shown in (a). The iso-volume plots of the phase-field variable between 0 and 0.01 for the structured mesh and unstructured mesh are shown in (b).

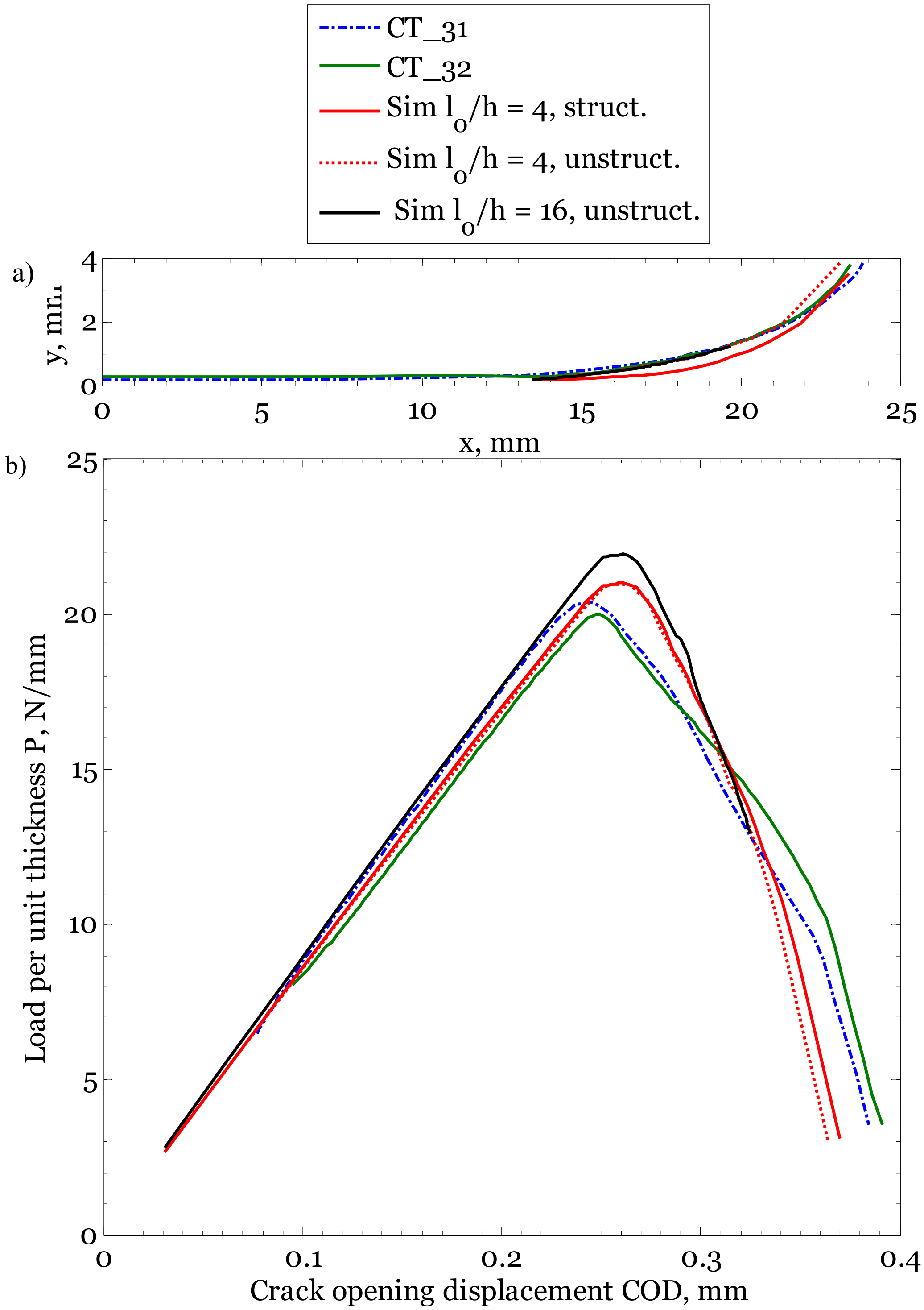

Figure 3.21. Comparison between experimental results and the simulation with the geometry based on the specimen CT_31.

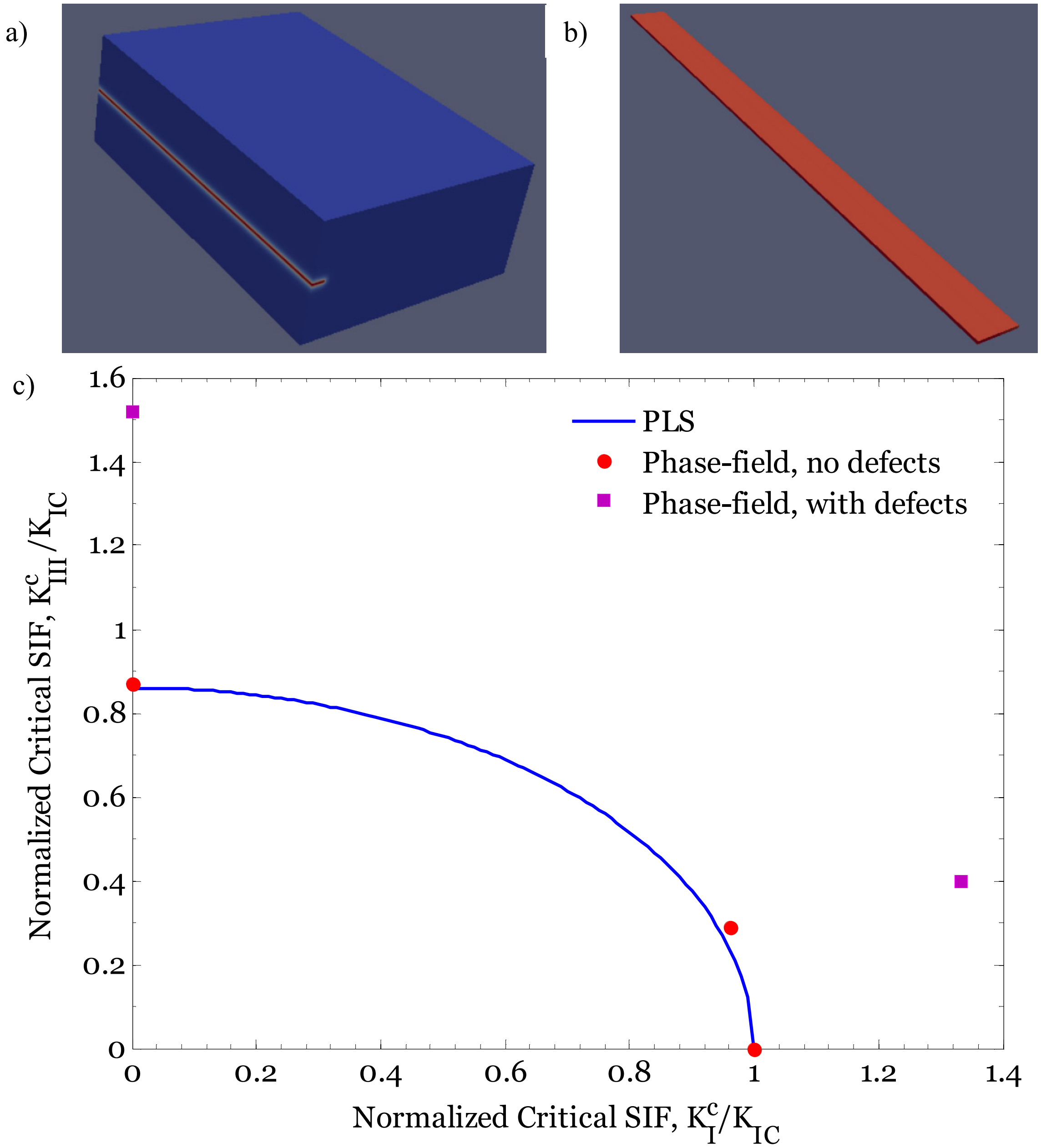

Figure 3.22. Simulation for pure mode III loading. (a) Domain of the simulation. (b) growth of the crack as an extension of the original crack plane. (c) Failure envelope K^{∞}_{Ic}/K_{IC} vs. K^{∞}_{IIIc}/K_{IC} corresponding to the principle of local symmetry (blue line) and predictions from the phase-field simulations without defects (red dots) and with defects (magenta squares).

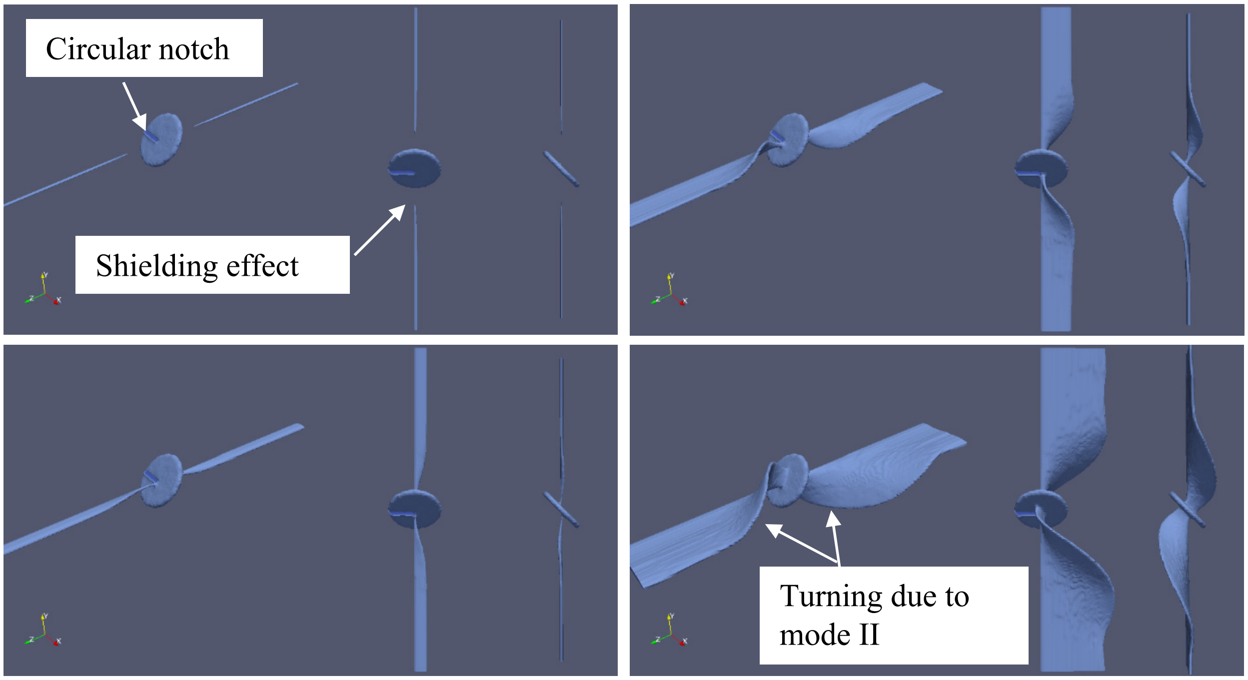

Figure 3.23. Perturbation of the parent crack front by a single daughter crack oriented at 45° relative to the parent crack plane. The images show the iso-volume plots of phase-field values below 0.2. The left portion of each image provides a 3D perspective view, while the second and third parts on the right provide two projected views of the parent crack surface in the $+\mathbf{n}$ and $-\mathbf{b}$ directions of the parent crack front.

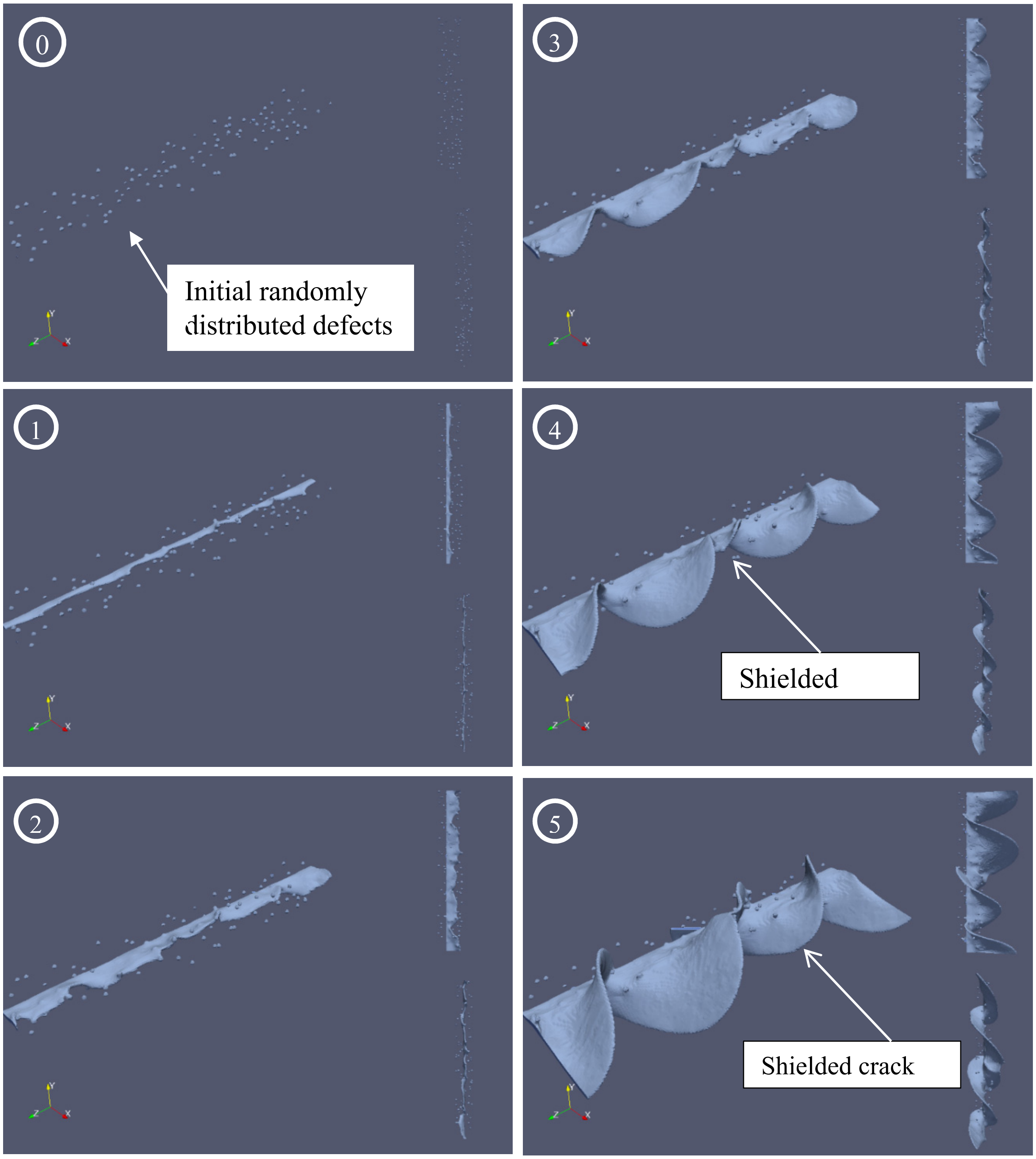

Figure 3.24. Pure mode III loading with defects. 0.06% of the nodes located inside a tube are assigned a damage value $c = 0$; the tube axis is parallel to the parent crack front line and its cross-section has the dimensions of $30l_0 \times 20l_0$ centered at the location $x = 5l_0, y = 0$.

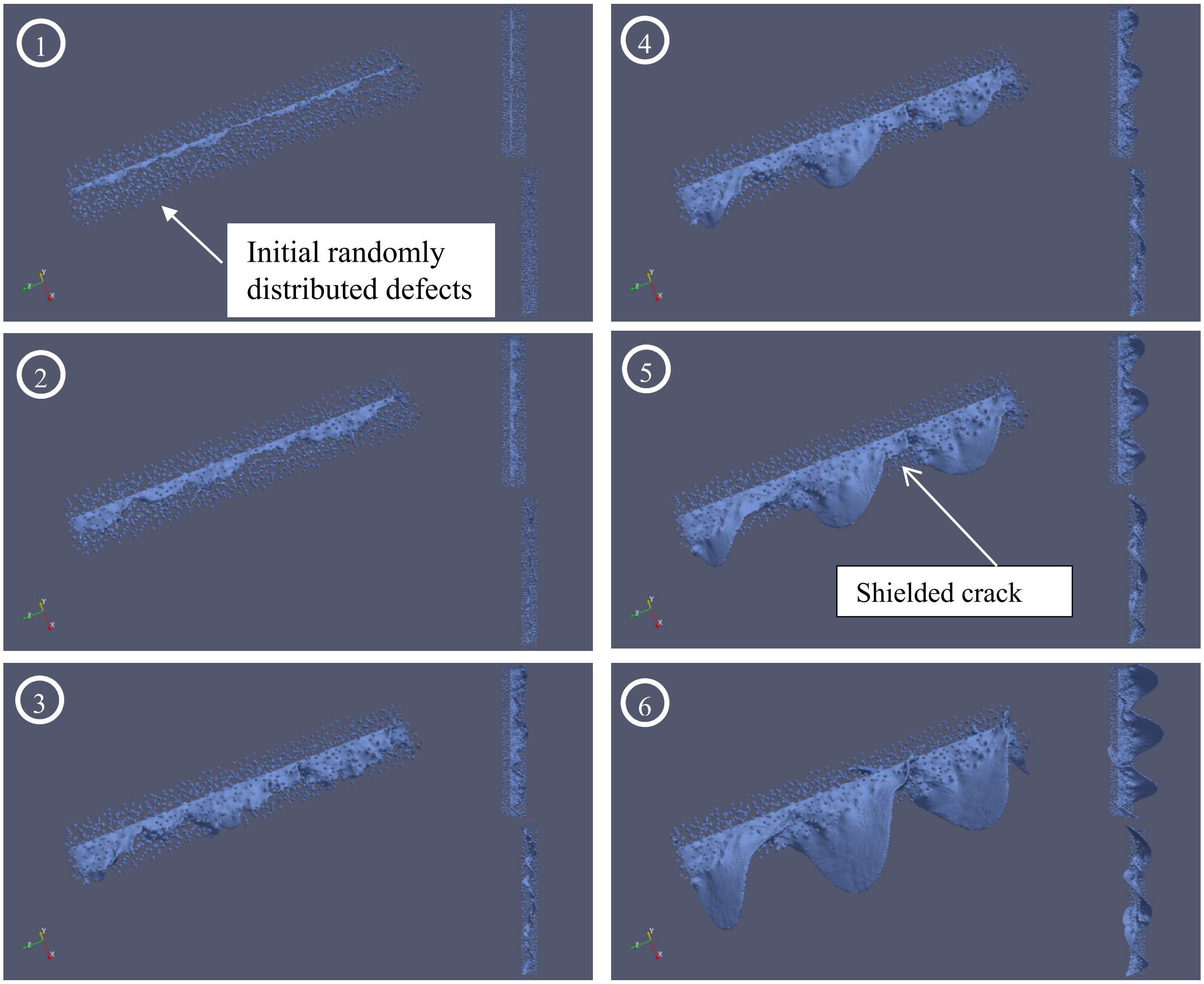

Figure 3.25. Pure mode III loading with defects. 0.6% of the nodes located inside a tube are assigned a damage value $c = 0$; the tube axis is parallel to the parent crack front line and its cross-section has the dimensions of $30l_0 \times 20l_0$ centered at the location $x = 5l_0, y = 0$.

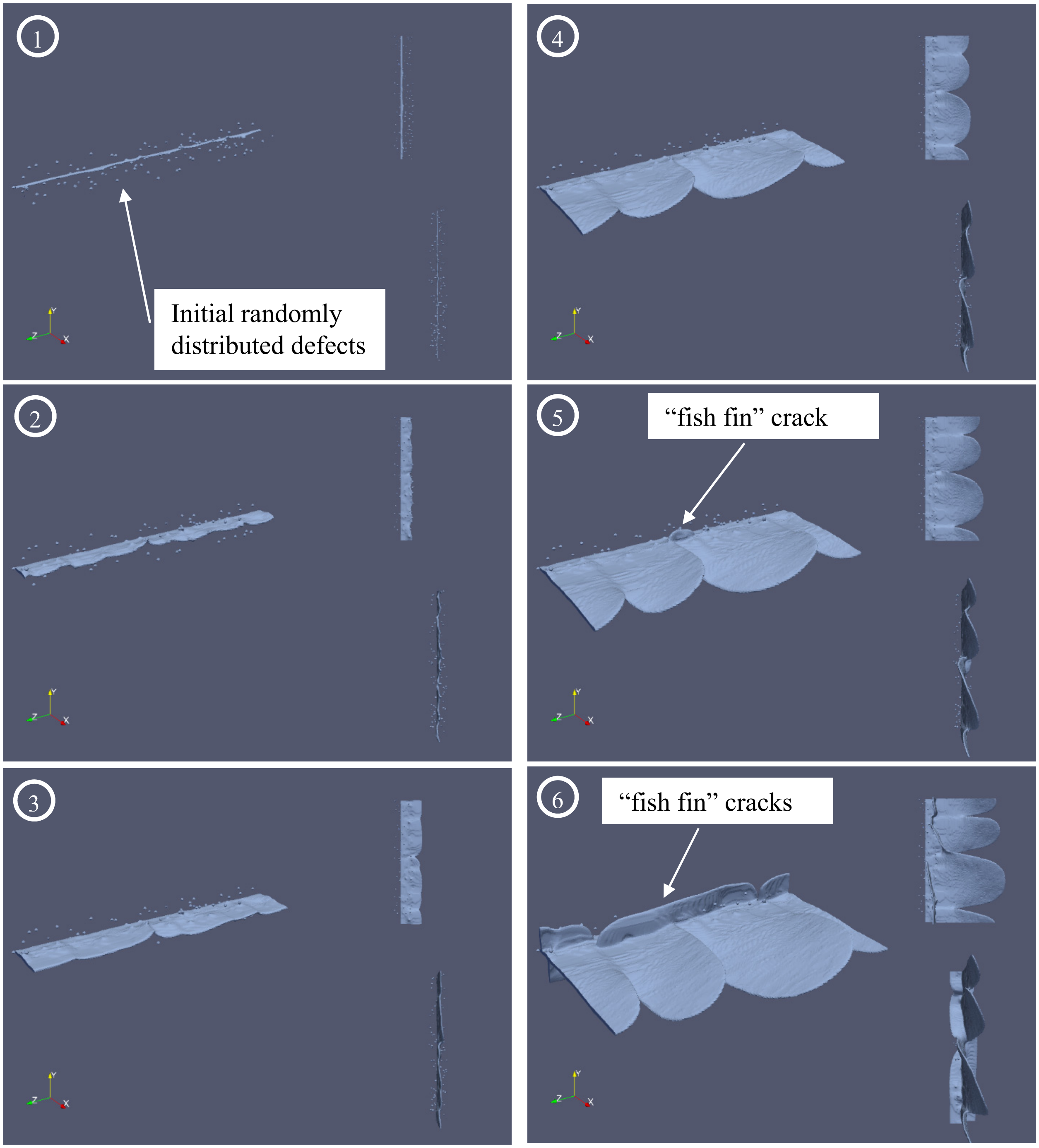

Figure 3.26. Mixed-mode I+III loading with $K_{III}^{\infty} / K_I^{\infty} = 0.5\left(K_{III}^{\infty} / K_I^{\infty}\right)_{cr}$, well below the level according to the linear instability analysis of Leblond et al. (2011).

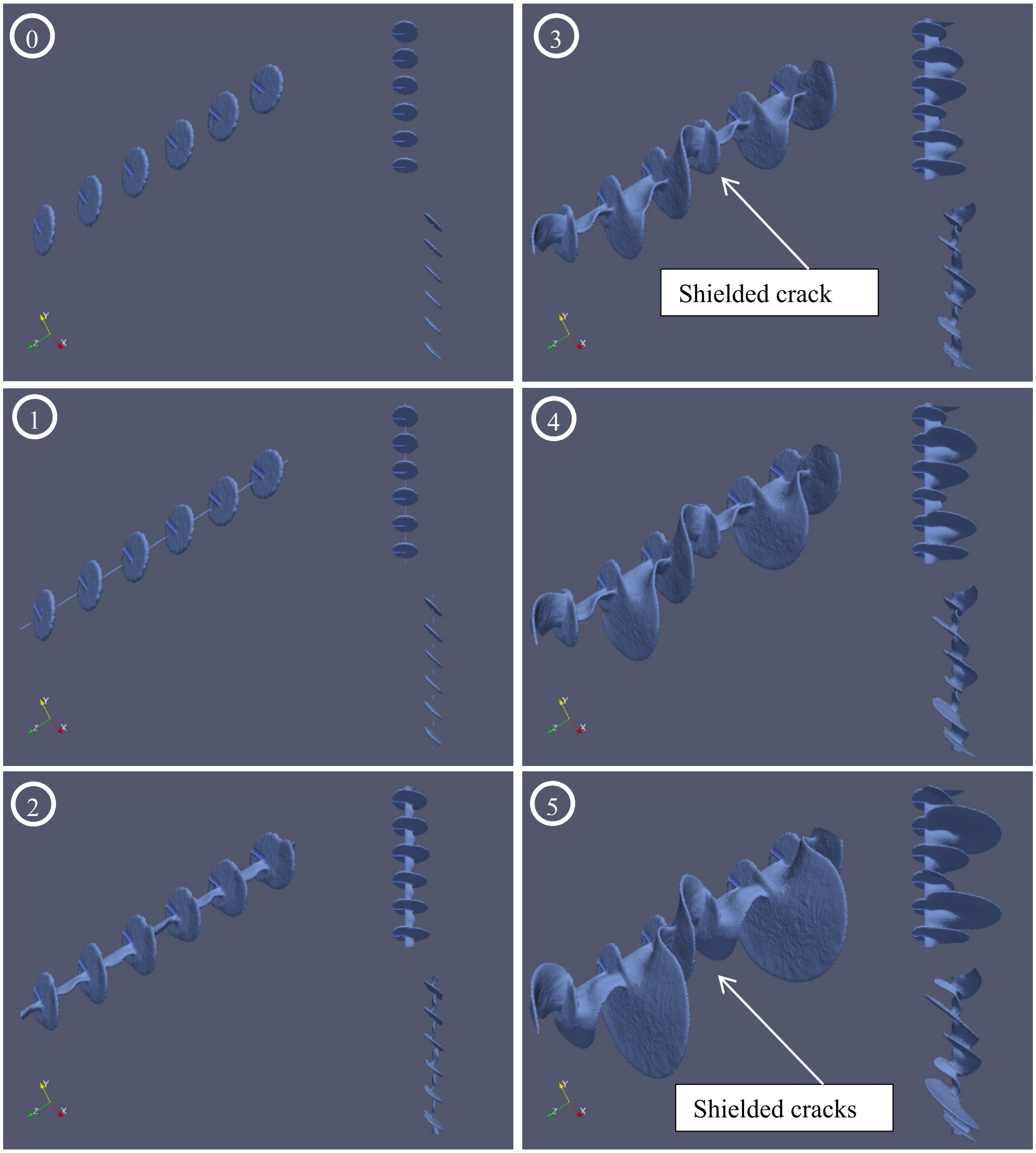

Figure 3.27. Simulation for a domain of a parent crack with six discrete daughter cracks under pure mode III loading.

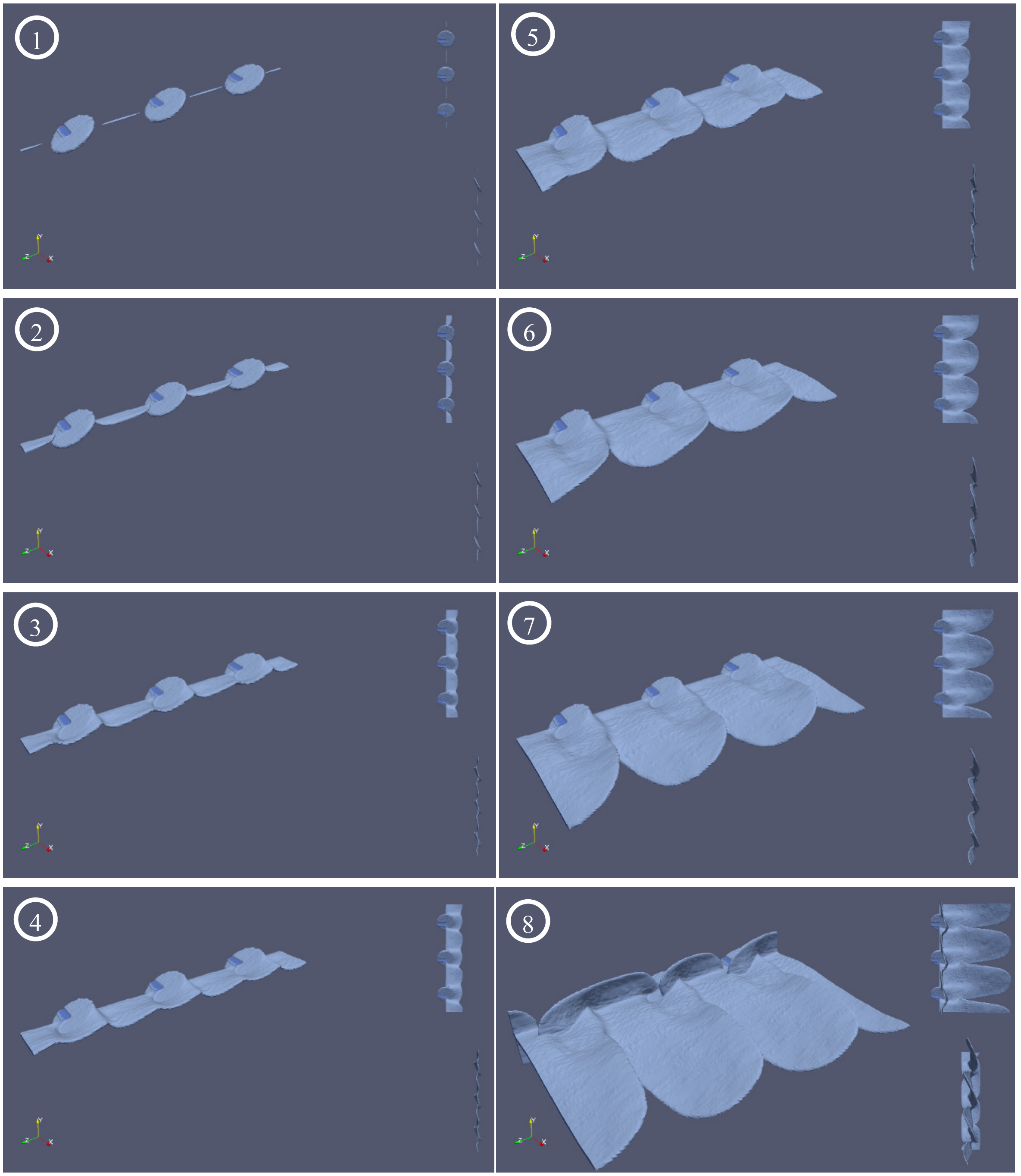

Figure 3.28. Simulation for a domain of a parent crack with three discrete nucleation of daughter cracks under subcritical mixed-mode I+III loading $K_{III}^{\infty} / K_{I}^{\infty} = 0.5\left(K_{III}^{\infty} / K_{I}^{\infty}\right)_{cr}$.

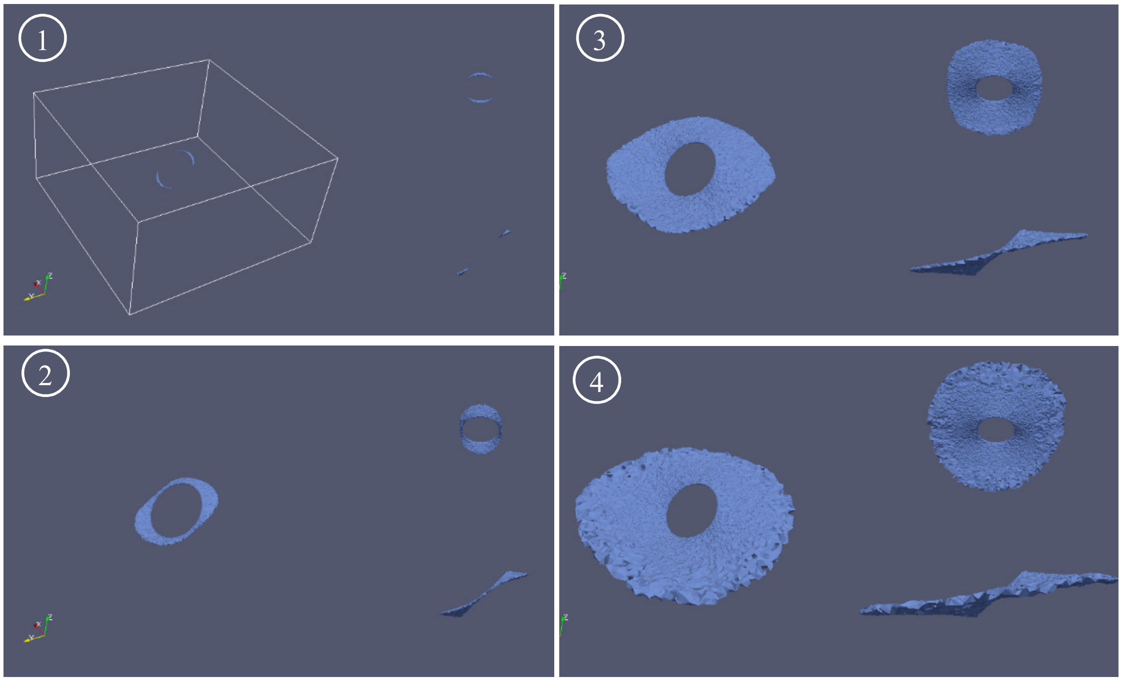

Figure 3.29. Growth of a circular center-crack under uniaxial tensile loading. Each image shows a full 3D view, a view opposite to the loading direction (top right of the image) and a view parallel to the initial crack plane (bottom right of the image). The circular hole is the location of the initial crack which was modeled by double node surfaces. The initial crack plane was inclined at an angle of 45° with respect to the uniaxial loading direction which was along the z axis.

`

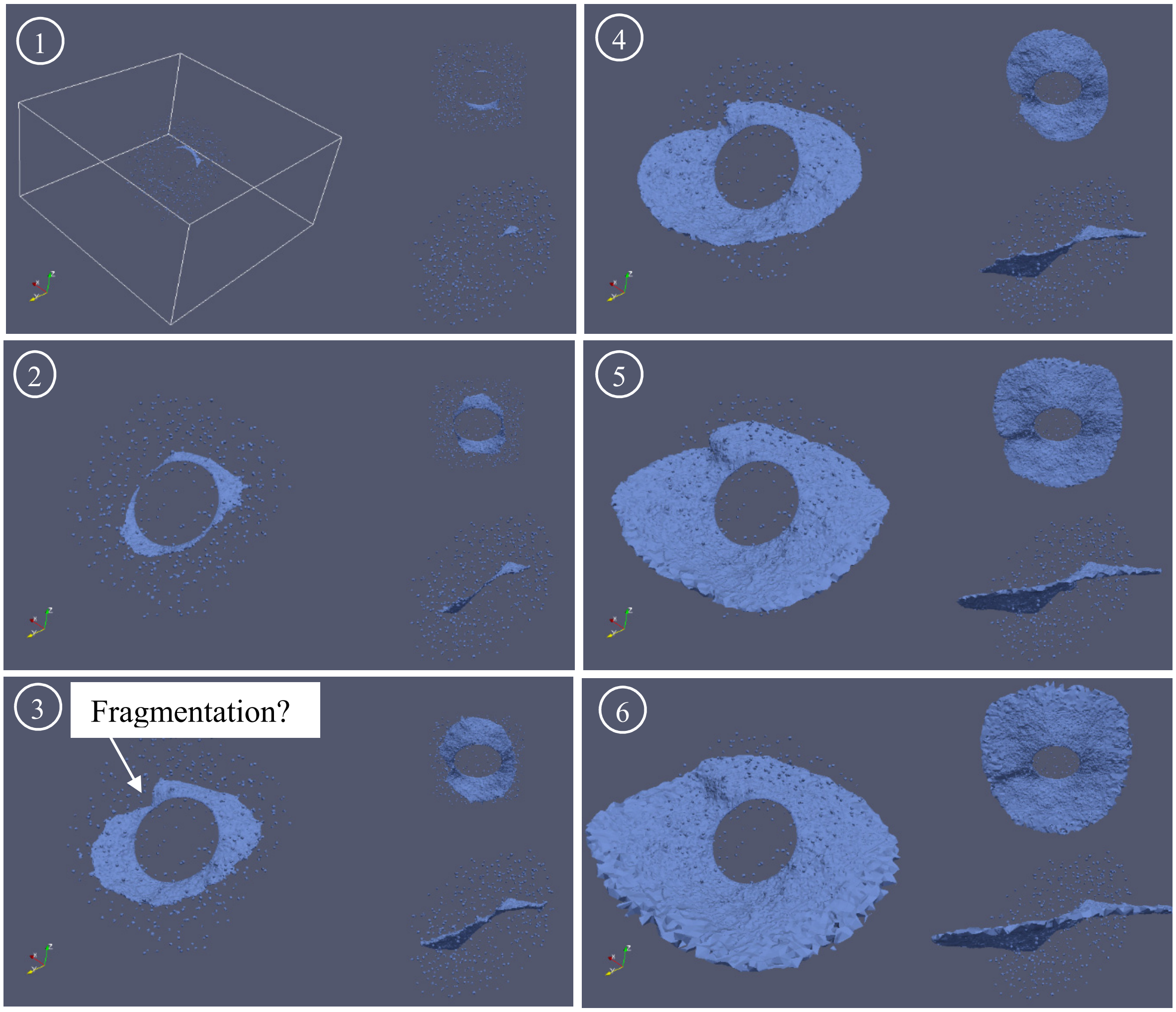

Figure 3.30. Growth of a circular center-crack under uniaxial tensile loading. Each image shows a full 3D view, a view opposite to the loading direction (top right of the image) and a view parallel to the initial crack plane (bottom right of the image). The defects were assigned randomly to 0.2% of the nodes which are inside a torus centered at the center of the initial crack with major radius equal to the radius of the crack and minor radius of $30l_0$, (nodes with normal projections onto the initial crack plane outside the initial crack front circle were not assigned any damage.)

Chapter 4: Conclusions and Future Works

In this work we have studied fundamental questions related to the initiation and continued growth of daughter cracks under far-field mixed-mode I+III loading. We showed that the formation of type A daughter cracks occurs through the homogeneous nucleation and growth of localized crack front distortions and not through the growth of unstable modes from a smooth extension of the parent crack as suggested by Pons and Karma (2010) and others. The nucleation of type B cracks was not observed in our experiments on glass, Homalite-100 or gelatin based hydrogel. We showed that a parent crack subjected to combined modes I+III loading causes fragmentation of the crack front *without any threshold*; perturbations as small as $K_{III}^{\infty}/K_{I}^{\infty} \sim 0.001$ cause nucleation of fragmented daughter cracks. The distance between the daughter cracks is dictated by the length scale corresponding to the decay of the elastic field; this decay depends on the thickness dimension of the parent crack from which the daughter fragments are nucleated. The thickness of the parent crack is governed either by the microstructural scale blunting of the natural crack, or by the local radius of curvature of grooves for a machined crack. As the type A nucleated cracks continue growing, they coarsen in spacing also through elastic shielding. Failure that occurs through break-up of the bridging regions between the type A cracks was observed in the case of the gel specimens. Based on these results, the following sequence of events is proposed that governs initiation and growth of cracks under mixed-mode I + III:

- First, type A daughter cracks are nucleated from random defects in the vicinity of the parent crack.
- Second, fluctuations and elastic interaction result in shielding of some subset of the nucleated daughter cracks; some daughter cracks are arrested.

- As the daughter cracks grow farther, the parent crack, pinned at the original position, experiences increased stress intensity factor and the bridging regions begin to crack and the parent crack front advances towards the daughter cracks.
- It is now possible to set up a new structure, where the leading edge is formed by the fragmented type A daughter cracks, while the trailing edge is created by the fracture of the bridging regions between the type A daughter cracks. In the absence of any mode II, there is no driving force to alter this picture, and the process can sustain itself and break the entire specimen creating a system of echelon cracks under the combined mode I + III loading.

Phase-field model for fracture was also explored in order to study the above mechanism of mixed-mode I + III crack growth. The phase-field model was first verified against close-form solutions for simple 2D problems. Then it was validated again the experimental results for the in-plane pure mode I and mixed-mode I+II loading problems. The results showed a very good agreement between the phase-field solution and the experimental data. Finally, the phase-field model was used to simulate the nucleation and growth of daughter cracks under mixed-mode I+III loading. The outcome of these exercises reveals that the length scale l_0 used in representing the crack surface by the phase-field plays a crucial role in determining the appropriateness of the solution, especially for the problem in which there exist interactions between cracks. It is clear that l_0 must be chosen to be extremely small in comparison to the smallest dimension in the problem. But, this brings about a significant increase in the computational cost for the problem. Within the present limitations in computational resources, we were able to reproduce qualitatively the ingredients of initiation, coarsening and steady state growth that were observed experimentally.

While the simulations presented here indicate the potential of the phase-field method to capture complex crack growth in mixed-mode I + III problems, there are many questions that still remain open in this problem which should be explored further in order to develop a suitable predictive model for mixed-mode fracture. First, increasing the computational resource to simulate a larger problem size would be fruitful in the future. Thus, for example, we can revisit the problem of the center-crack under uniaxial tensile load with a crack size much larger than the length scale l_0. This will allow us to reproduce quantitatively all the aspects of the initiation, coarsening and steady state growth which are observed experimentally. Second, the steady-state growth of the system of parent crack front segments and daughter cracks may be viewed as an "effective" crack which dissipates more energy as it grows than a simple mode I crack. The idea of a multi-scale model of a cohesive zone that embeds such a system has been examined by Leblond et al. (2015) and can be explored further to formulate a theory of "effective crack" under mixed-mode I+III loading. Third, one may extend the mixed-mode I+III conditions by examining problems with mixed-mode I+II+III loading. As was pointed out earlier, the addition of a mode II loading will either kink or turn the crack front; the combination of mode II and III may force the crack to form a torturous but continuous surface rather than a fragmented surface. The mode II loading may also be a driver for coalescence of the type A cracks. Thus, one may ask the question: is there a threshold of mode II, above which there does not exist daughter cracks which are unconnected? Or could the presence of mode II inhibit crack front fragmentation altogether?

Appendix

APPENDIX A. TABLES OF STRESS INTENSITY FACTORS FOR PART-THROUGH CRACKS FOR SPECIMEN TYPES I, II AND III.

The variation of the stress intensity factor along the crack front for the original Goldstein-Osipenko geometry and its variants used in this work, labeled Type I, III and III specimens are provided here; the stress intensity factors were calculated using a boundary element code developed by Li et al ((Li S, Mear ME 1998), (Li S, Mear ME, Xiao L 1998)).

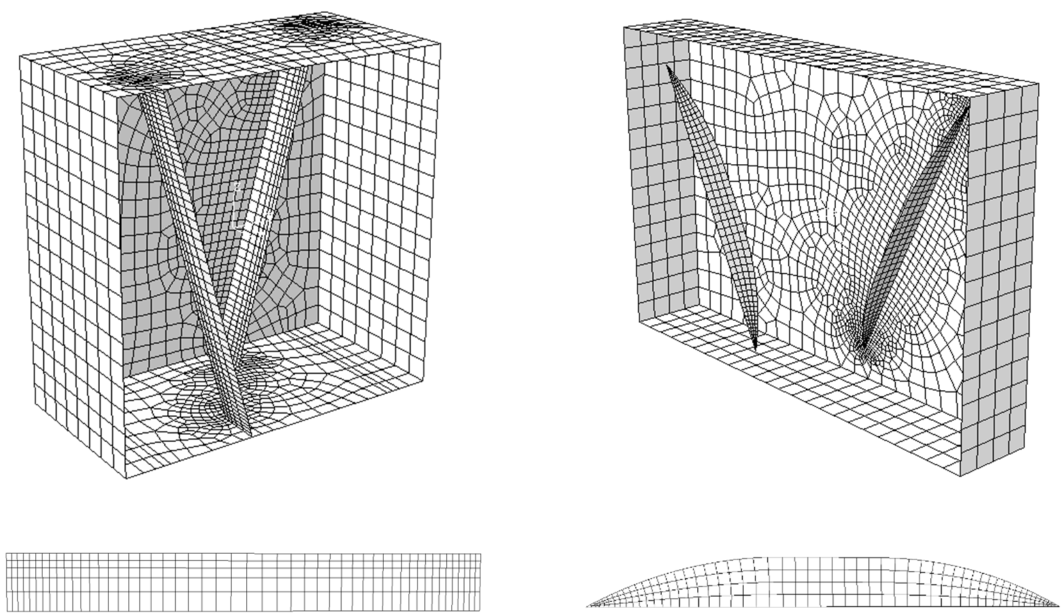

Figure A 1. (a) Mesh discretization of Goldstein-Osipenko configurations. (b) Typical mesh discretization for Part-Through Cracks configurations

Table A 1. Stress Intensity Factors for Goldstein-Opisenko configurations

s	K_I^∞	K_{II}^∞	K_{III}^∞	s	K_I^∞	K_{II}^∞	K_{III}^∞
0.000	0.031	0.100	0.052	0.533	-0.200	0.003	0.341
0.022	-0.036	0.034	0.060	0.594	-0.177	0.000	0.334
0.047	-0.076	0.021	0.069	0.650	-0.153	-0.003	0.324
0.074	-0.114	0.015	0.082	0.701	-0.124	-0.006	0.313
0.103	-0.153	0.013	0.101	0.748	-0.088	-0.009	0.299
0.136	-0.191	0.014	0.128	0.790	-0.042	-0.013	0.281
0.171	-0.226	0.015	0.163	0.829	0.017	-0.018	0.260
0.210	-0.252	0.017	0.204	0.864	0.089	-0.024	0.239
0.252	-0.267	0.017	0.247	0.897	0.172	-0.033	0.221
0.299	-0.269	0.016	0.286	0.926	0.260	-0.046	0.207
0.350	-0.260	0.013	0.317	0.953	0.347	-0.067	0.199
0.406	-0.243	0.010	0.336	0.978	0.429	-0.104	0.195
0.467	-0.223	0.006	0.344	1.000	0.492	-0.295	0.210

Table A 2. Stress Intensity Factors for Part-Through Cracks for Types I, II and III

s	Specimen Type I			Specimen Type II			Specimen Type III		
	K_I^∞	K_{II}^∞	K_{III}^∞	K_I^∞	K_{II}^∞	K_{III}^∞	K_I^∞	K_{II}^∞	K_{III}^∞
0.000	-0.003	-0.010	-0.022	0.000	0.000	0.000	0.001	-0.001	0.002
0.028	0.002	-0.054	-0.100	-0.039	-0.003	0.006	-0.029	-0.006	0.012
0.058	0.014	-0.055	-0.107	-0.058	-0.005	0.011	-0.047	-0.008	0.016
0.091	0.029	-0.048	-0.105	-0.075	-0.007	0.016	-0.065	-0.009	0.020
0.126	0.046	-0.040	-0.100	-0.091	-0.009	0.021	-0.083	-0.011	0.025
0.164	0.064	-0.031	-0.095	-0.106	-0.011	0.029	-0.101	-0.012	0.031
0.204	0.084	-0.024	-0.090	-0.120	-0.013	0.037	-0.117	-0.012	0.038
0.248	0.104	-0.017	-0.085	-0.131	-0.013	0.046	-0.132	-0.012	0.045
0.294	0.125	-0.010	-0.080	-0.139	-0.012	0.056	-0.145	-0.010	0.053
0.345	0.147	-0.004	-0.076	-0.144	-0.008	0.067	-0.155	-0.007	0.061
0.399	0.174	0.002	-0.074	-0.146	-0.002	0.077	-0.163	-0.001	0.069
0.450	0.199	0.002	-0.070	-0.144	-0.001	0.084	-0.167	0.000	0.074
0.500	0.221	0.002	-0.066	-0.136	-0.001	0.088	-0.166	0.001	0.076
0.550	0.239	0.003	-0.059	-0.125	0.000	0.089	-0.160	0.001	0.074
0.601	0.251	0.003	-0.051	-0.110	0.001	0.086	-0.150	0.002	0.069
0.655	0.261	0.007	-0.040	-0.092	0.008	0.081	-0.137	0.007	0.062
0.706	0.271	0.008	-0.030	-0.074	0.013	0.075	-0.125	0.010	0.054
0.752	0.277	0.008	-0.019	-0.057	0.016	0.069	-0.111	0.012	0.047
0.796	0.281	0.006	-0.009	-0.039	0.019	0.063	-0.096	0.013	0.040
0.836	0.280	0.003	0.001	-0.021	0.020	0.058	-0.080	0.012	0.035
0.874	0.275	0.000	0.010	-0.004	0.021	0.054	-0.063	0.012	0.030
0.909	0.265	-0.004	0.017	0.010	0.021	0.049	-0.047	0.011	0.026
0.942	0.247	-0.007	0.022	0.022	0.021	0.044	-0.031	0.010	0.022
0.972	0.211	-0.009	0.023	0.028	0.018	0.036	-0.016	0.009	0.017
1.000	0.023	-0.003	0.005	0.006	0.003	0.006	0.002	0.001	0.003

Note: Specimen dimensions are indicated in Section 2.1 of Chapter 2 (with thickness $D = 0.5$). Poisson's ratio $\nu = 0.35$ and unit load distributed over the length of 0.38 for specimen type I and 1.0 for specimen types II and III have been assumed in the simulations.

APPENDIX B. SUPPLEMENTARY MATERIAL H.

APPENDIX C. SUPPLEMENTARY MATERIAL M1-M6.

APPENDIX D. SUPPLEMENTARY MATERIAL G1.

APPENDIX E. SUPPLEMENTARY MATERIAL G2.

APPENDIX F. SUPPLEMENTARY MATERIAL V1.

APPENDIX G. SUPPLEMENTARY MATERIAL V2.

APPENDIX H. SUPPLEMENTARY MATERIAL V3.

APPENDIX I. SUPPLEMENTARY MATERIAL V4.

APPENDIX J. SUPPLEMENTARY MATERIAL V5.

References

Adams M, Sines G (1978) Crack extension from flaws in a brittle material subjected to compression, Tectonophysics, 49:97-118.

Ambati M, Gerasimov T, De Lorenzis L. (2015) A review on phase-field models of brittle fracture and a new fast hybrid formulation. Comput Mech ,55:383-405.

Amor H, Marigo JJ, Maurini C (2009) Regularized formulation of the variational brittle fracture with unilateral contact: numerical experiments. J Mech Phys Solids, 57:1209–1229.

Balay S et al. (2014) PETSc Users Manual. ANL-95/11 - Revision 3.5, Chicago: Argonne National Laboratory.

Barenblatt GI and Cherepanov GP (1961) On brittle cracks under longitudinal shear. Prikl Mech Math, 25:1110-1119.

Baumberger T, Caroli C, Martina D, and Ronsin O (2008) Magic angles and cross-hatching instability in hydrogel fracture, Physical Review Letters, **100**, 178303.

Borden MJ et al. (2012) A phase-field description of dynamic brittle fracture. Comput Methods Appl Mech Engrg, 77-95.

Bourdin B, Francfort GA, Marigo J (2008) The Variational Approach to Fracture. J Elasticity ,91:5-148.

Cooke ML, Pollard DD (1996) Fracture propagation paths under mixed mode loading within rectangular blocks of polymethylmethacrylate. J Geophys Res, 101:3387-3400.

Francfort GA, Marigo JJ (1998) Revisiting brittle fractures as an energy minimization problem. J Mech Phys Solids, 46:1319-1342.

Gao H, Rice JR (1986) Shear stress intensity factors for a planar crack with slightly curved front, J Appl Mech 53, 774.

Germanovich LN, Salganik RL, Dyskin AV, Lee KK (1994) Mechanisms of brittle fracture of rock with pre-existing cracks in compression. Pure Appl Geophys, 143:117-149.

Goldstein RV and Salganik RL (1974) Brittle fracture of solids with arbitrary cracks. Int J Fract, 10:507-523.

Goldstein RV, Osipenko NM (2012) Fracture structure near a longitudinal shear macrorupture. Mech of Solids, 47:505-516.

Griffith AA (1920) The phenomena of rupture and flow in solids, Phil Trans Roy Soc (London) A221:163-198.

Heister T, Wheeler M, Wick T (2015) A primal-dual active set method and predictor-corrector mesh adaptivity for computing fracture propagation using a phase-field approach. Comput Method Appl M ,290:466-495.

Hourlier F, McLean D and Pineau A. (1978) Fatigue crack growth behavior of Ti-5Al-2.5Sn alloy under complex stress (mode I + steady mode III). Metals Technology, 5:154-158.

Hull D (1993) Tilting cracks: the evolution of fracture surface topology in brittle solids. Int J Fract, 62, 119-138.

Hull D (1995) The effect of mixed mode I/III on crack evolution in brittle solids. Int J Fract, 70, 59-79.

Irwin GR (1957) Analysis of stresses and strains near the end of a crack traversing a plate. J Appl Mech 24:361-364.

Karma A, Kessler DA, Levine H (2001) Phase-Field Model of Mode III Dynamic Fracture. Phys Rev Lett, 87, 045501.

Karypis G, Kumar V (1999) A Fast and Highly Quality Multilevel Scheme for Partitioning Irregular Graphs. SIAM J Sci Comput, 20:359-392.

Knauss WG (1970) An observation of crack propagation in anti-plane shear. Int J Fract, 6:183-187.

Lazarus V and Leblond JP (2001), Crack front rotation and segmentation in mixed mode I + III or I + II + III. Part I: Calculation of stress intensity factors. J Mech Phys Solids, 49, 1399-1420.

Lazarus V, Buchholz F-G, Fulland M, Wiebesiek J (2008) Comparison of predictions by mode II or mode III criteria on crack front twisting in three or four point bending experiments, Int J Fract, 153:141-151.

Leblond JB (1999) Crack paths in three-dimensional elastic solids, I: two-term expansion of the stress intensity factors-application to crack path stability in hydraulic fracturing. Int J Solids Struct, 36:79-103.

Leblond JB, Karma A and Lazarus V (2011) Theoretical analysis of crack front instability in mode I+III. J Mech Phys Solids, 59:1872-1887.

Leblond JB, Lazarus V, Karma A (2015) Multiscale cohesive zone model for propagation of segmented crack fronts in mode I+III fracture. Int J Fract, 191:167-189.

Li S, Mear ME (1998) Singularity-reduced integral equations for displacement discontinuities in three-dimensional linear elastic media. Int J Fract, 93:87-114.

Li S, Mear ME, Xiao L (1998) Symmetric weak-form integral equation method for three dimensional fracture analysis. Comput Methods Appl Mech Engrg, 151:435-45.

Lin B, Mear ME, Ravi-Chandar K (2010) Criterion for initiation of cracks under mixed-mode I+III loading. Int J Fract, 165:175-188.

Miehe C, Hofacker M, Welschinger F (2010) A phase field model for rate-independent crack propagation: Robust algorithmic implementation based on operator splits. Comput Methods Appl Mech Engrg 199:2765-2778.

Mittelman B, Yosibash Z (2015) Energy release rate cannot predict crack initiation orientation in domains with a sharp V-notch under mode III loading. Eng Fact Mech, 141:230-241.

Movchan AB, Gao H, Willis JR (1998) On perturbations of plane cracks. Int. J. Solids Struct., 35:3419-3453.

Murakami Y et al. (1987) Stress Intensity Factors Handbook (volume 1). Pergamon Pr.

Pham KH, Ravi-Chandar K. (2014) Further examination of the criterion for crack initiation under mixed-mode I+III loading. Int J Fract, 189:121-138.

Pollard DD, Segall P, Delaney PT (1982) Formation and interpretation of dilatant echelon cracks. Geol Soc Am Bull, 93:1291-1303.

Pons AJ, Karma A (2010) Helical crack-front instability in mixed-mode fracture, Nature Let, 464:85-89.

Ravi-Chandar K, Knauss WG (1984) An experimental investigation into dynamic fracture – II. Microstructural aspects, Int J Fract, **26**, 65-80.

Ronsin O, Caroli C, Baumberger T (2014) Crack front echelon instability in mixed mode fracture of a strongly nonlinear elastic solid, Euro Physics Letters, 105: 34001.

Rubinstein AA (1985) Macrocrack interaction with semi-infinite microcrack array. Int J Fract, 27:113-119.

Smekal A (1953) Zum Bruchvogang bei sprodem Stoffrerhalten unter ein und mehrachsiegen Beanspringen. Osterr Ing Arch, 7:49-70.

Sommer E (1969) Formation of fracture 'lances' in glass. Eng Fract Mech, 1:539-546.

Tanaka Y, Fukao K, Miyamoto Y, and Sekimoto K, 1998, Discontinuous crack fronts of three-dimensional fractures, Europhysics Letters, 43, 664-670.

Wheeler MF, Wick T, Wollner W (2014) An Augmented-Lagrangian Method for the Phase-Field Approach for Pressurized Fractures. Comp. Meth. Appl. Mech. Engrg., 271: 69-85.

Williams ML (1952) Stress singularities resulting from various boundary conditions in angular corners of plates in extension, J App Mech, 19:526-528.

Xu G, Bower AF, Ortiz M (1994) An analysis of non-planar crack growth under mixed mode loading. Int J Solids Struct 31:2167–2193.

Yates JR, Miller KJ (1989) Mixed-mode (I-III) fatigue thresholds in a forging steel. Fatigue Fract Eng Mater and Struct, 12:259-270.

Younes AI, Engelder T. (1999). Fringe cracks: Key structures for the interpretation of the progressive Alleghanian deformation of the Appalachian plateau. GSA Bulletin, 111: 219-239.